December 2020

A Mechanistic Investigation of Cytochrome C Nitrite Reductase Catalyzed Reduction of Nitrite to Ammonia: The Search for Catalytic Intermediates

SHAHID SHAHID
University of Wisconsin-Milwaukee

Follow this and additional works at: https://dc.uwm.edu/etd

Part of the Biochemistry Commons, Chemistry Commons, and the Microbiology Commons

A MECHANISTIC INVESTIGATION OF CYTOCHROME *C* NITRITE

REDUCTASE CATALYZED REDUCTION OF NITRITE TO AMMONIA:

THE SEARCH FOR CATALYTIC INTERMEDIATES

by

Shahid Shahid

A Dissertation Submitted in

Partial Fulfilment of the

Requirement for the Degree of

Doctor of Philosophy

in Chemistry

at

The University of Wisconsin-Milwaukee

December 2020

ABSTRACT

A MECHANISTIC INVESTIGATION OF CYTOCHROME *C* NITRITE REDUCTASE CATALYZED REDUCTION OF NITRITE TO AMMONIA: THE SEARCH FOR CATALYTIC INTERMEDIATES

by

Shahid Shahid

The University of Wisconsin-Milwaukee, 2020
Under the Supervision of Professor A. Andrew Pacheco

Cytochrome *c* Nitrite Reductase (ccNiR) is a periplasmic homodimeric decaheme enzyme that catalyzes the reduction of nitrite to ammonium in a process that involves six electrons and eight protons. Under standard assay conditions, which use a strong reducing agent as an electron source, catalysis takes place rapidly without producing detectable intermediates. However, intermediates do accumulate when weaker reducing agents are employed, allowing the ccNiR mechanism to be studied. Herein, the early stages of *Shewanella oneidensis* ccNiR-catalyzed nitrite reduction were investigated in isolation by using the weak reducing agents *N*,*N*,*N'*,*N'*-tetramethyl-*p*-phenylenediamine (TMPD) and the 2-electron reduced form of indigo trisulfonate. Experiments were done with the wild type enzyme (wtccNiR) as well as with R103Q, Y206F, and H257Q variants.

A UV/Vis stopped-flow investigation of the reaction between nitrite-loaded wtccNiR and TMPD revealed for the first time that the reaction proceeds via a transient 1-electron reduced intermediate. Generation of this species is pH-independent, whereas its decay to a previously characterized 2-electron reduced intermediate is fastest at pH 6.8 and significantly slower at higher

pH. The pH dependence is ascribed to the rate-limiting cleavage of the nitrite N – O bond, which requires a prior di-protonation predicted to be slow in earlier computational studies.

Under steady-state conditions, *S. oneidensis* ccNiR catalyzed the slow 1-electron reduction of nitrite to nitric oxide, which was monitored by tracking the concomitant appearance of the colored TMPD$^+$ radical product. The rate of TMPD$^+$ formation was found to be directly proportional to the concentration of TMPD$^+$ at low TMPD concentrations, providing important insights about the mechanism of NO˙ release. The steady-state studies also showed that nitrite is a substrate inhibitor of NO˙ release when TMPD is the electron source, probably because it blocks exit by NO˙ through the nitrite entry channel.

The H257Q variant of ccNiR was found to have 1/400th of the wild type enzyme's nitrite reductase activity in the standard assay in which methyl viologen monocation radical is the electron source, but nearly normal hydroxylamine reductase activity. This demonstrated that H257 is essential for nitrite reduction but not for reduction of hydroxylamine, a putative intermediate in the catalytic process. UV/Vis spectropotentiometry showed that the nitrite-loaded active site of H257Q still reduced at fairly high applied potential, but the reduction was by one electron, whereas the wild type is reduced in a concerted 2-electron step. The experiments with the variant, coupled with the pH-dependent stopped flow experiments with wtccNiR, confirm H257's importance in facilitating nitrite reduction, but suggest that its role is to modulate the pK_a values of one or more of the waters that form a complex hydrogen bonding network in the active site. This view is more conservative than earlier theoretical predictions of direct histidine involvement in nitrite diprotonation leading to N – O bond cleavage.

TABLE OF CONTENTS

Contents

v

Appendices

Appendix 1: Supporting Material For Chapter 2

Appendix 2: Supporting Material For Chapter 3

LIST OF FIGURES

LIST OF TABLES

LIST OF SCHEMES

LIST OF ABBREVIATIONS

FULL NAME

NAD(P)H	Nicotinamide Adenine Dinucleotide Phosphate
CsNiR	Siroheme-Containing Nitrite Reductases
NO	Nitric Oxide
N₂O	Nitrous Oxide
DNRA	Dissimilatory Nitrite Reduction to Ammonium
NaR	Mo Containing Nitrate Reductase
CcNiR	Cytochrome *c* Nitrite Reductase
AMO	Ammonium Monooxygenase
HAO	Hydroxylamine Oxidase
Nif	Nitrogen-Fixing Enzyme Nitrogenase
rRNA	Ribosomal Ribonucleic Acid
MR-1	Manganese-, Or Metal-Reducing
rpm	Revolutions Per Minute
CDS	Coding Sequence
CXXCH	Cysteine-XX(Any Two Amino Acids)-Cysteine-Histidine
CDC	The Centers for Disease Control and Prevention
G, C	Guanine, Cytosine Neucleotide
DNA	Deoxyribonucleic Acid
GFP	Green Fluorescence Protein
LM Medium	Lactate Medium
CCM	Cytochrome *C* Maturation Protein
Ccma-H	Cytochrome C Maturation Chaperones (A-H)
Nb	Neuroglobin
Cytp450	Cytochromes P450 Protein
NOS	Nitric Oxide Synthase
Cd1NiR	*Cd1* Type Heme Cytochrome C Nitrite Reductase
PDB	Protein Data Bank
ICP	Inductively Coupled Plasma
TvNiR	Cytochrome *c* Nitrite Reductase from *Thialkalivibrio*

Cyma	Cytoplasmic Membrane Protein A
NrfB	Small Pentaheme Electron-Transfer Protein
DMSO	Dimethyl Sulfoxide
MtrA	Metal-Reducing Protein A
PCET	Protons in Proton-Coupled Electron Transfers
Mv_{red}	Methyl Viologen Monocation Radical
DFT	Density-Functional Theory
$HisH^+$	Protonated Histidine Amino Acid
H_Y	Tyr-206
H_R	Arg-103
H_H	His-257
EDTA	Ethylenediaminetetraacetic Acid
CPET	Concerted Proton-Electron Transfer
PFV	Protein Film Voltammetry
SHE	Standard Hydrogen Electrode
UV/Vis	Ultraviolet–Visible Spectroscopy
EPR	Electron Paramagnetic Resonance
TMPD	*N*,*N*,*N′*,*N′*-Tetramethyl-*P*-Phenylenediamine
Kan	Kanamycin
Rif	Rifampicin
LB	Lysogeny Broth or Luria Broth, or Lennox Broth
AS	Ammonium Sulfate
HIC	Hydrophobic Interaction Chromatography
HEPES	(4-(2-Hydroxyethyl)-1-Piperazineethanesulfonic Acid)
EDTA	Ethylenediaminetetraacetic Acid
TFF	Tangential Flow Filtration
PDA	Photodiode Array
Bis-tris	2-[Bis-(2-hydroxy-ethyl)-amino]-2-hydroxymethyl-propane-1,3-diol
HEPPS	3-[4-(2-Hydroxyethyl)piperazin-1-yl]propane-1-sulfonic acid
SVD	Singular Value Decomposition
PCR	Polymerase chain reaction
EtBr	Ethidium Bromide
PMSF	Phenylmethylsulfonyl Fluoride
AEBSF	4-(2-Aminoethyl)Benzenesulfonyl Fluoride Hydrochloride
H257Q	Histidine Replaced by Glutamine at 257 Position of ccNiR Gene

HisTrap	High-Performance Columns for His-Tag Protein Purification
A280	Absorbance at 280 nm Wavelength
TEV	Tobacco Etch Virus
O.D	Optical Density
DTT	Dithiothreitol
SEC	Size Exclusion Chromatography
SDS-PAGE	Sodium Dodecyl Sulphate–Polyacrylamide Gel Electrophoresis
OTTLE	Optically Transparent Thin-Layer Electrode
LMCT	Ligand-to-Metal Charge Transfer
$MV^{+\cdot}$ or MV_{red}	Methyl Viologen Monocation
EDTA	Ethylenediaminetetraacetic Acid
ppm	Parts Per Million
MM	Michaelis-Menten
ΔG	Gibbs Free Energy Change
I3S	Indigo trisulfonate
OTTLE	Optically Transparent Thin-Layer Electrode
CPE	Controlled Potential Electrolysis

ACKNOWLEDGMENTS

In addition, I would like to acknowledge my parents as they have provided me with unconditional support and love through this journey. They have always given me their trust and confidence. Last but not least, I would like to show my deep appreciation towards my wife, my lovely Bou, Samiha for keeping me motivated and optimistic during my stressful time. She sacrificed her career to take good care of me. It would mentally nearly impossible without her constant support.

Chapter 1

Introduction

1.1. The importance of nitrite in the nitrogen cycle

Nitrite, which undergoes reduction to ammonium or oxidation to nitrate by various biological enzymes, is one of the pivotal components in the biological nitrogen cycle (Fig. 1.1). The reductive fate of nitrite is governed by either an assimilatory or a dissimilatory process. In the assimilatory process, nitrite is reduced to ammonium for incorporation into biomass. Assimilatory nitrite reduction is found in bacteria, plants, and fungi, and the process is catalyzed by either NAD(P)H- or ferredoxin-dependent cytoplasmic siroheme-containing nitrite reductases (CsNiR).[1-4] While the goal of assimilatory nitrite reduction is the production of ammonium for incorporation into biomass, dissimilatory nitrite reduction is an anaerobic respiratory process that is carried out by bacteria. In dissimilatory nitrite reduction, the product can be dinitrogen (respiratory denitrification) or ammonium (respiratory nitrite ammonification).[1-4] Interestingly, both products are never produced at the same time during anaerobic respiration.[5] Biological nitrite reduction is of interest to microbiologists and ecologists because of its importance in energy conservation and balancing eutrophication in the environment, among other things.[6]

Metalloenzymes play essential roles in both assimilatory and dissimilatory processes, which attracts the interest of bioinorganic chemists. The first step in respiratory denitrification is the reduction of nitrite to nitric oxide (NO$^.$), and this is carried out either by an enzyme called cytochrome cd_1 nitrite reductase, or alternatively by a copper-containing nitrite reductase. An enzyme called NO reductase then reduces NO$^.$ to nitrous oxide (N$_2$O), which is in turn reduced by

N$_2$O reductase to dinitrogen (N$_2$). Like the nitrite reductases, both NO reductase and N$_2$O reductase are metalloenzymes. The complete denitrification process converts so-called "reactive nitrogen"
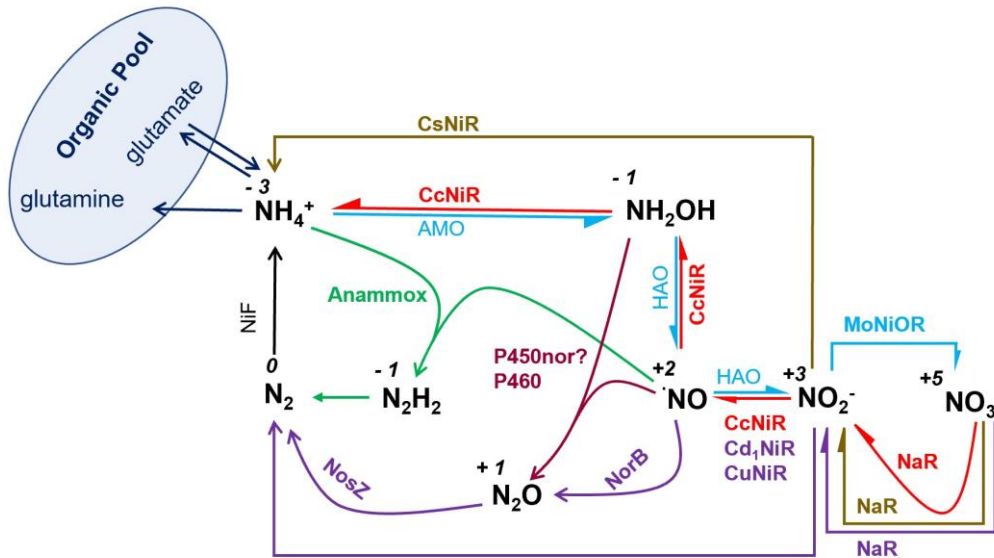
Figure 1.1. The nitrogen cycle, showing the five major and one minor enzyme-catalyzed pathway. **Black**: Nitrogen fixation (Mo or Fe metal containing nitrogenase), **Red**: Dissimilatory nitrite reduction to ammonium (DNRA) (NaR: Mo containing nitrate reductase, ccNiR: *c*-heme containing cytochrome nitrite reductase), **Dark Brown:** Assimilatory Ammonification (NaR: Mo containing nitrate reductase, CsNiR: siroheme containing nitrite reductase), **Violet**: Denitrification, **Green**: Anaerobic ammonium oxidation (Anammox), **Light Blue:** Nitrification (AMO; ammonium monooxygenase, HAO: hydroxylamine oxidase)

(nitrogen that is universally bioavailable) into dinitrogen, which is the largest terrestrial nitrogen source, but is only directly usable by a handful of prokaryotes. These prokaryotes use the nitrogen-fixing enzyme nitrogenase (NiF), another metalloenzyme, to reduce dinitrogen to the reactive nitrogen species ammonium. This makes nitrogen bioavailable for non-nitrogen fixing organisms, which are the majority.

Free nitrate is much less toxic to life forms than free ammonium, and so is the primary reservoir of reactive nitrogen in the biosphere, even though it is ammonium that is directly incorporated into the biomass. Nitrate reductases, which are molybdenum-containing metalloenzymes, convert nitrate to nitrite,[7-9] which can then be converted to ammonium for biomass production either by the specialized assimilatory nitrite reduction pathway or by respiratory ammonification (also known as "dissimilatory nitrite reduction pathway to ammonium, DNRA").[10] Though the primary function of the latter process is anaerobic respiration, the ammonium generated by the process is also available for biomass incorporation. Cytochrome *c* nitrite reductase (ccNiR, also called NrfA after the *nrfA* gene that codes for it) is the main enzyme in the nitrite ammonification pathway, and remarkably, under standard assay conditions, it converts nitrite to ammonium without releasing any potential toxic intermediates. Moreover, not only nitrite can act as a terminal electron acceptor in this process, but also other nitrogenous molecules such as NO· and hydroxylamine can be reduced by ccNiR at a very good rate. In recent years, a few interesting results regarding ccNiR have been reported from different groups.[6, 11-12]

This thesis focuses on efforts to elucidate the ccNiR mechanism for nitrite reduction to ammonium. The role of conserved active site amino acids in the reduction process will be explored, and possible reactive intermediates will be identified. The ccNiR source used for the studies presented herein was the bacterium *Shewanella oneidensis*, so the section that follows explains why *S. oneidensis* was chosen, and also briefly summarizes this bacterium's interesting ecological position. Section 1.3 is an introduction to heme proteins and cytochromes in general, while Section 1.4 presents an overview of the ccNiR structure in particular. Section 1.5 provides a summary of nitrite ammonification bioenergetics and its position relative to other bacterial respiratory pathways. Section 1.6 presents a detailed summary of the ccNiR reaction mechanism as it was

3

understood prior to the research described in this thesis, while Section 1.7 concludes the introduction with an outline of the specific thesis goals.

1.2. An overview of the model species *Shewanella oneidensis* MR-1

The *Shewanella* proteobacteria (Fig. 1.2) have attracted the most attention because of their bioremediation and versatile respiration capabilities,[13] though they have also been considered as possible opportunistic pathogens of humans and other aquatic animals.[14-15] *Shewanella* species were first noticed in putrid butter in combination with other bacteria.[16] *Shewanella* can swim by using single polar type flagella so unsurprisingly they are also found in marine sediments and soil as well. Structurally, they are rod-shaped, with lengths and widths of no more than 2-3 μm and 0.4-0.7 μm, respectively.[14] *Shewanella* were first classified as belonging to the *Achromobacter* genus,[17] but after 5S RNA sequencing in 1985, the new genus name *Shewanella* was coined to honor the renowned marine microbiologist Dr. James M. Shewan.[18]

The discovery story of the *oneidensis* species is interesting (Table 1.1). It started with the surprising observation by a group of scientists that Lake Oneida contained an excessive amount of reduced manganese (Mn^{2+}) in comparison with oxidized manganese (Mn^{4+} as MnO_2), which would have been expected in natural aerated waters. The scientists could not find the reason for naturally reduced Mn^{2+} until DNA hybridization and 16S rRNA sequencing studies confirmed the presence of a new metal-reducing species of *Shewanella* bacteria. They named the new species *Shewanella oneidensis* after the name of lake Oneida. The suffix MR-1 ("manganese-, or metal-reducing") was added to reflect *S. oneidensis*' Mn reducing property; however, this moniker doesn't reflect the species' versatility in anaerobic respiration. Indeed, *S. oneidensis* can reduce a wide range of inorganic, organic, soluble, and non-soluble compounds, using them as terminal electron acceptors

during anaerobic respiration. For example, in addition to manganese dioxide, the bacteria can reduce iron, dimethyl sulfoxide, dioxygen, and even uranium. [17, 19-21]
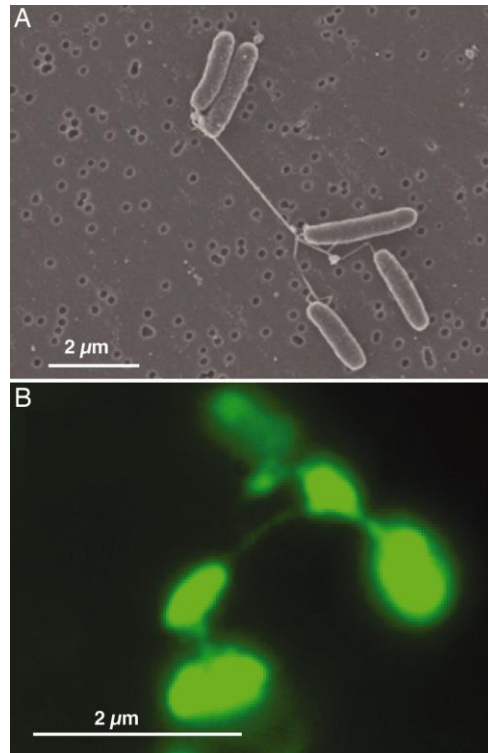
FIgure 1.2. *Shewanella oneidensis* MR-1 is seen through a scanning electron microscope (SEM) in the presence of limited oxygen and low agitation chemostat (50 rpm). (b) Fluorescence microscopy has observed similar structures when stained with a nonspecific fluorescent protein-binding stain. Both images are copied from Gorby et al (2006).[22]

The insolubility of the Mn^{4+} oxidation state also highlights a remarkable feature of *S. oneidensis* respiration: these bacteria can transfer electrons to *extracellular* electron acceptors during respiration, a process that is now termed "extracellular respiration".[17, 23-24]

The MR-1 species was the first sequenced *Shewanella* genome. It contains a 4,969,803 base pair circular chromosome, 4,758 coding genes (CDS), and a plasmid with 161,613 base pairs

and 173 CDS.[13] MSHA and tapABCD are the type IV pilin gene clusters that play a role in colony formation and mediate DNA transfer during pathogenesis.[25-27] The *S. oneidensis* genome contains 39 cytochrome *c* genes, with 14 of these encoding at least 4 hemes in multi-heme proteins. This makes *S. oneidensis* the bacterium that contains the second-greatest number of cytochrome *c* proteins identified to date; for comparison, *Escherichia coli* encodes only 5-7 *c* type cytochromes. The recently sequenced bacterium *Geobacter sulfurreducens* holds the current record for most *c*-type proteins. These bacteria have at least 111 cytochrome *c* encoding genes based on counting *c* attachment motifs, CXXCH. Out of these, 73 genes encode at least two heme groups per protein.[28-29] Unsurprisingly, the multiheme cytochrome groups in *S. oneidensis* and *G. sulfurreducens* make these organisms capable of using an extensive range of substrates for respiration.[13, 29-30]

Table 1.1. Major events in *Shewanella's* history from first identification (1931) to genome sequencing (2002)

Timeline	Events	Ref
1931	*Shewanella* first isolated and reported as *Achromobacter* type bacteria	[16]
1941	Proposed genus re-classification to *Pseudomonas* by Long and Hammer	[31]
1964 - 1967	CDC lists oxidase-positive l-b strains isolated from clinical "*Pseudomonas (Shewanella) putrefaciens*"	[32]
1972	Low G%, C% nucleotide (43–55%) in *P. putrefaciens* compare to *Pseudomonas spp.* (58–70%) suggested a new genus	[33-35]
1978	(1) *P. putrefaciens* referred to infections of bloodborne, soft-tissue iseases (2) A minimum of four distinct DNA groups	[36-37]
1985	Phylogenic studies proposed a new family Vibrionaceae and genus *Shewanella* by MacDonell and Colwell	[38]
1988	Metal reducing *Shewanella*; the idea of bioremediation	[21]
1996	*Shewanella algae* associated with human illness	[39]
2002	*Shewanella* MR-1 genome sequenced	[13]

1.2.1. Biofilm formation and transfer of electrons to external acceptors

Insoluble oxidized manganese is widely reduced by *S. oneidensis*, revealing a novel form of anaerobic respiration. Microbes form biofilms after attaching to a solid surface, and this is also the first step of external metal reduction since biofilm formation brings bacteria and oxidized metal surfaces together. In the environment, *Shewanella* first creates a metabolic interaction on the mineral surface to continue its metabolism and biofilm formation. In vitro, the *Shewanella* initially attaches to a surface (Fig. 1.3) and grows out sideways along the surface for about 24 hours to fully colonize the surface. After that, the biofilm continues to grow straight up.

A global transposon mutagenesis screening of 1500 mutants turned up 173 that had defects in either (1) attachment or (2) biofilm formation or (3) both. The study also reported that 71 of those mutants had a non-swimming phenotype, which prompted the authors to further investigate the roles of motility for biofilm formation. The mutation of the motility genes (*flhB, fliK, and pomA*) in *Shewanella* posed no problem for attachment to the glass surface, but nevertheless significantly affected biofilm development.

Other studies showed that biofilm development is also inversely nutrient-dependent, so that biofilms form faster when the nutrient level is low. When the nutrient level is high and oxygen is available, *Shewanella* can metabolize aerobically and not waste energy for biofilm formation. On the other hand, under anaerobic conditions and when the nutrient level is poor, *Shewanella* form biofilms which help them continue to thrive by interacting with oxidized metal. After successful surface colonization multicomponent electron transport systems, mainly cytochrome reductase proteins, quinones, or riboflavin, help the bacteria to transfer the electrons to terminal electron acceptors, including metal oxides, for anaerobic respiration.[40]
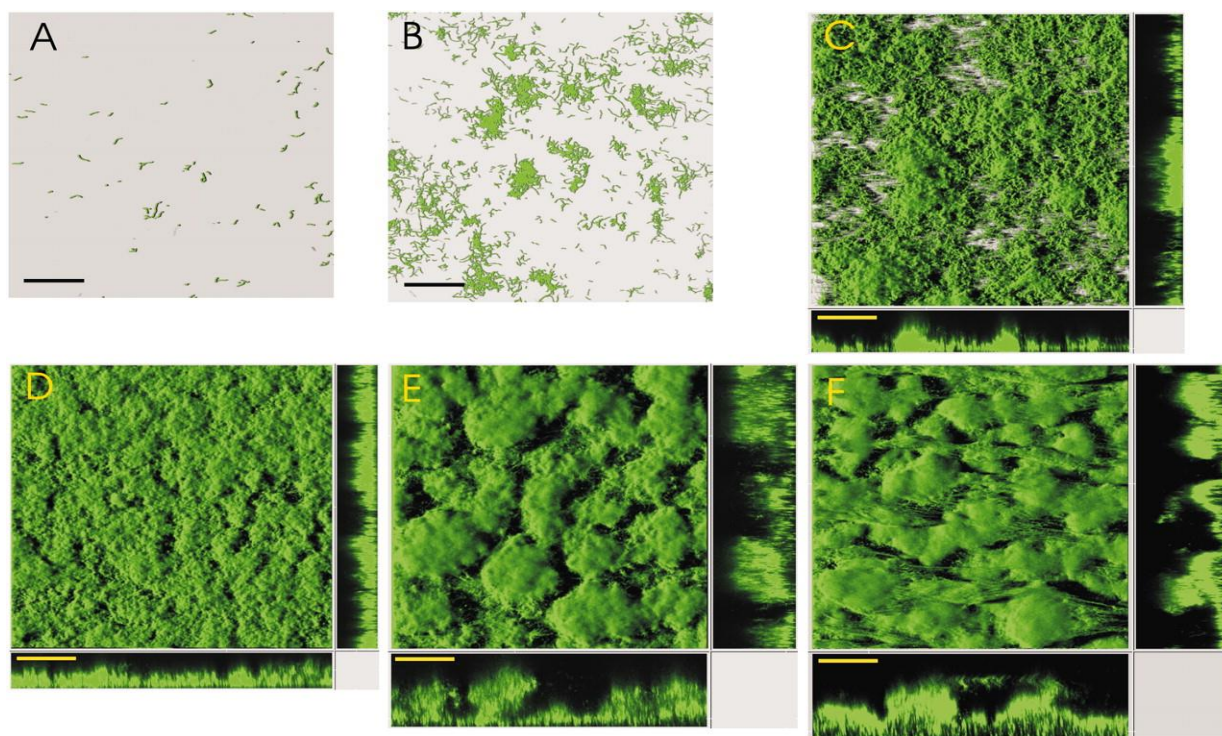
Figure 1.3. *S. oneidensis* MR-1 biofilm formation on a glass surface. Confocal laser-scanning microscopy aided green fluorescence protein (GFP)-labeled *Shewanella* cells. **(A)** adhesion by the first colonies (1 hour), **(B)** successive rapid cell divisions (8 hours), **(C)** formation of 3D structures (12-16 hours), **(D)** the cells fully cover the surface and tower to a height of around 20 μm (20-24 hours). By the 5th day, the biofilm formation enters a stable state and shown approximately 200 μm. **(E)** and **(F)** are recorded after 48 hours and 120 hours, respectively. The scale bar in the image reflects 80 μm. The bacterial cells were grown in a 0.5 mM lactate-containing LM medium. This image is copied from Thormann et al.[40]

1.2.2. *Shewanella oneidensis* is a better host for expression of ccNiR than *E. coli*

Though *S. oneidenis* has attracted the most attention from researchers for its ability to reduce solid metal oxides, the bacterium is also very well suited to be a source of ccNiR. Several methods have been suggested for the overexpression of *c*-type multi-heme cytochromes.[41-44] Originally *E. coli* seemed to be a suitable organism to use for overexpressing *c*-heme proteins such as ccNiR, and this organism has indeed been used successfully, although mostly for proteins

containing four or less hemes.[43, 45] A big downside of the *E. coli* expression system though is that eight **c**ytochrome **_c_** **m**aturation (CCM) chaperones (ccmA-H) that are required for the post-translational incorporation of *c*-type hemes into apoproteins are only expressed anaerobically in this organism. Londer et al. resolved the issue by producing an *E. coli* strain that contained the necessary chaperones within a pEC86 vector. However, ccNiR requires three additional chaperones (nrfEFG) to properly ligate lysine to the active-site heme (see below), and once again, these are expressed only anaerobically in *E. coli*.[43, 45-46]

Crucially, unlike *E. coli*, *S. oneidensis* expresses the ccmA-H and nrfEFG genes under both aerobic and anaerobic conditions. This makes *S. oneidensis* a much better host for expressing *c*-type cytochromes at high levels because, like other bacteria, *Shewanella* bacteria tend to grow much faster and to higher densities under aerobic conditions.[41, 44, 47]

1.3. Introduction to heme proteins

1.3.1. Heme

Heme is one of the most important prosthetic groups in living cells, involved in electron transfer, energy metabolism, catalysis, and transport of small molecules.[48-49] The basic heme unit consists of an iron coordinated equatorially by four nitrogen donor atoms from a macrocyclic porphyrin ligand. Hemes are widely found within proteins with one or two ligands bound to the iron axial sites, in addition to the equatorial heme ligand.

Very often the types of axial arrangements define the protein or enzyme function. For example, hemes involved purely in electron transfer are typically 6-coordinate, with two amino acid axial ligands from the protein occupying the axial sites.[50-51] Histidine and methionine are the two most common amino acid residues bound to the axial sites of hemes in electron transfer

proteins, which are sometimes referred to as closed hemes because both proximal and distal axial sites are occupied.

In contrast to closed hemes, penta-coordinated heme is termed an open heme center because of the open distal site that allows exogenous substrates to bind. Typically, when a protein's primary role is to transport small molecules such as oxygen, then a penta-coordinated open structure is most prevalent. Histidine is bound in the proximal site in most, but not all, of the cases. Interestingly, a seemingly closed heme can be functionally open because the proximal axial ligand is loosely held, and easily displaced by a substrate. A common example is water, a weak-field ligand that is easily displaced by stronger-field ligands that can bind and then undergo oxidoreductase reactions.[51] Other examples of weak distal ligand coordination are provided by Cd1NiR, bacterial cytochrome *c* peroxidase, Neuroglobin (Nb), or Cytoglobin.[52-54] In these cases, the distal ligand is often an amino acid from the protein backbone.

Importantly, the nature of proximal site ligand often dictates heme reactivity. As examples, CytP450,[55] and NOS[56] contain cysteine amino acids, peroxidases have histidine,[57] and catalase contains tyrosine.[58] CcNiR, the subject of this thesis, has a lysine ligand in the proximal site which is very unusual.[59-60] Looking specifically at nitrite reduction, the nitrite ammonifying ccNiR has the lysine as the distal ligand, whereas the NO-producing *cd1* type heme (Cd1NiR) has histidine in the distal site.[61]

1.3.2. Overview of cytochromes

Cytochromes are heme-containing proteins that are involved in electron transport and enzymatic oxidation-reduction processes. They are widely distributed in the biosphere, and along with iron-sulfur clusters, are the main electron transporting molecules used during respiration.

Because of the broad tunability of the prosthetic iron's redox potential, and the accessibility to multiple oxidation states (oxidized Fe^{3+}, reduced Fe^{2+}, and in some cases Fe^{4+} in catalytic intermediates),[62] cytochromes are highly versatile.

Irish scientist Charles Alexander MacMunn first described cytochromes as respiratory pigments in the blood in 1886,[63] but it was entomologist David Keilin that coined the term "cytochrome" (standing for "cellular pigment") after rediscovering the proteins in the 1920s.[64] Keilin was also responsible for the early classification of cytochromes into groups $a - c$, based on the position of their lowest energy absorption band in their reduced state. For cytochrome a the lowest energy band is found at around 605 nm, for cytochrome b it is in the vicinity of 565 nm, and for cytochrome c it's closer to 550 nm.[65-66] Later, cytochrome d was added to the classification,[67] and more recently cytochrome o[68] and cytochrome $p450$, among others, have joined the pantheon. The monooxygenase cytochrome P450s have been widely studied because of their medically important catalysis of redox reactions of fatty acids, steroids, and xenobiotics in mammals.[69-70] The cytochrome spectroscopic properties reflect the chemical properties of the heme prosthetic group, as will be detailed below for the case of cytochrome c.

Because of their metal-reducing properties, cytochrome c proteins comprise nearly 80% of the total outer membrane protein content in *S. oneidensis*.[23] Membrane proteins are always important to study because more than half of reported therapeutic drugs are based on targeting membrane proteins,[71-72] and approximately 20-30% of all total open reading frames are responsible for encoding membrane proteins.[73-74]

1.3.3. Cytochrome *c* proteins

C-type hemes are structurally unique among the heme prosthetic groups in that the porphyrin rings are covalently bound to the protein backbone. All other hemes are held in place by non-covalent interactions, and by the interaction between the iron and amino acids from the protein backbone at one or both of the iron axial sites. In *c*-hemes, the heme *c* is covalently bound to the protein by two thioether bonds (Fig. 1.4).[66] Characteristically, the bond formation region of the amino acid sequence in the cytochrome *c* family is encoded by the CXXCH motif, where C stands for a cysteine amino acid residue, X for any amino acid residue, and H for histidine. The Sγ atoms from the two cysteines form two covalent thioether bonds with vinyl groups from the porphyrin ring (Fig. 1.4) and the histidine ligand binds to one axial site of the iron. Mammalian cytochrome *c*, the best characterized and most studied protein in the cytochrome family, was discovered over a hundred years ago.[63] In *S. oneidensis* at least 42 types of putative cytochrome *c* proteins have been identified based on the number of CXXCH motifs present in the genome,[75] though Romine et al. eliminated one because of disrupted or truncated genes.[76] Interestingly, most ccNiRs, including *S. oneidensis* ccNiR, are unusual because they contain a CXXCK motif in place of the usual CXXCH motif. This motif is associated with the ccNiR heme active site.[77]

In addition to their role as electron transfer proteins, eukaryotic cytochrome *c*s also appear to play other important ancillary roles. For example, they appear to help trigger apoptosis when they are released from mitochondria into the cytoplasm.[78] Furthermore, in mammalian cells, cytochrome *c*s also show responses to nitrosative and oxidative stress.
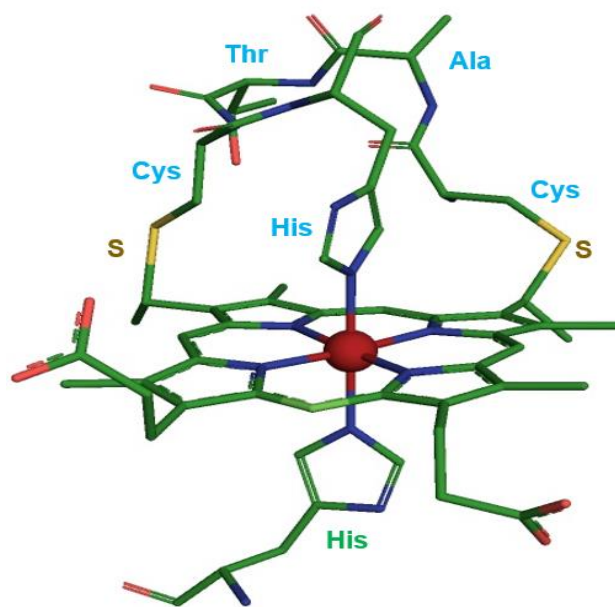
Figure 1.4. The typical *c*-heme, showing the two thioether linkages (yellow) to cysteine residues and bis-histidine coordination to the iron center (red sphere). The typical CXXCH motif for *c*-heme is presented here by Cys-Thr-Ala-Cys-His. Four of five heme centers in each protomer of ccNiR follow this CXXCH pattern, where X can be any amino acid residue. However, the ccNiR active site is unusual in that the proximal site His (H) is replaced by Lys (K) and encoded by a CXXCK motif. The ccNiR active site structure is discussed in detail in the main text. The c-heme image here is taken as an example from the *S. oneidensis* ccNiR enzyme (PDB 6P73).

In prokaryotic cells, the main function of cytochrome *c*s is still in respiration and photosynthesis, but they also play key roles in response to nitrosative stresses.[79] In fact, ccNiRs provide an illustrative example of how one class of *c*-type heme protein may play multiple physiological roles. As communicated above, the main role of ccNiR is to catalyze nitrite ammonification during anaerobic respiration, where nitrite is being used as an electron sink in energy transduction. However, some bacteria that express ccNiR, such as the microaerobic bacterium *Campylobacter rectus*, can't survive if nitrite is the only available electron sink. In the case of *C. rectus* it appears that ccNiR's role is to detoxify nitric oxide by reducing it. In this way, these bacteria are adapted to survive in the human oral cavity and circulatory system, where they are responsible for periodontal disease and formation of arterial wall plaques, among other

pathologies.[80-83] Another interesting example of non-standard ccNiR behavior is provided by the *Campylobacter jejuni* variant, which has a CXXCH motif at the active site instead of the novel CXXCK motif.[84] This ccNiR variant can't readily reduce nitrite, but it does reduce nitric oxide, and so its physiological role is most likely to be mitigation of nitrosative stress.

1.4. Structure of cytochrome *c* nitrite reductase

1.4.1. Typical structural characteristics

CcNiR is a stable, periplasmic, soluble, multi-heme respiratory protein found in a variety of gram-negative bacteria. A recent low temperature crystal structure of *S. oneidensis* ccNiR (1.66 Å, PDB 6P73)[60] and one previously obtained at room temperature using the Laue method (2.59 Å PDB 3UBR)[59] showed that the *S. oneidensis* enzyme is quite similar to homologs from *Wolinella succinogenes,*[85] *E. coli,*[86] *Sulfurospirillum deleyianum* (1.9 Å),[77] *Desulfovibrio desulfuricans,*[87] *Desulfovibrio vulgaris,*[88] and *Haemophilus influenzae*[77] that had been structurally characterized earlier.

The enzyme is a homodimer (Fig. 1.5a); each protomer has five *c* type hemes and a molecular weight that varies from 55 kDa-70 kDa depending on the bacterial source.[3, 89] Four of the hemes (heme #2 to heme #5) are low-spin, bis-his ligated, and interact with the protein backbone through the characteristic CXXCH motif (see the previous section). However, the active site heme #1 is five coordinate, has a high-spin ferric resting state, and unusually, has a lysine (Lys123 in *S. oneidensis*) bound at the proximal site instead of a histidine.[90] This lysine is supplied by the novel CXXCK sequence mentioned earlier. All ccNiRs identified to date have three conserved amino acid active site residues that appear to be critical for optimal catalytic activity. For example, in *S. oneidensis* ccNiR these are Arg-103, Tyr-206, and His-257,[59-60] in *W. succinogenes* they are Arg-

114, Tyr-218, and His-277, and in *S. deleyianum* they are Arg-113, Tyr-217, His-282.[77] (Table 1.2, Fig. 1.6)
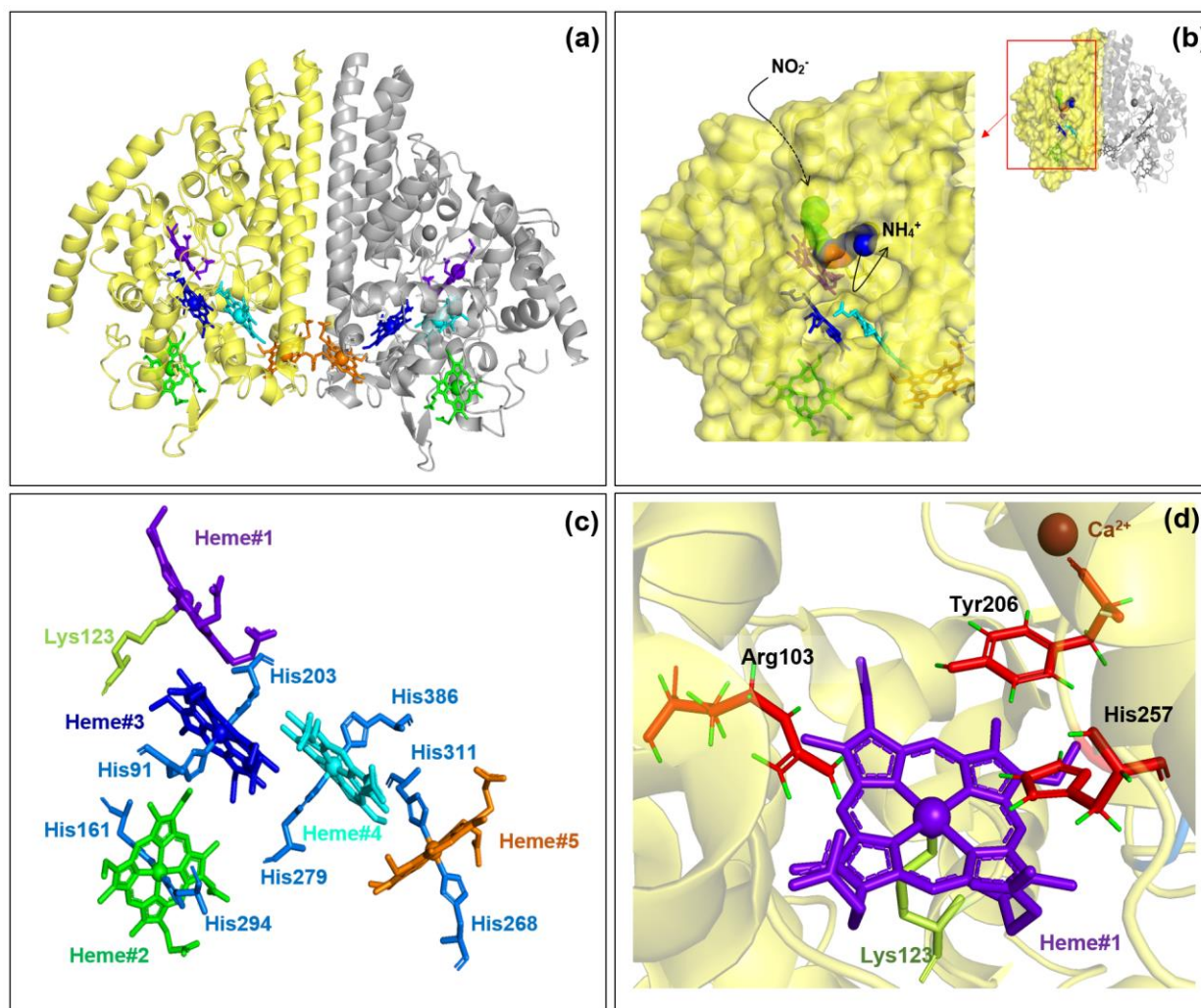
Figure 1.5. (a) The homodimer structure of *S. oneidensis* ccNiR. Each protomer contains five heme centers, heme#1 – heme#5. Heme #2 (green) is considered the electron entering the heme center and heme#1 (purple) is the active site heme in each protomer. Each protomer of *S. oneidensis* ccNiR has one Ca^{2+} ion (*left protomer;* lemon sphere, *right protomer*; gray sphere). **(b)** Zoom-in view of the left side protomer showing the substrate and product channels in the active site heme#1 of ccNiR. The two funnel-like channels were drawn using free software Caver 3.0.3 plugin in PyMol (PDB 6P73). Green balls trace the entry tunnel, with the black dashed line represent the substrate's entry path into the tunnel from the hidden backside. The blue balls trace the possible product release tunnel. **(c)** Ligand orientations for the five ccNiR hemes on one protomer. The histidines on heme#2 – heme#5 are blue sticks, while the unusual lysine ligated to the active site heme#1 is lemon. **(d)** the *S. oneidensis* ccNiR active site heme arrangement with three conserved amino acid residues, R103, Y206 and, H257 (red stick) where green stick representing hydrogen atom.

15

Table 1.2. CcNiR obtained from different species of bacteria comparison

Proteobacteria class	Epsilon (ε)	Delta (δ)	Epsilon (ε)	Delta (δ)	Gamma (γ)	Gamma (γ)
PDB ID	2E80	1OAH	1QDB	6V0A	1GU6	6P73
e⁻ supplier partner	NrfH	NrfH	NrfH	NrfH	NrfB	CymA
Active site residues	Arg-114 Tyr-218 His-277	His-299 Arg-130 Tyr-237	Arg-113 Tyr-217 His-282	Arg-122 Tyr-221 His-278	Arg-106 Tyr-216 His-264	Arg-103 Tyr-206 His-257
Proximal ligand	Lys-134	Lys-150	Lys-133	Lys-133	Lys-126	Lys-123
References	[91]	[92]	[77]	[93]	[86]	[60, 94]

The arrangement of the histidine imidazole planes in 6-coordinate *c*-hemes can range from being completely perpendicular to completely parallel (Fig. 1.5c). This provides an important EPR spectroscopic handle because hemes with parallel imidazoles have rhombic signals whereas hemes with perpendicular imidazoles have very characteristic axial signals. The imidazole plane in heme #2 is close to parallel in all ccNiR homologues characterized so far. However, compared to all other species the imidazole plane of heme #2 from the *S. oneidensis* is more parallel. The imidazole planes in heme#3 are also close to parallel, while those in hemes#4 and heme#5 are perpendicular.[86]

According to an analysis by Page *et al*, electrons can transfer from one redox center to another if the distance between them is less than 14 Å.[95] All the ccNiR heme centers are tightly packed and closely spaced (Fe-Fe distances < 13 Å), which facilitates the shuttling of electrons between them. Heme#2 appears to be the entry point for electrons from the physiological electron

Heme#1

```
G.lovleyi       WKDTALPTP----EGKSKYKKGNDGG-KVYDKLSEYPFIALLFNGWGFGIEYNEPRGHVYMMKDQKEIDRSRL-------KGGGACLTCKTPYAPQLAQKQGVTYFSQSYADAVNQIPKE 163
D.desulfuricans YMKNNEDRIMTDYKGSVPYHKNDNVNPLPKGFKHAQPYLKNLWLGYPFMYEYNETRGHTYAIDDFLNIDRINRFAADGKGNLPATCWNCKTPKMMEWVSQYGDKFWSMDVNEFRAKDKIN 180
W.succinogenes  WKKTKESDNITDM------------------LKEKPALVVAWAGYPFSKDYNAPRGHYYALQDNINTLRTGAPVDGKTGPLPSACWTCKSPDVPRIIEQDGELEYFTGKWA----KYGD 160
S.deleyianum    WKKTKEYDSFTDM------------------LAKDPALVIAWSGYAFSKDYNSPRGHYYALQDNVNSLRTGAPVDAKTGPLPTACWTCKSPDVPRLIEEDGELEYFTGKWA----KYGS 149
E.coli          WKATSEQSERVDA------------------LAEDPRLVILWAGYPFSRDYNKPRGHAFAVTDVRETLRTGAPKNAEDGPLPMACWSCKSPDVARLIQKDGEDGYFHGKWA----RGGP 152
S.oneidensis    WHDTAKSEELVDA------------------LEQDPNMVILWAGYAFAKDYKAPRGHMYAVTDVRNTLRTGAPKNAEDGPLPMACWSCKSPDVPRLIEEQGEDGYFKGKWA----KGGP 149
```

Arginine
Tyrosine   Active Site Residue

Heme#2   Heme#3

```
G.lovleyi       HQEMGVACIDCHNNK-------DMGLKISRGFTLVKALDKMG-VDQTKLTNQDKRSLVCAQCHVTYTIPKDANM-------KSQDVFFPWDESKWG--KISIENIIKKR---------S 257
D.desulfuricans AHDETIGCANCHDPA-------TMELRLYSEP-LKDWLKRSG-KDWQKMSRNEKRTLVCAQCHVEYYFTHKDNG-------PAAKPVFPWDNGFNP------EDMYQYYKGHGAKGPDGK 278
W.succinogenes  EIVNTIGCYNCHDDK-------SAELKSKVPY-LDRGLSAAGFKTFAESTHQEKRSLVCAQCHVEYYFKKTEWKDDKGVDKTAMVVTLPWSKGIST------EQMEAYYDEI-------- 258
S.deleyianum    QIVNVIGCANCHDDK-------TAELKVRVPH-LNRGLQAAGLKTFEESTHQDKRTLVCAQCHVEYYFKKTEWKDAKGADKTAMVVTLPWANGVGKDGNAGVEGMIKYYDEI-------- 263
E.coli          EIVNNLGCADCHNTASPEFAKGKPELTLSRPY-AARAMEAIG-KPFEKAGRFDQQSMVCGQCHVEYYFDGKN-----------KAVKFPWDDGMKV------ENMEQYYDKI-------- 245
S.oneidensis    EVTNTIGCSDCHEK-------GSPKLRISRPY-VDRALDAIG-TPFSKASKQDKESMVCAQCHVEYYFEKKED--------KKGFVKFPWDMGVTV------DQMEVYYDGI-------- 238
```

Heme#4   Heme#5

```
G.lovleyi       DKSYGEWTQAVTGFKMAYIHPEFEMYSNQSVHWMAGVSCADCHMPYTKVGSK-KISDHRI-MSPLKNDFKGCKQCHSESSEWLKNQVITIQD-------RAASQYIRSGYALATVAKLF 336
D.desulfuricans PGPFVDWVHAASKVPMIKMQPEYETFQD-GPHGAAGVSCADCHMQYVREDGK-KISSHWMTSPMKDPEMRACRQCHADKTGEYLR------QRVLYTQQKTFDQLLKAQEMSVKAHEAV 390
W.succinogenes  --NFADWTHGISKTPMLKAQPDWELYKT-GIHGQKGVSCADCHMPYTQEGAV-KYSDHKV-GNPLDNMDKSCMNCHRESEQKLKDIVKQKFERKEFLQDIAFDNIGKAHLETGKA---- 369
S.deleyianum    --NFSDWTHNISKTPMLKAQPGFEFWKS-GIHGQKGVSCADCHMPYTQEGSV-KYSDHQVKENPLDSMDQSCMNCHRESESKLRGIVHQKYERKEFLNKVAFDNIGKAHLETGKA---- 375
E.coli          --AFSDWTNSLSKTPMLKAQPEYETWTA-GIHGKNNVTCIDCHMPKVQNAEGKLYTDHKI-GNPFDNFAQTCANCHTQDKAALQKVVAERKQSINDLKIKVEDQLVHAHFEAKAA---- 357
S.oneidensis    --EFSDWTHALSKTPMLKAQHPEYETWKM-GIHGKNNVSCVDCHMPKVTSPEGKKFTDHKV-GNPFDRFEETCATCHSQTKEFLVGVTNERKAKVKEMKLKAEEQLVKAHFEAAKA---- 350
```

Histidine
Active Site Residue

```
G.lovleyi       EMTHKQ--QAAGKQIDQKMYDQAKFYYEEGFYRNLFFGAENSIGFHNPTEAMRILGDATMYAGKADGLLRQALTKAGVDVPVKIDLELS---KYTNNR------------GAKKLMFKP 440
D.desulfuricans RLANAYEGHRAA-NYE-ALMAEAREMVRKGQLFWDYVSAENSVGFHNPAKALDTLMTSMECSQKAVDL-ATEATDFGIAPALAGDIKKLVPPILTLSRKLQQDPEFLKQNPWTRLLPALP 508
W.succinogenes  --------MELG-ATD-AELKEIRTHIRHAQWRADMAIAGHGSFFHAPEEVLRLLASGNEEAQKARIKLVKVLAKYGAIDY-------V-APDFETKEKAQKLAKVDMEAFIAEKLKFKQ 471
S.deleyianum    --------IEAG-ASD-EELKEVRKLIRHGQFKADMAIAAHGNYFHAPEETLRLLAAGSDDAQKARLLLVKILAKHGVMDY-------I-APDFDTKDKAQKLAKVDIAALAAEKMKFKQ 477
E.coli          --------LDAG-ATE-AEMKPIQDDIRHAQWRWDLAIASHGIHMHAPEEGLRMLGTAMDKAADARTKLARLLATKGITHE-------IQIPDISTKEKAQQAIGLNMEQIKAEKQDFIK 460
S.oneidensis    --------WELG-ATE-AEMKPILTDIRHAQWRWDLAIASHGVAAHAPEEALRVLGTSVNKAADARVKLAQLLAKKGLTDP-------VAIPDISTKAKAQAVLGMDMEKMNAEKEAFKK 453
```

Figure 1.6: Multiple sequence alignment of ccNiR protein from different classes of bacteria. **Blue**: conserved amino acid sequence for the *c*-heme motif (CXXCH). In the active site, the unusual Lysine (K) is highlighted with yellow. **Red**: Conserved histidine residues in the distal site of heme centers which complete the bis-histidine ligated heme center. *G. loveyi* ccNiR contains R122 which is not aligned with other bacterial ccNiR (shown in the dark brown arc). Amino acids not in the active site, and as far as is known, not structurally or catalytically active, are shown in **green**. **Red highlighted**: *G. loveyi* ccNiR, the function of methionine (M255) instead of typical tyrosine is as yet unknown. Arginine (R277) is shown prior to the conserved active site histidine (H) instead of typical glutamine (Q) residue. R277 plays a function similar to that of Ca^{2+} ion in *G. loveyi* ccNiR where Ca^{2+} ion is not present, as discussed in detail in the main text.

donors. [86] [88] From there, the electrons can shuttle from heme to heme to the active site on the same protomer. Alternatively, as hemes#5 from the two protomers are closely spaced, electrons may jump from one protomer to the other, and make their way to the second protomer's active site (Fig. 1.7).[89]

Einsle et.al. first detected the presence of a calcium ion close to the active site of *S. deleyianum* ccNiR in their X-ray crystal structure, which was further confirmed by the ICP mass spectrometry.[77] Calcium ions have since been found in virtually all the other homologous ccNiRs structurally characterized to date, including the *S. oneidensis* enzyme,[92, 96-98] though at present their role in the enzyme is unclear. Based on the calcium ion's closeness to the active site (10.7 Å) and other structural clues, it is hypothesized that Ca^{2+} may facilitate proton delivery during catalysis. The possible roles of Ca^{2+} are further discussed in Section 1.6.2.4 below.
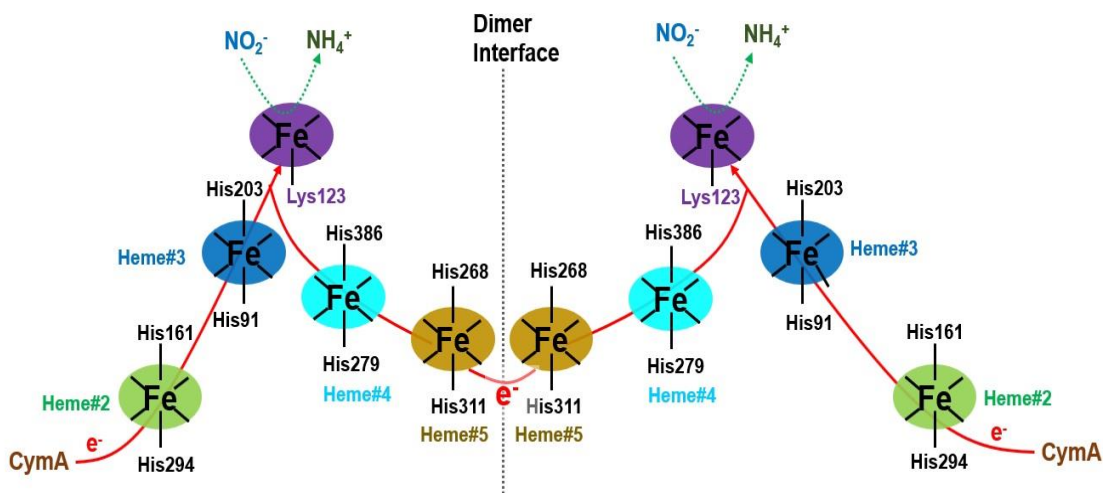
Figure 1.7. The heme arrangement within the *S. oneidensis* ccNiR dimer (dotted line separates the protomers). The electron entering heme#2 (green) and electron transferring heme#3 (blue), heme#4 (cyan) and heme#5 (orange) are bis-histidine ligated (6-coordinate). The active sites heme1# (purple) have unusual Lys at 123 (5-coordinate) and the distal site open for binding substrate nitrite.

Alpha helices are the main secondary structural motif in ccNiR (Fig. 1.8). At the end of the peptide chain, four long helices and four short turns are present. Two short antiparallel beta-sheets are found in each protomer and one of these is found close to the active site and appears to form a funnel-like structure that facilitates substrate entry (Fig. 1.5b). The dimer interface of ccNiR is mainly formed by two helices, dubbed *h22* and *h25* by Einsle et al,[77] where *h25* has direct interaction with the other protomer (Fig. 1.8). The dimer interaction consists of approximately 28 amino acid residues along a 42 Å stretch, which is also 8.5% of the total accessible surface area of a protomer.[77]
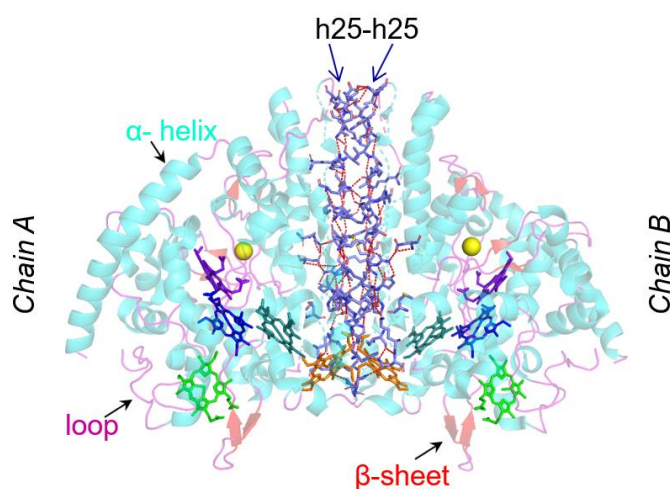
Figure 1.8. The ccNiR structure showing the helix (cyan), loop (pink), and sheet (red) form. The *helix25s* are shown here as sticks (blue) and the polar interactions between amino acids are shown as red dotted lines.

1.4.2. Atypical nitrite ammonifying enzymes

A few *Thialkalivibrio* species of bacteria (*T. nitratireducens and T. paradoxus*) have a homohexameric ccNiR consisting of eight hemes per protomer, where each protomer has two domains. The N-terminal domain contains a unique fold and three hemes, while the C-terminal contains the remaining five hemes in the typical pattern seen in *S. oneidensis*. Interestingly, the *Thialkalivibrio* pentaheme sequence has only approximately 20% sequence homology with the analogous *S. oneidensis* domain, but their main catalytic amino acid residues, calcium metal-binding site, and lysine bound in the proximal site are all conserved. The ccNiR enzyme from *T. nitratireducens* (also referred as TvNiR) shows a covalent modification between amino acid Y(331) and C(333) which is another significant difference from the more typical bacterial ccNiRs such as that from *S. oneidensis*.[99] A third difference is found in the architecture of the substrate entry and product exit channels.[99-102]

A crystal structure from *Geobacter lovleyi* ccNiR (2.55 Å resolution, PDB 6V0A) has recently revealed that, unusually, Ca^{2+} is not present in this form of the enzyme. Instead, an arginine, R277, appears to provide the electrostatic stability and hydrogen-bonding network normally provided by Ca^{2+} in the active site. The catalytic properties of *G. lovleyi* ccNiR are similar to those of other bacterial ccNiRs.[93] A more in-depth comparative analysis of *G. lovleyi* ccNiR relative to the Ca^{2+} containing variants is presented in Section 1.6.2.4 below.

1.5. The bioenergetics of nitrite ammonification

During ccNiR-mediated anaerobic respiration, nitrite is the primary electron acceptor and formate the electron donor, with the NAD^+/NADH couple mediating the electron transport.[6, 103] However, the bioenergetics are not straightforward because many processes are intertwined. Ammonification can also serve to decrease nitrogenous oxidative stress molecules such as nitric

oxide, hydroxylamine, and O-methyl hydroxylamine (CH_3ONH_2) to ammonium, and in addition, ccNiR can reduce sulfite to sulfide at significant rates,[3, 104-105] thus bridging the sulfur and nitrogen cycles.[84, 96, 105-108]

The δ, ε, and γ-proteobacteria have different electron transport proteins to directly supply electrons to ccNiR's heme#2 (Table 1.2), which is the physiological entry point for electrons.[86, 109] In *S. oneidensis*, a γ-proteobacterium, the electrons are supplied by CymA (**Cy**toplasmic **m**embrane protein **A**), which is an inner membrane-anchored electron transport protein (Fig 1.9). Interestingly, in *E. coli* which is also a γ-proteobacterium, the electron source is NrfB, a periplasmic pentaheme protein with molecular weight ~21 kDa.[21, 86, 110-113] Perhaps reflecting the difference in electron donors, the *S. oneidensis* and *E. coli* structures, which are otherwise very similar, are most different on the protein surface surrounding the heme 2-electron entry point (Fig. 1.10). This has some interesting effects on the ccNiR electrochemistry.[89] NrfH, another cytoplasmic membrane-anchored protein with MW~20 kDa, is the electron supplier for *W. succinogenes*, an ε-proteobacterium,[11, 85, 104] and for *D. desulfuricans*[87] and *D. vulgaris,*[88, 114] both δ-proteobacteria.

In *S. oneidensis*, the CymA protein sits at a branch point from where it can distribute electrons to several periplasmic reductase proteins (Fig 1.10). Unsurprisingly then, mutation of CymA blocks not only ccNiR activity but also other conversions, such as fumarate to succinate and DMSO to dimethyl sulfide. The Cytochrome periplasmic **m**etal-**r**educing protein **A** (MtrA) is also part of the complex electron transport system mediated by CymA. MtrA, together with another periplasmic protein MtrB and the outer membrane protein MtrC, are involved in the respiratory extracellular reduction of insoluble metals such as manganese dioxide.[115]

In addition to CymA, the respiratory fumarate reductase (FccA) also plays a central role in the multifaceted *S. oneidensis* electron transport system (Fig. 1.10). It is a soluble monomeric protein and responsible for reducing fumarate to succinate using the electrons supplied by CymA. However, in *S. oneidensis*, it plays an additional role not observed in other organisms: it appears to store electrons temporarily, thus acting as an intermediate electron acceptor during the temporary absence of a suitable terminal electron acceptor.[116-118]
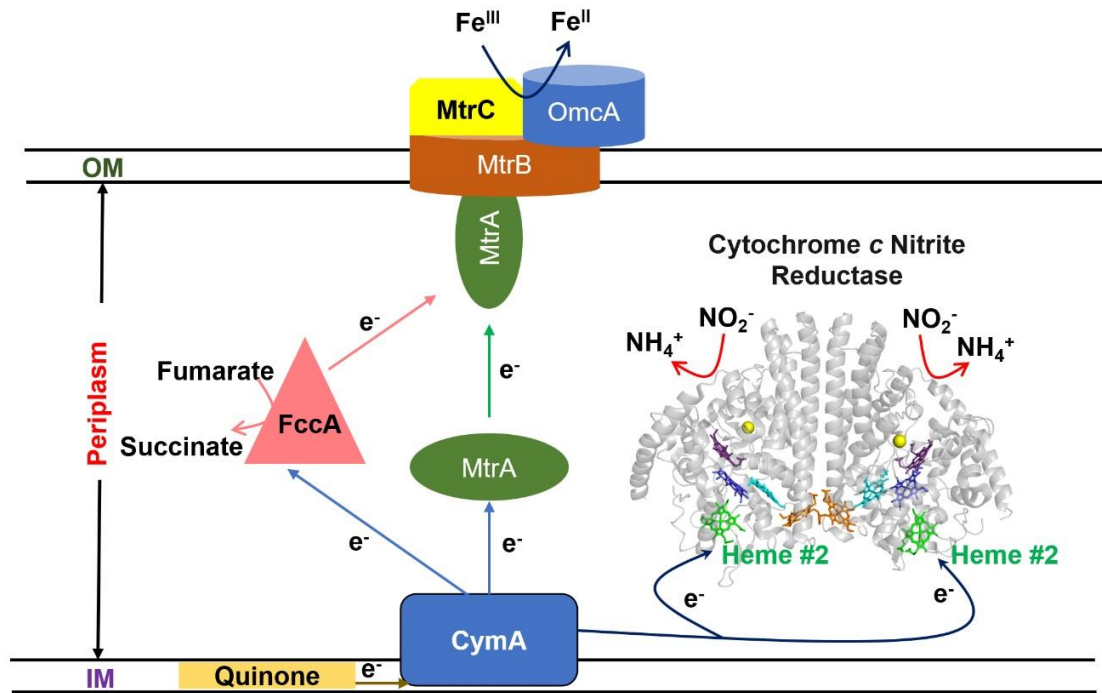
Figure 1.9. The inner membrane protein, CymA, anchors the electron distribution to multiheme respiratory proteins including the periplasmic ccNiR. CymA also provides electrons to MtrA which ultimately transports electron to the extracellular surface (MtrC and OmcA).
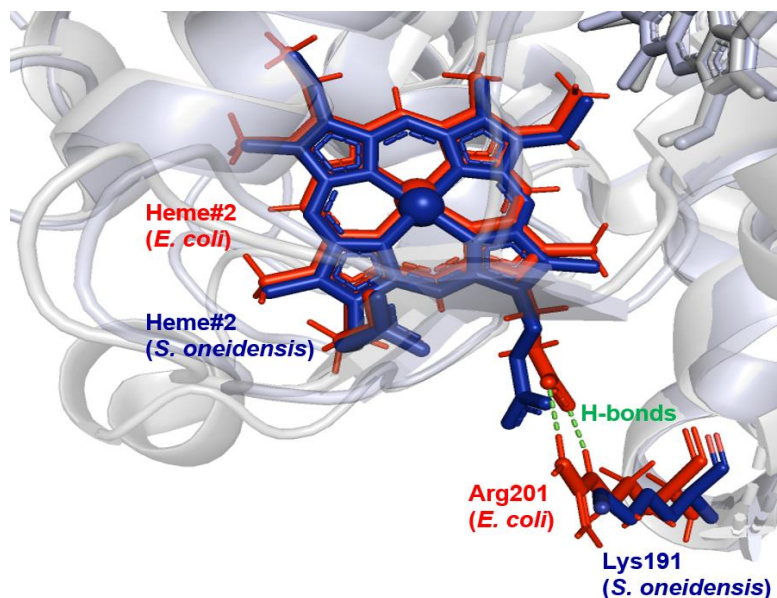
Figure 1.10. Heme#2 alignment between *S. oneidensis* (darkblue) and *E. coli* (red*)* ccNiR. The *E. coli* ccNiR propionate chain is less solvent-exposed and forms hydrogen bonds (green dotted lines) with Arg-201, whereas in *S. oneidensis*, the propionate chain is more solvent-exposed and forms no hydrogen bond with similarly aligned Lys191.
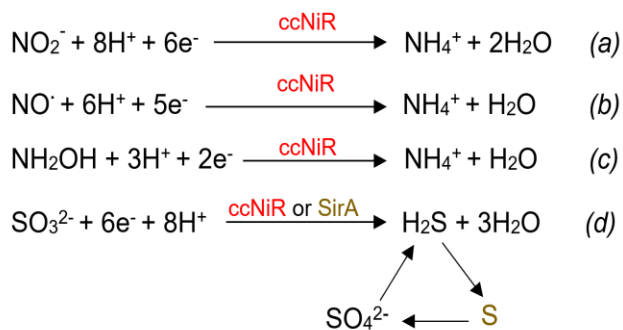
Scheme 1.1. Reactions catalyzed by ccNiR under standard assay conditions. The strong reductant methyl viologen monocation radical, MV_{red}, is used as the electron donor. Sulfite reduction by ccNiR is shown here with a dotted arrow (d) to emphasize that the reduction is normally catalyzed by the SirA enzyme. By doing sulfite reduction ccNiR also couples the nitrogen cycle with the sulfur cycle.

23

1.6. The ccNiR reaction mechanism

1.6.1. Overview

The ccNiR-catalyzed nitrite ammonification pathway is fascinating in its complexity, involving as it does the transfer of a total of six electrons and eight protons in proton-coupled electron transfers (PCETs) at the ccNiR active site heme center. The standard in vitro assay for ccNiR uses methyl viologen monocation radical (MV_{red}, $E^o = -0.445$ V) as the nitrite reducing agent (Scheme 1.1). Ammonium is the sole free nitrogenous product in the MV_{red} assay, and no enzyme intermediate has ever been detected with the assay either.[77, 80, 86, 94] This is in keeping with the prediction that each successive reduction step increases the protonation affinity, which in turn increases the affinity for the next reduction.[61] Despite the absence of detectable intermediates though, researchers soon surmised that nitrite reduction proceeded through catalytic intermediates that had $NO^·$ and hydroxylamine bound at the active site because both of these species are also substrates for ccNiR in the standard assay (Scheme 1.1).[77, 86-87, 91-92] Over the years several computational studies, together with assessment of the existing ccNiR crystal structures, have provided additional insights regarding the possible ccNiR mechanism. Section 1.6.2 below summarizes the mechanistic hypotheses that have been developed on the basis of structural and computational studies, together with the data that support these hypotheses.

Despite the early conclusions to the contrary, recent reports by the Pacheco group have demonstrated that putative catalytic intermediates *can* be trapped and studied, if ccNiR-catalyzed nitrite reduction proceeds under more weakly reducing conditions than are provided in the MV_{red} assay.[59, 97-98, 119] These reports are summed up in Section 1.6.3. The theoretical and experimental studies reviewed in Sections 1.6.2 and 1.6.3 provided the starting point for the investigations described in this thesis, whose goals are summarized in Section 1.7.

1.6.2. Structural and computational analyses of the ccNiR mechanism

    1.6.2.1. The resting enzyme and nitrite activation at the active site. Initially, the ccNiR active site was surmised to be 5-coordinate or to have water bound at the distal site, on the basis of spectroscopic studies.[120-122] Since then, resting-state ccNiR has been crystallized with a variety of ligands occupying the active site distal position.[29] For example, the *E. coli* and *S. oneidensis* enzymes have been crystallized with water or hydroxide in the distal position,[60, 86] while the *W. succinogenes* and *S. deleyianum* structures were obtained with sulfate in this position.[77] The *W. succinogenes* structure was also obtained in the presence of the physiological substrate nitrite, and of the putative reaction intermediate, hydroxylamine.[91] Azide is an inhibitor for ccNiR, but it does not bind the active site.[85] In a series of computational studies, the Neese group analyzed the ccNiR mechanism, using the experimental structures as benchmarks for calibrating their calculations.[123-126 123]

    The Neese group first modeled the resting enzyme with water at the distal site. They calculated an iron – oxygen distance of 2.106 Å for water bound to the ferric heme,[123, 125] which is in good agreement with the experimental structure (2.1 Å).[91] However, the calculations predicted that the resting active site should be low-spin, whereas EPR studies show it to be high-spin.[89-90, 127 128] This is unsurprising, as the density functional methods used in the calculations are known to overestimate the stability of lower spin states.[125] Despite this limitation, the calculations could be used to do comparative studies. For example, the calculations show that water will be weakly bound in both the ferric and ferrous state, with binding energies of -10.8 and -5.6 kcal/mol for the ferrous and ferric complexes, respectively, and that upon reduction, the iron – oxygen bond length should increase from 2.106 Å to 2.134 Å.
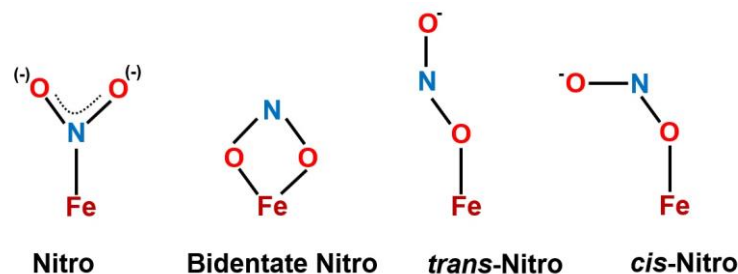
Figure 1.11. Various possible binding modes of nitrite when it binds with iron. The figure drawn here shows binding mode *possibilities* only. The bond lengths, angles, and other parameters are ignored here.

The catalytic process starts when the substrate, nitrite, binds to the heme#1 distal site. Nitrite is an ambidentate ligand that can, in principle, bind metals via either a nitrogen or an oxygen donor atom, to give the nitro or nitrito forms, respectively (Fig. 1.11). In addition, the nitrito form has *cis* and *trans* isomers, as well as a bidentate form in which both oxygens bind to the metal center (Fig. 1.11). Both nitro and nitrito forms are known in heme chemistry. For example, the nitrito isomer was found in horse-heart myoglobin[129] and human myoglobin,[130] in which the proximal site is typically histidine bound. In the case of ccNiR, the 2002 structure of the *W. succinogenes* homologue displayed the nitro isomer.[91] The theoretical calculations by Bykov and Neese also predicted that binding via oxygen should be 4 kcal/mol less favorable than binding via nitrogen.[123] The calculations suggest that the proximal lysine ligand plays a role in stabilizing the nitro form, as do the positively charged amino acid residues that line the active site and interact with the N-bound nitrite's oxygen atoms.[91, 123, 125] In the *S. oneidensis* homologue the positively charged amino acids that stabilize the nitro form are His257 and Arg103.[94]
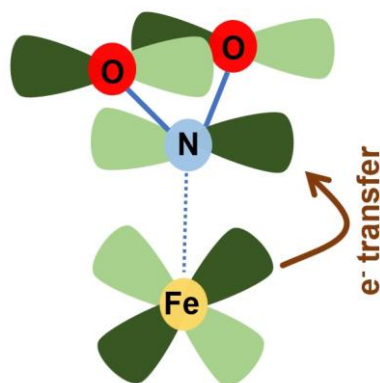
Figure 1.12. Back-bonding interaction between the ccNiR active site heme (ferrous iron) and the physiological substrate nitrite. The iron d_{xz} orbital interacts with the NO_2^- molecule's lowest unoccupied molecular orbital, which has an antibonding character with regard to the N-O bond.

DFT calculations predict that the Fe-N bond becomes significantly stronger when the nitrite-loaded active site is reduced. This can be attributed to π-backbonding from the more electron-rich ferrous iron into the nitrite π-antibonding orbital (Fig. 1.12). As a consequence of π-backbonding the Fe^{II}-N bond length is calculated to be a short 1.877 Å. At the same time, as mentioned earlier, the Fe – O bond distance of active site-bound water lengthens from 2.106 Å to 2.134 Å upon heme reduction, which facilitates replacement of the water by nitrite upon reduction. The driving force for the replacement was calculated to be −39 kcal/mol.[125] In addition to shortening the Fe – N bond, π-backbonding also weakens the nitrite N – O bond as it adds electron density to the antibonding orbital. This results in N – O bond elongation, which facilitates the subsequent heterolytic cleavage of one of the N-O bonds.[91, 123, 125, 131-132] The active site amino acid residues (R103, Y206, H257 in *S. oneidensis* ccNiR) form an electropositive environment that fine-tunes the iron-nitrite π-backbond to optimize for subsequent PCET reactions.[92, 125]

1.6.2.2. The Possible Pathways for the First N−O Bond Cleavage. The theoretical work of the Neese group explored the role of the three conserved active site residues (Arg103, Tyr206, and His257 in *S. oneidensis*) in mediating the first N – O nitrite bond cleavage. At physiological pH, the Arg and Tyr must be protonated since their side-chain pK_a values are expected to be around 12.5 and 10.1, respectively, based on the pK_as of the free amino acids. The pK_a of the His side chain ($pK_a = 6.0$ in the free amino acid) is close to the physiological level, which indicates it can be protonated or deprotonated. Bykov and Neese computationally explored two reaction pathways, the first assuming that His was initially protonated, the second that is was deprotonated.[123, 125]

When His was initially protonated ($HisH^+$) the theoretical analysis of Bykov and Neese ruled out Tyr as the proton donor leading to HONO formation because the product Fe(HONO) adduct was unstable. This adduct was stable when either Arg or $HisH^+$ was the proton donor; however, proton transfer from Arg was highly endergonic ($\Delta G = +17.7$ kcal/mol) while proton transfer from $HisH^+$ was much more thermodynamically feasible ($\Delta G = +4.9$ kcal/mol). The latter is still endergonic, but this is manageable if the Fe(HONO) is continually removed by subsequent reactions. The calculations also showed a reasonable activation barrier for proton transfer from $HisH^+$ to bound nitrite ($\Delta G^{\ddagger} = +5.5$ kcal/mol).[123]

The crystallographic evidence supports the theoretical conclusions.[91, 133-134] According to the crystal structure of nitrite-bound ccNiR, the active site His is very close (2.6 Å) to one of the nitrite oxygen atoms. The active site Arg is close, but not as close, to the second nitrite oxygen (2.8 Å).[91] Bykov and Neese calculate an H-bonding distance of 1.56 Å for the nitrite -HisH+ interaction and 2.67 Å and 2.30 Å for the two Arg interactions.[123] Tellingly, an H-bonding interaction is also seen between Arg and O in the hydroxylamine-bound ccNiR crystal structure

(3.0 Å), whereas the His – O hydrogen bond is missing in this structure,[91] suggesting that the oxygen that interacted with HisH$^+$ in the nitrite structure has now been cleaved.

To cleave the first N-O bond completely, two protons need to be transferred to the O leaving group. So, the question arises: which amino acid donates the second proton? Again, Bykov and Neese examined each possibility computationally.[123] Protonation by Tyr or Arg both had activation barriers (+37.5 kcal/mol and +24.4 kcal/mol, respectively) that substantially exceeded the barrier predicted from experimental results (+15.2 kcal/mol),[96, 106] which left only His. Bykov and Neese showed that His could be re-protonated if the Fe-bound HONO temporarily rotated towards Tyr at an energy cost of +4.2 kcal/mol. This, together with the +7.9 kcal/mol cost of His reprotonation, provided an activation barrier of +12.1 kcal/mol, in the range of the experimental predictions.[96, 106] The calculations also showed that subsequent proton transfer from HisH$^+$ and hydrolysis of the resulting H$_2$ONO could proceed with no further activation barrier.

In calculations where the active site His was taken to be deprotonated at the start of the reaction, Bykov and Neese showed that the lowest energy path involved successive protonations of the nitrite oxygen leaving group by the active site Arg, which was reprotonated after each proton transfer step.[123] In this case, the first activation barrier was 16.7 kcal/mol and the second 17.2 kcal/mol. These activation barriers are higher than those calculated when HisH$^+$ is the proton donor, but they are nevertheless in the range of the +15.2 kcal/mol barrier predicted from experimental results.[96, 106] Taken together, the conclusions of Bykov and Neese suggest that while ccNiR may use HisH$^+$ as the proton donor at low pH, it should still be able to catalyze the first N – O nitrite bond cleavage fairly rapidly at high pH by using Arg as an alternate proton source.

1.6.2.3. Heme iron-nitrosyl intermediates and the second N – O bond cleavage. The Neese computational group analyzed the reduction steps that follow cleavage of the first N – O bond in two detailed articles,[124, 126] and a review.[125] The analyses looked at the changes occurring at the heme#1 center, as well as the protonation states of the three conserved active site amino acid residues known to be directly involved in catalysis (see above). This section summarizes the key results of the analyses, using a modified version of the shorthand used by Bykov and Neese in their papers (Scheme 1.3).

Following cleavage of the N – O bond in nitrite bound to ferrous heme, one obtains an iron nitrosyl species referred to as $\{Fe_{H1}NO\}^6$ using the Enemark-Feltham notation (Scheme 1.2).[135] This species is, in turn, reduced by two more electrons, to generate iron nitrosyl species referred to as $\{Fe_{H1}NO\}^7$ and $\{Fe_{H1}(HNO)\}^8$ (Scheme 1.3).[135] The $\{Fe_{H1}NO\}^6$ reduction to $\{Fe_{H1}NO\}^7$ (Step 1, Scheme 1.3) was predicted to be highly exergonic,[124] a prediction that is consistent with later experimental results in our laboratories (see Section 1.6.3 below). Bykov and Neese analyzed the sequential reductions computationally to assess the roles of the conserved active site amino acids.[124-125] In the $\{Fe_{H1}NO\}^7$ state, Arg103 was protonated, but His257 remained unprotonated (Scheme 1.3). The $\{Fe_{H1}NO\}^7$ state was calculated to be a thermodynamic minimum; however, the species could be reduced in a CPET step to $\{Fe_{H1}HNO\}^8$, in a nearly thermoneutral process with a 6.5 kcal/mol activation barrier (Step 2, Scheme 1.3).[124]

$$\{FeNO\}^6 = [Fe^{II}(NO^+) \longleftrightarrow Fe^{III}(NO^\cdot)]$$
$$\{FeNO\}^7 = [Fe^{II}(NO^\cdot) \longleftrightarrow Fe^{III}(NO^-)]$$
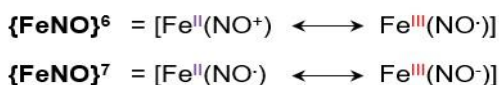
Scheme 1.2. Enemark – Feltham notation used to represent iron nitrosyl species for which the electron distribution is uncertain.[135]

$$\{Fe_{H1}NO\}^6 H_Y H_R \xrightarrow{\ e^-\ } \{Fe_{H1}NO\}^7 H_Y H_R \qquad (1)$$

$$\{Fe_{H1}NO\}^7 H_Y H_R \xrightarrow[PCET]{\ H^+,e^-\ } \{Fe_{H1}HNO\}^8 H_Y H_R \qquad (2)$$

$$\{Fe_{H1}HNO\}^8 H_Y H_R \xrightarrow[slow]{\ H^+\ } \{Fe_{H1}HNO\}^8 H_Y H_R H_H \qquad (3)$$

$$\{Fe_{H1}HNO\}^8 H_Y H_R H_H \xrightarrow[PCET]{\ H^+,e^-\ } [Fe_{H1}^{II} H_2 N\dot{O}] H_Y H_R \qquad (4)$$

$$[Fe_{H1}^{II} HN\dot{O}] H_Y H_R \xrightarrow{\ H^+,e^-\ } [Fe_{H1}^{II} H_2 NOH] H_Y H_R \qquad (5)$$

$$[Fe_{H1}^{II} H_2 NOH] H_Y H_R \xrightarrow[slow]{\ H^+\ } [Fe_{H1}^{II} H_2 NOH] H_Y H_R H_H \qquad (6)$$

$$[Fe_{H1}^{II} H_2 NOH] H_Y H_R H_H \xrightarrow[slow]{} [Fe_{H1}^{II} H_2 N^+] H_Y H_R + H_2O \qquad (7)$$

$$[Fe_{H1}^{II} H_2 N^+] H_Y H_R \xrightarrow{\ e^-\ } [Fe_{H1}^{II} H_2 \dot{N}] H_Y H_R \qquad (8)$$

$$[Fe_{H1}^{II} H_2 \dot{N}] H_Y H_R \xrightarrow{\ H^+\ } [Fe_{H1}^{II} H_2 \dot{N}] H_Y H_R H_H \qquad (9)$$

$$[Fe_{H1}^{II} H_2 \dot{N}] H_Y H_R H_H \xrightarrow[PCET]{\ H^+,e^-\ } [Fe_{H1}^{III} H_3 N] H_Y H_R \qquad (10$$

Scheme 1.3. Some of the catalytic steps proposed for the reduction of nitrite to ammonia at the ccNiR active site, based on computational analysis.[124-126, 135] The heme-bound nitrosyl species are represented by their Enemark-Feltham notations (Scheme 1.2). When present in protonated form, the catalytically important conserved active site amino acids are labeled as follows (using *S. oneidensis* numbering): H_Y, Tyr-206; H_R, Arg-103; H_H, His-257. This shorthand is adapted from that used by Bykov and Neese,[126] but with some modifications. PCET: Proton Coupled Electron Transfer.

Reduction of $\{Fe_{H1}HNO\}^8$ is prohibitively endergonic unless it is coupled to proton transfer, and Bykov and Neese's calculations suggest that this first requires a rate-limiting protonation of His 257 (+12.9 kcal/mol, Step 3, Scheme 1.3).[126] There are two energetically plausible products of $\{Fe_{H1}HNO\}^8$ reduction, and Step 4 of Scheme 1.3 shows the one that is most consistent with our experimental results, the ferrous $[Fe_{H1}H_2NO^\cdot]$ (see Section 1.6.3 below).

Sequential protonation and reduction of the active site moiety next generates the ferrous hydroxylamine-bound intermediate, [$Fe_{H1}H_2NOH$] (Step 5, Scheme 1.3).

The final stage in the catalytic cycle is the reduction of bound hydroxylamine to ammonia, and both the computational studies[126] and experimental results from our laboratories (Section 1.6.3 below) suggest that this is an energetically expensive process. The computational studies unambiguously show that the rate limiting step is hydroxylamine dehydration, which requires a prior protonation. The lowest energy pathway requires an initial protonation of His 257 at a cost of 5 kcal/mol (Step 6, Scheme 1.3), followed by proton transfer to the hydroxylamine oxygen and subsequent dehydration (Step 7, Scheme 1.3). This step is highly endergonic (9.0 kcal/mol), and has an activation barrier of 12.2 kcal/mol.[126] Experimental results (Section 1.6.3 below) suggest that this may be the overall rate-limiting step in nitrite reduction to ammonia, at least at pH 7.0; however, the activation energy is still within the range of the +15.2 kcal/mol barrier predicted from experimental results.[96, 106] It should be noted that, while protonated histidine provides the lowest energy pathway to hydroxylamine dehydration, calculations show that protonation by Tyr-206 is also feasible. Indeed, Bykov et al. favor the tyrosine pathway because this amino acid appears to be essential for efficient hydroxylamine reduction.[126]

Once hydroxylamine has been dehydrated, the subsequent reactions are all highly exergonic, with steps 8-10 of Scheme 1.3 showing one plausible sequence to heme-bound ammonia. Two important conclusions came from the computational analysis of the final steps. First, the final nitrogenous product has ammonia bound to ferric heme. Second, the rate of dissociation of the bound ammonia is governed by a switch from a low-spin to high-spin ferric state as the Fe – N bond lengthens; the low spin state energy increases as the bond lengthens,

whereas the high-spin state energy decreases. The activation barrier for the dissociation is the point at which the low-spin and high-spin potential energy surfaces cross.[126]

1.6.2.4. Possible roles for the Ca^{2+} ion. Einsle et.al. first noted a calcium ion close to the active site of *S. deleyianum* ccNiR by X-ray crystallography and confirmed its presence by ICP mass spectrometry.[77] Since then Ca^{2+} has been found in all but one of the ccNiR homologues that have been structurally characterized to date. That Ca^{2+} plays a very important role in the active site stability/catalytic activity is confirmed by mutating the amino acid residues that interact directly with the cation. In *E. coli*, ccNiR variants with an altered Ca^{2+} environment exhibit significantly different active site midpoint potentials.[136] The presence of external Ca^{2+}, or Ca^{2+} chelators, in the ccNiR solution buffers has been found to affect some ccNiR preparations but not others. For example, *S. deleyianum* ccNiR activity increases in the presence of added Ca^{2+}, and decreases by 50% in the presence of added EDTA,[96] but neither of these additives has any effect on the activity of the *S. oneidensis* enzyme.[94] Adding other divalent cations like Mg^{2+} cannot compensate for *S. deleyianum* ccNiR activity under limited Ca^{2+} concentration. Interestingly, adding Zn^{2+} slows down the ccNiR activity significantly.[136]

Though Ca^{2+} has now been found in virtually all ccNiR homologues,[92, 96] its role in the enzyme remains unclear. Based on its structural properties and close proximity to the active site (10.7 Å), it is hypothesized that the Ca^{2+} ion may indirectly facilitate proton delivery during catalysis by stabilizing OH$^-$ that is formed as H$^+$ is donated to the nitrogenous intermediates in CPET.[125] The Ca^{2+} ion can also form hydrogen bonds with the conserved active site amino acid residues to provide stability,[92] and to provide a positive electrostatic potential that encourages substrate nitrite's entry to the active site.[92, 125]

The architectural position of Ca^{2+} ion in CcNiR and peroxidase enzymes (classes II and III) are similar and can serve to restrict His residues from binding to the Fe atom in the heme active site. In all these enzymes, the metal ion Ca^{2+} inhibits a conserved His residue from binding the Fe atom in the active site which would result in catalyst deactivation. Experiments with *P. chrysosporium* lignin and manganese peroxidase enzymes showed that when the calcium ion is missing, the enzymes lost their activity because a conserved His was then bound to the heme iron.[137]

A second Ca^{2+} ion binding site was observed close to heme #3 and heme #4 of ccNiR in many γ and ε proteobacteria (but not in *S. oneidensis* ccNiR), as well as in TvNiR from *Thioalkalivibrio nitratireducens*. The role of this second Ca^{2+} ion is still unknown.[86, 88, 92] The second Ca^{2+} is far from the active sites, approximately 14 Å[92], and has different ligation arrangements in ccNiR and TvNiR. In all cases, the second Ca^{2+} ion is octahedrally coordinated by the propionate groups of heme #3 and heme #4, the carbonyl oxygen from a Proline (P91 for γ and ε proteobacterial ccNiR, P144 for TvNiR).[85, 136, 138-139] The second Ca^{2+} ion is also ligated with at least two or three water molecules. A second Ca^{2+} is also seen in δ-proteobacterial ccNiR, but its ligation is different again. The second Ca^{2+} is not ligated with any water molecules and instead, it is ligated exclusively by amino acid residues.[92, 139-140] The solvent excluding the arrangement of Ca^{2+} coordination in δ-proteobacteria makes this metal less mobile.

Interestingly, the recently crystallized *G. lovleyi* ccNiR (2.55 Å) has revealed a new ccNiR structure where the primary Ca^{2+} is not present. Instead, R277 provides the electrostatic stability and network in the active site normally provided by Ca^{2+}. The catalytic properties of *G. lovleyi* ccNiR are similar to all other bacterial ccNiR. *G. lovleyi* ccNiR also effects one-step nitrite ammonification in a six-electron reduction reaction without releasing intermediates. Here, the side

chain of R277 forms two salt-bridges with the side chain oxygens of E263. The R277 side chain and carbonyl group form two more hydrogen bonds with the carbonyl group and the side chain of conserved Tyr-221, respectively. Unlike, *E. coli* and like *S. oneidensis* one water molecule was found close to the R277 and forms a hydrogen bond with the side chain of R277. Additionally, the R277 shows a π-cationic interaction with Y221 which facilitates the proper arrangement of Tyr and His. Site-directed mutagenesis experiments also confirmed the importance of R277: R277K or R277Q variants of *G. lovleyi* ccNiR showed less than 3% activity compared to wild type ccNiR.[93]

1.6.2.5. The roles of non-active conserved amino acids in the active site cavity.

In addition to the three active site amino acids that appear to be directly involved in the ccNiR catalytic cycle (R103, Y206, and H257 in the *S. oneidensis* enzyme) several other active site residues are strictly conserved in ccNiR homologues (Fig. 1.6). The exact role of these amino acids is still unknown, but surely, they play a role in catalysis. The crystal structure has shown that Y235 (*S. oneidensis*) helps form a network with water molecules in the active site cavity. The homologous amino acid in *W. succinogenes* is Y218, and a site-directed mutagenesis study of the Y218P variant revealed very low catalytic activity for nitrite ammonification, 0.7% compared to the wild type.[107] However, the mutation did not disrupt the enzyme's conformation.

A conserved glutamine is another important amino acid in the ccNiR active site cavity (Gln263 in *E. coli*, Gln256 in *S. oneidensis*). The amide oxygen of Gln (Q) forms a hydrogen-bonding network to the active site Ca^{2+}. The Q263E ccNiR variant (*E. coli*) showed no catalytic or conformational disruption, probably because glutamine and glutamate occupy almost the same volumes. However, the variant displayed a significantly higher K_m value (10-fold). One possible explanation for the increased K_m is that the amide group of Gln is neutral at pH 7.0 and forms only

monodentate ligation with the active site Ca^{2+} ion, whereas the mutant Glu is negatively charged and can ligate in a bidentate fashion, which disrupts the conserved water molecule's orientation. A second possible reason for the high K_m in the variant is that introducing the negatively charged Glu into the active site may play a repulsive role for the negatively charged substrate nitrite and thus lower the active site potential.[136, 139]

1.6.3. Detection of catalytic intermediates under weakly reducing conditions

1.6.3.1. Detection of high potential intermediates. As mentioned earlier, under standard assay conditions ccNiR catalyzes nitrite reduction to ammonia by MV_{red} in a single six-electron step, without detected intermediates (Scheme 1.1a). Based on these results it had long been assumed that ammonia was the sole product of ccNiR-catalyzed nitrite reduction in vivo as well. A comparison of protein film voltammetry (PFV) and spectropotentiometric experiments with *S. oneidensis* ccNiR first caused the Pacheco group to question this assumption. The PFV experiments showed that no ammonia formation occurs at potentials above −120 mV vs SHE,[94, 97, 119] though the process should be favorable at potentials as high as 0 mV (Fig. 1.13). On the other hand, UV/Vis- and EPR-spectropotentiometric studies showed that the ccNiR active site, when occupied by the strong-field ligand cyanide, had a midpoint potential of +20 mV vs SHE,[89] well above the potential required for the onset of catalysis. As N-bound nitrite is also a strong-field ligand, these results raised the possibility that ccNiR with nitrite bound to the active site would also be reduced at a potential well above that required for the onset of catalysis. A subsequent report from the Pacheco research group proved this conjecture.[98] UV/vis spectropotentiometry showed that nitrite-loaded *S. oneidensis* ccNiR is reduced in a concerted 2-electron step to generate the $\{Fe_{H1}NO\}^7$ moiety at the active site (see Step 1, Scheme 1.3), with an associated midpoint potential of +246 mV vs SHE at pH 7.0.[60] This is 220 mV higher than the midpoint potential for

reduction of cyanide-loaded ccNiR, and over 350 mV above the potential at which the onset of catalysis is observed in PFV experiments (Fig. 1.13). Thus, these results suggest that $\{Fe_{H1}NO\}^7$ is a catalytic intermediate in the ccNiR-mediated reduction of nitrite to ammonia, whose degree of accumulation depends exclusively on the applied potential. At low potentials the species is rapidly reduced and does not accumulate, while at higher potentials it is trapped, thus preventing catalytic ammonia formation.
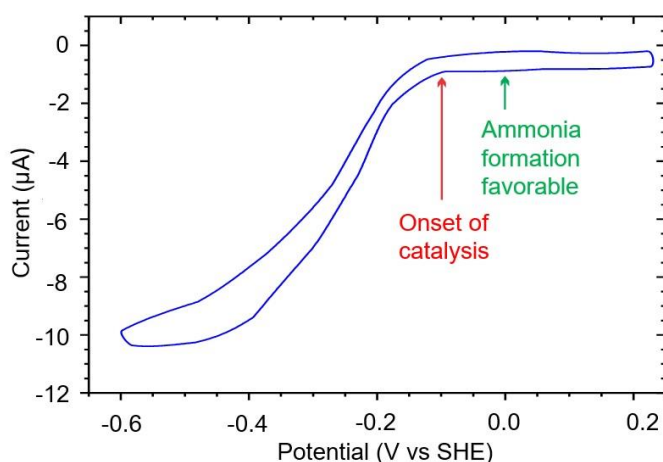
Figure 1.13. Cyclic voltammogram of electrode-adsorbed ccNiR dipped in a solution containing 500 mM nitrite in a pH 7.0 buffer.[97]

1.6.3.2. Detection of lower potential ferrous nitrosyl intermediates. As discussed more fully in ref., [60] the $\{Fe_{H1}NO\}^7$ moiety may not be the only catalytic intermediate that can be trapped by tuning the potential applied to nitrite-loaded ccNiR. Preliminary UV/Vis spectropotentiometric studies[89] showed that a second intermediate might accumulate at applied potentials between −80 mV vs SHE and the −120 mV vs SHE required for detectable catalytic turnover; this hypothesis is also supported by the results of rapid-mixing experiments with ccNiR and hydroxylamine.[59] UV/Vis stopped-flow experiments showed that when ccNiR was mixed with large excesses of

hydroxylamine (10 mM – 300 mM) the ccNiR was reduced in a triphasic exponential process. A follow-up using the rapid freeze-quench technique showed that a radical species built up within 100 ms of mixing, and then decayed, but not to zero concentration. EPR analysis[59] suggested that this transient intermediate was most likely the ferrous [Fe$_{H1}$H$_2$NO$\cdot$] moiety that theoretical studies[126] have proposed as an intermediate in ccNiR-catalyzed nitrite reduction (see Section 1.6.2.3 and Step 4 of Scheme 1.3). Together, the stopped-flow and rapid freeze-quench EPR studies suggested that, within 10 s of mixing ccNiR with hydroxylamine, electrons were transferred from the hydroxylamine to the ccNiR heme pool, generating an equilibrium mixture of partly reduced nitrosylated ccNiR moieties.[59]

1.7. Specific objectives of this thesis

Figure 1.15 summarizes schematically our understanding of the ccNiR reaction mechanism, based on the theoretical and experimental evidence reviewed in Section 1.6. We propose that the rate-limiting step for ccNiR-catalyzed reduction of nitrite to ammonia is the final 2-electron reduction of a heme 1-bound hydroxylamine equivalent (specifically, Steps 6 and 7 in Scheme 1.3). A strong reducing agent such as MV$_{red}$ can overcome this activation barrier, but weaker reducing agents will generate partially reduced nitrosylated ccNiR moieties. The hypothesis is consistent with the fact that the k_{cat} value, as measured in electrons transferred per second, is the same for nitrite and hydroxylamine reduction to ammonia when MV$_{red}$ is the electron source.[94] Chapter 2 of this thesis describes a kinetic investigation of the reaction between nitrite-loaded ccNiR and the weak reducing agent N,N,N',N'-tetramethyl-p-phenylenediamine (TMPD), which we had previously shown does not reduce nitrite-loaded ccNiR beyond the {Fe$_{H1}$NO}^{7} stage.[60] Stopped-flow analysis reveals that a 1-electron reduced intermediate accumulates transiently on the way to {Fe$_{H1}$NO}^{7}, while steady-state studies provide a measure of the lability
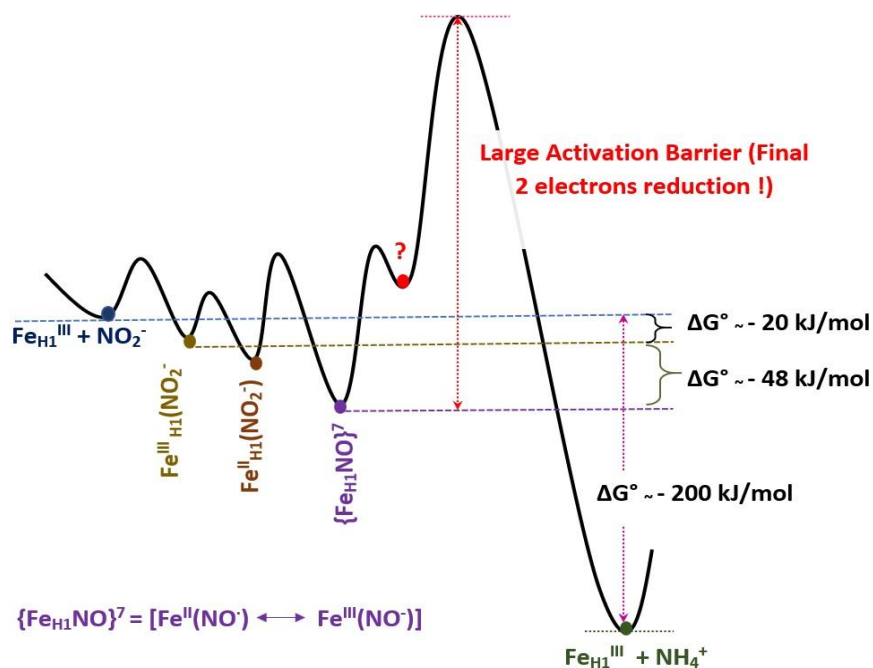
Figure 1.14. Cartoon representation of the ccNiR-catalyzed nitrite reduction path proposed on the basis of experimental and theoretical data available at the start of the project described in this thesis.

of the nitrosyl species. Chapters 3 and 4 of the thesis describe preliminary studies of ccNiR active site variants. Chapiter 3 describes the expression and purification of three such variants, H257Q, R103Q, and Y206F, while Chapter 3 presents a UV/Vis spectropotentiometric analysis of nitrite-loaded H257Q, as well as a steady-state analysis of H257Q-catalyzed reduction of nitrite and hydroxylamine by MV_{red}. Chapter 5 summarizes preliminary studies of ccNiR-catalyzed nitrite reduction by reduced indigo trisulfonate. Reduced indigo trisulfonate ($E^o = -0.085$ V) is a stronger reducing agent than TMPD, but a weaker one than M_{red}. The goal of this study was to trap one or

more nitrosylated ccNiR intermediates that are more reduced than $\{Fe_{H1}NO\}^7$. Finally, Chapter 6 summarizes the findings of the thesis.[60, 77, 86-87, 89, 91-92, 97-98, 119, 135, 141-144]

1.8. References

1.   Cole, J. A., Independent pathways for the anaerobic reduction of nitrite to ammonia by Escherichia coli. *Biochem Soc Trans* **1982,** *10* (6), 476-8.

2.   Kajie, S.; Anraku, Y., Purification of a hexaheme cytochrome c552 from Escherichia coli K 12 and its properties as a nitrite reductase. *Eur J Biochem* **1986,** *154* (2), 457-63.

3.   Liu, M. C.; Peck, H. D., Jr., The isolation of a hexaheme cytochrome from Desulfovibrio desulfuricans and its identification as a new type of nitrite reductase. *J Biol Chem* **1981,** *256* (24), 13159-64.

4.   Schumacher, W.; Kroneck, P. M. H.; Pfennig, N., Comparative systematic study on "Spirillum" 5175, Campylobacter and Wolinella species. *Archives of Microbiology* **1992,** *158* (4), 287-293.

5.   Summers, D. P.; Chang, S., Prebiotic ammonia from reduction of nitrite by iron (II) on the early Earth. *Nature* **1993,** *365*, 630-3.

6.   Fritz, G.; Einsle, O.; Rudolf, M.; Schiffer, A.; Kroneck, P. M., Key bacterial multi-centered metal enzymes involved in nitrate and sulfate respiration. *J Mol Microbiol Biotechnol* **2005,** *10* (2-4), 223-33.

7.   Richardson, D. J.; Berks, B. C.; Russell, D. A.; Spiro, S.; Taylor, C. J., Functional, biochemical and genetic diversity of prokaryotic nitrate reductases. *Cell Mol Life Sci* **2001,** *58* (2), 165-78.

8.   Zumft, W. G., Cell biology and molecular basis of denitrification. *Microbiol Mol Biol Rev* **1997,** *61* (4), 533-616.

9.   Campbell, W. H., NITRATE REDUCTASE STRUCTURE, FUNCTION AND REGULATION: Bridging the Gap between Biochemistry and Physiology. *Annu Rev Plant Physiol Plant Mol Biol* **1999,** *50*, 277-303.

10.   Shi, L.; Chen, B.; Wang, Z.; Elias, D. A.; Mayer, M. U.; Gorby, Y. A.; Ni, S.; Lower, B. H.; Kennedy, D. W.; Wunschel, D. S.; Mottaz, H. M.; Marshall, M. J.; Hill, E. A.; Beliaev, A. S.; Zachara, J. M.; Fredrickson, J. K.; Squier, T. C., Isolation of a high-affinity functional protein complex between OmcA and MtrC: Two outer membrane decaheme c-type cytochromes of *Shewanella oneidensis* MR-1. *J Bacteriol* **2006,** *188* (13), 4705-14.

11.   Simon, J., Enzymology and bioenergetics of respiratory nitrite ammonification. *FEMS Microbiol Rev* **2002,** *26* (3), 285-309.

12.   Richardson, D. J., Bacterial respiration: a flexible process for a changing environment. *Microbiology* **2000,** *146 (Pt 3)*, 551-571.

13.   Heidelberg, J. F.; Paulsen, I. T.; Nelson, K. E.; Gaidos, E. J.; Nelson, W. C.; Read, T. D.; Eisen, J. A.; Seshadri, R.; Ward, N.; Methe, B.; Clayton, R. A.; Meyer, T.; Tsapin, A.; Scott, J.; Beanan, M.; Brinkac, L.; Daugherty, S.; DeBoy, R. T.; Dodson, R. J.; Durkin, A. S.; Haft, D. H.; Kolonay, J. F.; Madupu, R.; Peterson, J. D.; Umayam, L. A.; White, O.; Wolf, A. M.; Vamathevan, J.; Weidman, J.; Impraim, M.; Lee, K.; Berry, K.; Lee, C.; Mueller, J.; Khouri, H.; Gill, J.; Utterback, T. R.; McDonald, L. A.; Feldblyum, T. V.; Smith, H. O.; Venter, J. C.; Nealson, K. H.; Fraser, C. M., Genome sequence of the dissimilatory metal ion-reducing bacterium Shewanella oneidensis. *Nat Biotechnol* **2002,** *20* (11), 1118-23.

14.   Venkateswaran, K.; Moser, D. P.; Dollhopf, M. E.; Lies, D. P.; Saffarini, D. A.; MacGregor, B. J.; Ringelberg, D. B.; White, D. C.; Nishijima, M.; Sano, H.; Burghardt, J.; Stackebrandt, E.; Nealson, K. H., Polyphasic taxonomy of the genus Shewanella and description of *Shewanella oneidensis* sp. nov. *Int J Syst Bacteriol* **1999,** *49 Pt 2*, 705-24.

15.   Chen, Y.-S.; Liu, Y.-C.; Yen, M.-Y.; Wang, J.-H.; Wang, J.-H.; Wann, S.-R.; Cheng, D.-L., Skin and Soft-Tissue Manifestations of Shewanella putrefaciens Infection. *Clinical Infectious Diseases* **1997,** *25* (2), 225-229.

16.   Derby, H.; Hammer, B. W., Bacteriology of butter. **1931**.

17.   Gralnick, J. A.; Newman, D. K., Extracellular respiration. *Mol Microbiol* **2007,** *65* (1), 1-11.

18.   MacDonell, M. T.; Colwell, R. R., Phylogeny of the Vibrionaceae, and Recommendation for Two New Genera, Listonella and Shewanella. *Systematic and Applied Microbiology* **1985,** *6* (2), 171-182.

19.   Gralnick, J. A.; Vali, H.; Lies, D. P.; Newman, D. K., Extracellular respiration of dimethyl sulfoxide by *Shewanella oneidensis* strain MR-1. *Proc Natl Acad Sci U S A* **2006,** *103* (12), 4669-74.

20.   Lovley, D. R.; Phillips, E. J., Novel mode of microbial energy metabolism: organic carbon oxidation coupled to dissimilatory reduction of iron or manganese. *Appl Environ Microbiol* **1988,** *54* (6), 1472-80.

21.   Myers, C. R.; Nealson, K. H., Bacterial manganese reduction and growth with manganese oxide as the sole electron acceptor. *Science* **1988,** *240* (4857), 1319-21.

22.   Gorby, Y. A.; Yanina, S.; McLean, J. S.; Rosso, K. M.; Moyles, D.; Dohnalkova, A.; Beveridge, T. J.; Chang, I. S.; Kim, B. H.; Kim, K. S.; Culley, D. E.; Reed, S. B.; Romine, M. F.;

Saffarini, D. A.; Hill, E. A.; Shi, L.; Elias, D. A.; Kennedy, D. W.; Pinchuk, G.; Watanabe, K.; Ishii, S.; Logan, B.; Nealson, K. H.; Fredrickson, J. K., Electrically conductive bacterial nanowires produced by *Shewanella oneidensis* strain MR-1 and other microorganisms. *Proc Natl Acad Sci U S A* **2006,** *103* (30), 11358-63.

23.   Myers, C. R.; Myers, J. M., Localization of cytochromes to the outer membrane of anaerobically grown Shewanella putrefaciens MR-1. *J Bacteriol* **1992,** *174* (11), 3429-38.

24.   Francis, C. A.; Casciotti, K. L.; Tebo, B. M., Localization of Mn (II)-oxidizing activity and the putative multicopper oxidase, MnxG, to the exosporium of the marine Bacillus sp. strain SG-1. *Archives of microbiology* **2002,** *178* (6), 450-456.

25.   Bagge, D.; Hjelm, M.; Johansen, C.; Huber, I.; Gram, L., Shewanella putrefaciens adhesion and biofilm formation on food processing surfaces. *Appl Environ Microbiol* **2001,** *67* (5), 2319-25.

26.   Little, B.; Wagner, P.; Hart, K.; Ray, R.; Lavoie, D.; Nealson, K.; Aguilar, C., The role of biomineralization in microbiologically influenced corrosion. *Biodegradation* **1998,** *9* (1), 1-10.

27.   Lower, S. K.; Hochella, M. F., Jr.; Beveridge, T. J., Bacterial recognition of mineral surfaces: nanoscale interactions between Shewanella and alpha-FeOOH. *Science* **2001,** *292* (5520), 1360-3.

28.   Methe, B. A.; Nelson, K. E.; Eisen, J. A.; Paulsen, I. T.; Nelson, W.; Heidelberg, J. F.; Wu, D.; Wu, M.; Ward, N.; Beanan, M. J.; Dodson, R. J.; Madupu, R.; Brinkac, L. M.; Daugherty, S. C.; DeBoy, R. T.; Durkin, A. S.; Gwinn, M.; Kolonay, J. F.; Sullivan, S. A.; Haft, D. H.; Selengut, J.; Davidsen, T. M.; Zafar, N.; White, O.; Tran, B.; Romero, C.; Forberger, H. A.; Weidman, J.; Khouri, H.; Feldblyum, T. V.; Utterback, T. R.; Van Aken, S. E.; Lovley, D. R.; Fraser, C. M.,

Genome of Geobacter sulfurreducens: metal reduction in subsurface environments. *Science* **2003,** *302* (5652), 1967-9.

29.   Mowat, C. G.; Chapman, S. K., Multi-heme cytochromes--new structures, new chemistry. *Dalton Trans* **2005,** (21), 3381-9.

30.   Blattner, F. R.; Plunkett, G., 3rd; Bloch, C. A.; Perna, N. T.; Burland, V.; Riley, M.; Collado-Vides, J.; Glasner, J. D.; Rode, C. K.; Mayhew, G. F.; Gregor, J.; Davis, N. W.; Kirkpatrick, H. A.; Goeden, M. A.; Rose, D. J.; Mau, B.; Shao, Y., The complete genome sequence of Escherichia coli K-12. *Science* **1997,** *277* (5331), 1453-62.

31.   Long, H.; Hammer, B., Classification of the organism important in dairy products: III. Pseudomonas putrefaciens (Research Bulletin 285, January 1941). State College of Agriculture Experiment Station and Mechanic Arts, Iowa: 1941.

32.   King, E., The identification of unusual pathogenic gram negative bacteria. US Dept. *Health, Education and Welfare, Public Health Service, National Communicable Disease Center, Atlanta, Georgia* **1967**.

33.   Holmes, B.; Lapage, S. P.; Malnick, H., Strains of Pseudomonas putrefaciens from clinical material. *J Clin Pathol* **1975,** *28* (2), 149-155.

34.   Riley, P. S.; Tatum, H. W.; Weaver, R. E., Pseudomonas putrefaciens isolates from clinical specimens. *Appl Microbiol* **1972,** *24* (5), 798-800.

35.   Richards, G. P.; Watson, M. A.; Crane, E. J., 3rd; Burt, I. G.; Bushek, D., Shewanella and Photobacterium spp. in oysters and seawater from the Delaware Bay. *Appl Environ Microbiol* **2008,** *74* (11), 3323-7.

36.   Vandepitte, J.; Debois, J., Pseudomonas putrefaciens as a cause of bacteremia in humans. *J Clin Microbiol* **1978,** *7* (1), 70-72.

37.   Owen, R. J.; Legors, R. M.; Lapage, S. P., Base composition, size and sequence similarities of genoma deoxyribonucleic acids from clinical isolates of Pseudomonas putrefaciens. *J Gen Microbiol* **1978,** *104* (1), 127-138.

38.   MacDonell, M.; Colwell, R., Phylogeny of the Vibrionaceae, and recommendation for two new genera, Listonella and Shewanella. *Systematic and applied microbiology* **1985,** *6* (2), 171-182.

39.   Dominguez, H.; Vogel, B. F.; Gram, L.; Hoffmann, S.; Schaebel, S., Shewanella alga bacteremia in two patients with lower leg ulcers. *Clinical infectious diseases* **1996,** *22* (6), 1036-1039.

40.   Thormann, K. M.; Saville, R. M.; Shukla, S.; Pelletier, D. A.; Spormann, A. M., Initial Phases of biofilm formation in *Shewanella oneidensis* MR-1. *J Bacteriol* **2004,** *186* (23), 8096-104.

41.   Takayama, Y.; Akutsu, H., Expression in periplasmic space of Shewanella oneidensis. *Protein Expr Purif* **2007,** *56* (1), 80-4.

42.   Thony-Meyer, L.; Fischer, F.; Kunzler, P.; Ritz, D.; Hennecke, H., Escherichia coli genes required for cytochrome c maturation. *J Bacteriol* **1995,** *177* (15), 4321-6.

43.   Londer, Y. Y.; Giuliani, S. E.; Peppler, T.; Collart, F. R., Addressing *Shewanella oneidensis* "cytochromome": the first step towards high-throughput expression of cytochromes c. *Protein Expr Purif* **2008,** *62* (1), 128-37.

44.   Ozawa, K.; Yasukawa, F.; Fujiwara, Y.; Akutsu, H., A simple, rapid, and highly efficient gene expression system for multiheme cytochromes c. *Biosci Biotechnol Biochem* **2001,** *65* (1), 185-9.

45.   Londer, Y. Y.; Pokkuluri, P. R.; Orshonsky, V.; Orshonsky, L.; Schiffer, M., Heterologous expression of dodecaheme "nanowire" cytochromes c from Geobacter sulfurreducens. *Protein Expr Purif* **2006,** *47* (1), 241-8.

46.   Eaves, D. J.; Grove, J.; Staudenmann, W.; James, P.; Poole, R. K.; White, S. A.; Griffiths, I.; Cole, J. A., Involvement of products of the nrfEFG genes in the covalent attachment of haem c to a novel cysteine-lysine motif in the cytochrome c552 nitrite reductase from Escherichia coli. *Mol Microbiol* **1998,** *28* (1), 205-16.

47.   Ozawa, K.; Tsapin, A. I.; Nealson, K. H.; Cusanovich, M. A.; Akutsu, H., Expression of a tetraheme protein, Desulfovibrio vulgaris Miyazaki F cytochrome c(3), in *Shewanella oneidensis* MR-1. *Appl Environ Microbiol* **2000,** *66* (9), 4168-71.

48.   Da Silva, J. F.; Williams, R. J. P., *The biological chemistry of the elements: the inorganic chemistry of life*. Oxford University Press: 2001.

49.   Kaim, W. S., B. Bioinorganic Chemistry: Inorganic Elements in the Chemistry of Life. Wiley: Chichester: 1996.

50.   Sigfridsson, E.; Olsson, M. H. M.; Ryde, U., A Comparison of the Inner-Sphere Reorganization Energies of Cytochromes, Iron−Sulfur Clusters, and Blue Copper Proteins. *The Journal of Physical Chemistry B* **2001,** *105* (23), 5546-5552.

51.   Moura, I.; Pauleta, S. R.; Moura, J. J., Enzymatic activity mastered by altering metal coordination spheres. *J Biol Inorg Chem* **2008,** *13* (8), 1185-95.

52.   Dias, J. M.; Alves, T.; Bonifacio, C.; Pereira, A. S.; Trincao, J.; Bourgeois, D.; Moura, I.; Romao, M. J., Structural basis for the mechanism of Ca(2+) activation of the di-heme cytochrome c peroxidase from Pseudomonas nautica 617. *Structure* **2004,** *12* (6), 961-73.

53.   Echalier, A.; Goodhew, C. F.; Pettigrew, G. W.; Fulop, V., Activation and catalysis of the di-heme cytochrome c peroxidase from Paracoccus pantotrophus. *Structure* **2006,** *14* (1), 107-17.

54.   Echalier, A.; Brittain, T.; Wright, J.; Boycheva, S.; Mortuza, G. B.; Fulop, V.; Watmough, N. J., Redox-linked structural changes associated with the formation of a catalytically competent form of the diheme cytochrome c peroxidase from Pseudomonas aeruginosa. *Biochemistry* **2008,** *47* (7), 1947-56.

55.   Li H In: Messerschmidt A, H. R., Poulos T, Wieghart K (eds), *Handbook of metalloproteins*. Wiley, Chichester: 2001.

56.   Rosenfeld In: Messerschmidt A, H. R., Poulos T, Wieghart K (eds) *Handbook of metalloproteins*. Wiley, Chichester: 2001.

57.   Gajhede M In: Messerschmidt A, H. R., Poulos T, Wieghart K (eds) *Handbook of metalloproteins*. Wiley, Chichester: 2001.

58.   Mate, M. J. B., J.; Fita, I.; Murshudov, G.; MelikAdamyan, W.; Loewen, P. C. , *Handbook of Metalloproteins*. Wiley: Chichester: 2001; p p 486.

59.   Youngblut, M.; Pauly, D. J.; Stein, N.; Walters, D.; Conrad, J. A.; Moran, G. R.; Bennett, B.; Pacheco, A. A., *Shewanella oneidensis* cytochrome c nitrite reductase (ccNiR) does not disproportionate hydroxylamine to ammonia and nitrite, despite a strongly favorable driving force. *Biochemistry* **2014,** *53* (13), 2136-44.

60.   Ali, M.; Stein, N.; Mao, Y.; Shahid, S.; Schmidt, M.; Bennett, B.; Pacheco, A. A., Trapping of a Putative Intermediate in the Cytochrome c Nitrite Reductase (ccNiR)-Catalyzed Reduction of Nitrite: Implications for the ccNiR Reaction Mechanism. *J Am Chem Soc* **2019,** *141* (34), 13358-13371.

61.   Maia, L. B.; Moura, J. J., How biology handles nitrite. *Chem Rev* **2014,** *114* (10), 5273-357.

62.   Nomenclature Committee of the International Union of Biochemistry (NC-IUB). Nomenclature of electron-transfer proteins. Recommendations 1989. *J Biol Chem* **1992,** *267* (1), 665-77.

63.   Mac Munn, C. A., Researches on Myohaematin and the Histohaematins. *Philosophical Transactions of the Royal Society of London* **1886,** *177*, 267–298.

64.   Keilin, D., On cytochrome, a respiratory pigment, common to animals, yeast, and higher plants. *Proc. R. Soc. Lond. B* **1925,** *98* (690), 312–339.

65.   Yamanaka, T.; Okunuki, K., Chapter 14 - CYTOCHROMES. In *Microbial Iron Metabolism*, Neilands, J. B., Ed. Academic Press: 1974; pp 349-400.

66.   Everse, J., Heme Proteins. In *Encyclopedia of Biological Chemistry (Second Edition)*, Lennarz, W. J.; Lane, M. D., Eds. Academic Press: Waltham, 2013; pp 532-538.

67.   Okunuki, T. Y. a. K., Microbial Iron Metabolism. Academic Press, New York: 1974; p 349.

68.   Puustinen, A.; Wikstrom, M., The heme groups of cytochrome o from Escherichia coli. *Proc Natl Acad Sci U S A* **1991,** *88* (14), 6122-6.

69.   Nebert, D. W.; Wikvall, K.; Miller, W. L., Human cytochromes P450 in health and disease. *Philos Trans R Soc Lond B Biol Sci* **2013,** *368* (1612), 20120431.

70.   Munro, A. W.; Girvan, H. M.; McLean, K. J., Cytochrome P450--redox partner fusion enzymes. *Biochim Biophys Acta* **2007,** *1770* (3), 345-59.

71.   Reiss, T., Drug discovery of the future: the implications of the human genome project. *Trends Biotechnol* **2001,** *19* (12), 496-9.

72.   Hopkins, A. L.; Groom, C. R., The druggable genome. *Nat Rev Drug Discov* **2002,** *1* (9), 727-30.

73.   Wallin, E.; von Heijne, G., Genome-wide analysis of integral membrane proteins from eubacterial, archaean, and eukaryotic organisms. *Protein Sci* **1998,** *7* (4), 1029-38.

74.   Stevens, T. J.; Arkin, I. T., Do more complex organisms have a greater proportion of membrane proteins in their genomes? *Proteins* **2000,** *39* (4), 417-20.

75.   Meyer, T. E.; Tsapin, A. I.; Vandenberghe, I.; de Smet, L.; Frishman, D.; Nealson, K. H.; Cusanovich, M. A.; van Beeumen, J. J., Identification of 42 possible cytochrome C genes in the *Shewanella oneidensis* genome and characterization of six soluble cytochromes. *OMICS* **2004,** *8* (1), 57-77.

76.   Romine, M. F.; Carlson, T. S.; Norbeck, A. D.; McCue, L. A.; Lipton, M. S., Identification of mobile elements and pseudogenes in the *Shewanella oneidensis* MR-1 genome. *Appl Environ Microbiol* **2008,** *74* (10), 3257-65.

77.   Einsle, O.; Messerschmidt, A.; Stach, P.; Bourenkov, G. P.; Bartunik, H. D.; Huber, R.; Kroneck, P. M., Structure of cytochrome c nitrite reductase. *Nature* **1999,** *400* (6743), 476-80.

78.   Liu, X.; Kim, C. N.; Yang, J.; Jemmerson, R.; Wang, X., Induction of apoptotic program in cell-free extracts: requirement for dATP and cytochrome c. *Cell* **1996,** *86* (1), 147-57.

79.   H. Tuppy, G. K., In *Encyclopedia of Biological Chemistry (Second Edition)*, 2013.

80.   Poock, S. R.; Leach, E. R.; Moir, J. W.; Cole, J. A.; Richardson, D. J., Respiratory detoxification of nitric oxide by the cytochrome c nitrite reductase of Escherichia coli. *J Biol Chem* **2002,** *277* (26), 23664-9.

81.   Pittman, M. S.; Elvers, K. T.; Lee, L.; Jones, M. A.; Poole, R. K.; Park, S. F.; Kelly, D. J., Growth of Campylobacter jejuni on nitrate and nitrite: electron transport to NapA and NrfA via

NrfH and distinct roles for NrfA and the globin Cgb in protection against nitrosative stress. *Mol Microbiol* **2007,** *63* (2), 575-90.

82.   Macuch, P. J.; Tanner, A. C., Campylobacter species in health, gingivitis, and periodontitis. *J Dent Res* **2000,** *79* (2), 785-92.

83.   Marcelino, S. L.; Gaetti-Jardim, E., Jr.; Nakano, V.; Canonico, L. A.; Nunes, F. D.; Lotufo, R. F.; Pustiglioni, F. E.; Romito, G. A.; Avila-Campos, M. J., Presence of periodontopathic bacteria in coronary arteries from patients with chronic periodontitis. *Anaerobe* **2010,** *16* (6), 629-32.

84.   Klotz, M. G.; Schmid, M. C.; Strous, M.; op den Camp, H. J.; Jetten, M. S.; Hooper, A. B., Evolution of an octahaem cytochrome c protein family that is key to aerobic and anaerobic ammonia oxidation by bacteria. *Environ Microbiol* **2008,** *10* (11), 3150-63.

85.   Einsle, O.; Stach, P.; Messerschmidt, A.; Simon, J.; Kroger, A.; Huber, R.; Kroneck, P. M., Cytochrome c nitrite reductase from Wolinella succinogenes. Structure at 1.6 A resolution, inhibitor binding, and heme-packing motifs. *J Biol Chem* **2000,** *275* (50), 39608-16.

86.   Bamford, V. A.; Angove, H. C.; Seward, H. E.; Thomson, A. J.; Cole, J. A.; Butt, J. N.; Hemmings, A. M.; Richardson, D. J., Structure and spectroscopy of the periplasmic cytochrome c nitrite reductase from Escherichia coli. *Biochemistry* **2002,** *41* (9), 2921-31.

87.   Almeida, M. G.; Macieira, S.; Goncalves, L. L.; Huber, R.; Cunha, C. A.; Romao, M. J.; Costa, C.; Lampreia, J.; Moura, J. J.; Moura, I., The isolation and characterization of cytochrome c nitrite reductase subunits (NrfA and NrfH) from Desulfovibrio desulfuricans ATCC 27774. Re-evaluation of the spectroscopic data and redox properties. *Eur J Biochem* **2003,** *270* (19), 3904-15.

88.   Rodrigues, M. L.; Oliveira, T. F.; Pereira, I. A.; Archer, M., X-ray structure of the membrane-bound cytochrome c quinol dehydrogenase NrfH reveals novel haem coordination. *EMBO J* **2006,** *25* (24), 5951-60.

89.   Stein, N.; Love, D.; Judd, E. T.; Elliott, S. J.; Bennett, B.; Pacheco, A. A., Correlations between the Electronic Properties of *Shewanella oneidensis* Cytochrome c Nitrite Reductase (ccNiR) and Its Structure: Effects of Heme Oxidation State and Active Site Ligation. *Biochemistry* **2015,** *54* (24), 3749-58.

90.   Pisa, R.; Stein, T.; Eichler, R.; Gross, R.; Simon, J., The nrfI gene is essential for the attachment of the active site haem group of Wolinella succinogenes cytochrome c nitrite reductase. *Mol Microbiol* **2002,** *43* (3), 763-70.

91.   Einsle, O.; Messerschmidt, A.; Huber, R.; Kroneck, P. M.; Neese, F., Mechanism of the six-electron reduction of nitrite to ammonia by cytochrome c nitrite reductase. *J Am Chem Soc* **2002,** *124* (39), 11737-45.

92.   Cunha, C. A.; Macieira, S.; Dias, J. M.; Almeida, G.; Goncalves, L. L.; Costa, C.; Lampreia, J.; Huber, R.; Moura, J. J.; Moura, I.; Romao, M. J., Cytochrome c nitrite reductase from Desulfovibrio desulfuricans ATCC 27774. The relevance of the two calcium sites in the structure of the catalytic subunit (NrfA). *J Biol Chem* **2003,** *278* (19), 17455-65.

93.   Campecino, J.; Lagishetty, S.; Wawrzak, Z.; Sosa Alfaro, V.; Lehnert, N.; Reguera, G.; Hu, J.; Hegg, E. L., Cytochrome c nitrite reductase from the bacterium Geobacter lovleyi represents a new NrfA subclass. *J Biol Chem* **2020**.

94.   Youngblut, M.; Judd, E. T.; Srajer, V.; Sayyed, B.; Goelzer, T.; Elliott, S. J.; Schmidt, M.; Pacheco, A. A., Laue crystal structure of *Shewanella oneidensis* cytochrome c nitrite reductase from a high-yield expression system. *J Biol Inorg Chem* **2012,** *17* (4), 647-62.

95.   Page, C. C.; Moser, C. C.; Chen, X.; Dutton, P. L., Natural engineering principles of electron tunnelling in biological oxidation-reduction. *Nature* **1999,** *402* (6757), 47-52.

96.   Stach, P.; Einsle, O.; Schumacher, W.; Kurun, E.; Kroneck, P. M., Bacterial cytochrome c nitrite reductase: new structural and functional aspects. *J Inorg Biochem* **2000,** *79* (1-4), 381-5.

97.   Judd, E. T.; Youngblut, M.; Pacheco, A. A.; Elliott, S. J., Direct electrochemistry of *Shewanella oneidensis* cytochrome c nitrite reductase: evidence of interactions across the dimeric interface. *Biochemistry* **2012,** *51* (51), 10175-85.

98.   Ali, M. Probing the early steps in the catalytic reduction of nitrite to ammonia, catalyzed by cytochrome c nitrite reductase. University of Wisconsin-Milwaukee, Milwaukee, WI, 2019.

99.   Polyakov, K. M.; Boyko, K. M.; Tikhonova, T. V.; Slutsky, A.; Antipov, A. N.; Zvyagilskaya, R. A.; Popov, A. N.; Bourenkov, G. P.; Lamzin, V. S.; Popov, V. O., High-resolution structural analysis of a novel octaheme cytochrome c nitrite reductase from the haloalkaliphilic bacterium Thioalkalivibrio nitratireducens. *J Mol Biol* **2009,** *389* (5), 846-62.

100.   Tikhonova, T. V.; Slutsky, A.; Antipov, A. N.; Boyko, K. M.; Polyakov, K. M.; Sorokin, D. Y.; Zvyagilskaya, R. A.; Popov, V. O., Molecular and catalytic properties of a novel cytochrome c nitrite reductase from nitrate-reducing haloalkaliphilic sulfur-oxidizing bacterium Thioalkalivibrio nitratireducens. *Biochim Biophys Acta* **2006,** *1764* (4), 715-23.

101.   Tikhonova, T. V.; Slutskaya, E. S.; Filimonenkov, A. A.; Boyko, K. M.; Kleimenov, S. Y.; Konarev, P. V.; Polyakov, K. M.; Svergun, D. I.; Trofimov, A. A.; Khomenkov, V. G.; Zvyagilskaya, R. A.; Popov, V. O., Isolation and oligomeric composition of cytochrome c nitrite reductase from the haloalkaliphilic bacterium Thioalkalivibrio nitratireducens. *Biochemistry (Mosc)* **2008,** *73* (2), 164-70.

102. Tikhonova, T.; Tikhonov, A.; Trofimov, A.; Polyakov, K.; Boyko, K.; Cherkashin, E.; Rakitina, T.; Sorokin, D.; Popov, V., Comparative structural and functional analysis of two octaheme nitrite reductases from closely related Thioalkalivibrio species. *FEBS J* **2012,** *279* (21), 4052-61.

103. Kern, M.; Volz, J.; Simon, J., The oxidative and nitrosative stress defence network of Wolinella succinogenes: cytochrome c nitrite reductase mediates the stress response to nitrite, nitric oxide, hydroxylamine and hydrogen peroxide. *Environ Microbiol* **2011,** *13* (9), 2478-94.

104. Simon, J.; Gross, R.; Einsle, O.; Kroneck, P. M.; Kroger, A.; Klimmek, O., A NapC/NirT-type cytochrome c (NrfH) is the mediator between the quinone pool and the cytochrome c nitrite reductase of Wolinella succinogenes. *Mol Microbiol* **2000,** *35* (3), 686-96.

105. Pereira, I. C.; Abreu, I. A.; Xavier, A. V.; LeGall, J.; Teixeira, M., Nitrite reductase from Desulfovibrio desulfuricans (ATCC 27774)--a heterooligomer heme protein with sulfite reductase activity. *Biochem Biophys Res Commun* **1996,** *224* (3), 611-8.

106. Clarke, T. A.; Hemmings, A. M.; Burlat, B.; Butt, J. N.; Cole, J. A.; Richardson, D. J., Comparison of the structural and kinetic properties of the cytochrome c nitrite reductases from Escherichia coli, Wolinella succinogenes, Sulfurospirillum deleyianum and Desulfovibrio desulfuricans. *Biochem Soc Trans* **2006,** *34* (Pt 1), 143-5.

107. Lukat, P.; Rudolf, M.; Stach, P.; Messerschmidt, A.; Kroneck, P. M.; Simon, J.; Einsle, O., Binding and reduction of sulfite by cytochrome c nitrite reductase. *Biochemistry* **2008,** *47* (7), 2080-6.

108. Kemp, G. L.; Clarke, T. A.; Marritt, S. J.; Lockwood, C.; Poock, S. R.; Hemmings, A. M.; Richardson, D. J.; Cheesman, M. R.; Butt, J. N., Kinetic and thermodynamic resolution of the

interactions between sulfite and the pentahaem cytochrome NrfA from Escherichia coli. *Biochem J* **2010,** *431* (1), 73-80.

109.   Burlat, B.; Gwyer, J. D.; Poock, S.; Clarke, T.; Cole, J. A.; Hemmings, A. M.; Cheesman, M. R.; Butt, J. N.; Richardson, D. J., Cytochrome c nitrite reductase: from structural to physicochemical analysis. *Biochem Soc Trans* **2005,** *33* (Pt 1), 137-40.

110.   Simon, J.; Kern, M., Quinone-reactive proteins devoid of haem b form widespread membrane-bound electron transport modules in bacterial respiration. *Biochem Soc Trans* **2008,** *36* (Pt 5), 1011-6.

111.   Berks, B. C.; Ferguson, S. J.; Moir, J. W.; Richardson, D. J., Enzymes and associated electron transport systems that catalyse the respiratory reduction of nitrogen oxides and oxyanions. *Biochim Biophys Acta* **1995,** *1232* (3), 97-173.

112.   Lockwood, C.; Butt, J. N.; Clarke, T. A.; Richardson, D. J., Molecular interactions between multihaem cytochromes: probing the protein-protein interactions between pentahaem cytochromes of a nitrite reductase complex. *Biochem Soc Trans* **2011,** *39* (1), 263-8.

113.   Clarke, T. A.; Cole, J. A.; Richardson, D. J.; Hemmings, A. M., The crystal structure of the pentahaem c-type cytochrome NrfB and characterization of its solution-state interaction with the pentahaem nitrite reductase NrfA. *Biochem J* **2007,** *406* (1), 19-30.

114.   Todorovic, S.; Rodrigues, M. L.; Matos, D.; Pereira, I. A., Redox properties of lysine- and methionine-coordinated hemes ensure downhill electron transfer in NrfH2A4 nitrite reductase. *J Phys Chem B* **2012,** *116* (19), 5637-43.

115.   Hartshorne, R. S.; Reardon, C. L.; Ross, D.; Nuester, J.; Clarke, T. A.; Gates, A. J.; Mills, P. C.; Fredrickson, J. K.; Zachara, J. M.; Shi, L.; Beliaev, A. S.; Marshall, M. J.; Tien, M.; Brantley,

S.; Butt, J. N.; Richardson, D. J., Characterization of an electron conduit between bacteria and the extracellular environment. *Proc Natl Acad Sci U S A* **2009,** *106* (52), 22169-74.

116.   Leys, D.; Tsapin, A. S.; Nealson, K. H.; Meyer, T. E.; Cusanovich, M. A.; Van Beeumen, J. J., Structure and mechanism of the flavocytochrome c fumarate reductase of Shewanella putrefaciens MR-1. *Nat Struct Biol* **1999,** *6* (12), 1113-7.

117.   Schuetz, B.; Schicklberger, M.; Kuermann, J.; Spormann, A. M.; Gescher, J., Periplasmic electron transfer via the c-type cytochromes MtrA and FccA of *Shewanella oneidensis* MR-1. *Appl Environ Microbiol* **2009,** *75* (24), 7789-96.

118.   Pessanha, M.; Rothery, E. L.; Miles, C. S.; Reid, G. A.; Chapman, S. K.; Louro, R. O.; Turner, D. L.; Salgueiro, C. A.; Xavier, A. V., Tuning of functional heme reduction potentials in Shewanella fumarate reductases. *Biochim Biophys Acta* **2009,** *1787* (2), 113-20.

119.   Judd, E. T.; Stein, N.; Pacheco, A. A.; Elliott, S. J., Hydrogen bonding networks tune proton-coupled redox steps during the enzymatic six-electron conversion of nitrite to ammonia. *Biochemistry* **2014,** *53* (35), 5638-46.

120.   Costa, C.; Moura, J. J. G.; Moura, I.; Liu, M. Y.; Peck, H. D.; Legall, J.; Wang, Y. N.; Huynh, B. H., Hexaheme Nitrite Reductase from Desulfovibrio-Desulfuricans - Mossbauer and Epr Characterization of the Heme Groups. *Journal of Biological Chemistry* **1990,** *265* (24), 14382-14388.

121.   Schumacher, W.; Hole, U.; Kroneck, P. M., Ammonia-forming cytochrome c nitrite reductase from Sulfurospirillum deleyianum is a tetraheme protein: new aspects of the molecular composition and spectroscopic properties. *Biochem Biophys Res Commun* **1994,** *205* (1), 911-6.

122. Costa, C.; Moura, J. J. G.; Moura, I.; Wang, Y. N.; Huynh, B. H., Redox properties of cytochrome c nitrite reductase from Desulfovibrio desulfuricans ATCC 27774. *Journal of Biological Chemistry* **1996,** *271* (38), 23191-23196.

123. Bykov, D.; Neese, F., Substrate binding and activation in the active site of cytochrome c nitrite reductase: a density functional study. *J Biol Inorg Chem* **2011,** *16* (3), 417-30.

124. Bykov, D.; Neese, F., Reductive activation of the heme iron-nitrosyl intermediate in the reaction mechanism of cytochrome c nitrite reductase: a theoretical study. *J Biol Inorg Chem* **2012,** *17* (5), 741-60.

125. Bykov, D.; Neese, F., Six-electron reduction of nitrite to ammonia by cytochrome c nitrite reductase: insights from density functional theory studies. *Inorg Chem* **2015,** *54* (19), 9303-16.

126. Bykov, D.; Plog, M.; Neese, F., Heme-bound nitroxyl, hydroxylamine, and ammonia ligands as intermediates in the reaction cycle of cytochrome c nitrite reductase: a theoretical study. *J Biol Inorg Chem* **2014,** *19* (1), 97-112.

127. Martins, G.; Rodrigues, L.; Cunha, F. M.; Matos, D.; Hildebrandt, P.; Murgida, D. H.; Pereira, I. A.; Todorovic, S., Substrate binding to a nitrite reductase induces a spin transition. *J Phys Chem B* **2010,** *114* (16), 5563-6.

128. Lockwood, C. W.; Burlat, B.; Cheesman, M. R.; Kern, M.; Simon, J.; Clarke, T. A.; Richardson, D. J.; Butt, J. N., Resolution of key roles for the distal pocket histidine in cytochrome C nitrite reductases. *J Am Chem Soc* **2015,** *137* (8), 3059-68.

129. Copeland, D. M.; Soares, A. S.; West, A. H.; Richter-Addo, G. B., Crystal structures of the nitrite and nitric oxide complexes of horse heart myoglobin. *J Inorg Biochem* **2006,** *100* (8), 1413-25.

130.   Yi, J.; Safo, M. K.; Richter-Addo, G. B., The nitrite anion binds to human hemoglobin via the uncommon O-nitrito mode. *Biochemistry* **2008,** *47* (32), 8247-9.

131.   Nasri, H.; Ellison, M. K.; Shang, M.; Schulz, C. E.; Scheidt, W. R., Variable pi-bonding in iron(II) porphyrinates with nitrite, CO, and tert-butyl isocyanide: characterization of [Fe(TpivPP)(NO2)(CO)]. *Inorg Chem* **2004,** *43* (9), 2932-42.

132.   Nasri, H.; Ellison, M. K.; Krebs, C.; Huynh, B. H.; Scheidt, W. R., Highly Variable π-Bonding in the Interaction of Iron(II) Porphyrinates with Nitrite. *Journal of the American Chemical Society* **2000,** *122* (44), 10795-10804.

133.   Hartshorne, S.; Richardson, D. J.; Simon, J., Multiple haem lyase genes indicate substrate specificity in cytochrome c biogenesis. *Biochem Soc Trans* **2006,** *34* (Pt 1), 146-9.

134.   Almeida, M. G.; Silveira, C. M.; Guigliarelli, B.; Bertrand, P.; Moura, J. J.; Moura, I.; Leger, C., A needle in a haystack: the active site of the membrane-bound complex cytochrome c nitrite reductase. *FEBS Lett* **2007,** *581* (2), 284-8.

135.   Enemark, J. H.; Feltham, R. D., Principles of structure, bonding, and reactivity for metal nitrosyl complexes. *Coordination Chemistry Reviews* **1974,** *13* (4), 339-406.

136.   Clarke, T. A.; Kemp, G. L.; Van Wonderen, J. H.; Doyle, R. M.; Cole, J. A.; Tovell, N.; Cheesman, M. R.; Butt, J. N.; Richardson, D. J.; Hemmings, A. M., Role of a conserved glutamine residue in tuning the catalytic activity of Escherichia coli cytochrome c nitrite reductase. *Biochemistry* **2008,** *47* (12), 3789-99.

137.   George, S. J.; Kvaratskhelia, M.; Dilworth, M. J.; Thorneley, R. N., Reversible alkaline inactivation of lignin peroxidase involves the release of both the distal and proximal site calcium ions and bishistidine co-ordination of the haem. *Biochem J* **1999,** *344 Pt 1*, 237-44.

138.   Mowat, C. G.; Rothery, E.; Miles, C. S.; McIver, L.; Doherty, M. K.; Drewette, K.; Taylor, P.; Walkinshaw, M. D.; Chapman, S. K.; Reid, G. A., Octaheme tetrathionate reductase is a respiratory enzyme with novel heme ligation. *Nat Struct Mol Biol* **2004,** *11* (10), 1023-4.

139.   Lockwood, C. W.; Clarke, T. A.; Butt, J. N.; Hemmings, A. M.; Richardson, D. J., Characterization of the active site and calcium binding in cytochrome c nitrite reductases. *Biochem Soc Trans* **2011,** *39* (6), 1871-5.

140.   Pereira, I. A.; LeGall, J.; Xavier, A. V.; Teixeira, M., Characterization of a heme c nitrite reductase from a non-ammonifying microorganism, Desulfovibrio vulgaris Hildenborough. *Biochim Biophys Acta* **2000,** *1481* (1), 119-30.

141.   Watanabe, T. H., K.,, Measurement of the extinction coefficient of the methyl viologen cation radical and the efficiency of its formation by semiconductor photocatalysis. *J. Phys. Chem.* **1982,** *86,* , 2617-2619.

142.   Michaelis, L.; Schubert, M. P.; Granick, S., The Free Radicals of the Type of Wurster's Salts. *Journal of the American Chemical Society* **1939,** *61* (8), 1981-1992.

143.   Chaka, G.; Bakac, A., Two-electron oxidation of N,N,N',N'-tetramethylphenylenediamine with a chromium(v) salen complex. *Dalton Trans* **2009,** (2), 318-21.

144.   Nematollahi, D.; Hosseinzadeh, S.; Dadpou, B., Comproportionation and Michael addition reactions of electrochemically generated N,N,N ',N '-tetramethyl-1,4-phenylenediamine dication. Synthesis of new unsymmetrical aryl sulfones containing N,N,N ',N '-tetramethyl-1,4-phenylenediamine moiety. *J Electroanal Chem* **2015,** *759*, 144-152.

Chapter 2

Investigation and characterization of the trapped intermediates at the early stage of nitrite loaded wtccNiR reduction

2.1. Overview

In earlier studies within the Pacheco group, *S. oneidensis* ccNiR was found to catalyze slow reduction of nitrite to nitric oxide when a weak reductant such as ferrocyanide, *N,N,N',N'*-tetramethyl-*p*-phenylenediamine (TMPD) or $[Ru(NH_3)_6]^{2+}$ was the electron source.[1-2] NO˙ production was verified by capturing the product with catalase to make the spectroscopically distinct nitrosylated product.[1] When ferrocyanide was used as the electron donor the initial rate of NO˙ generation was found to depend linearly on ccNiR concentration, sigmoidally on pH, and hyperbolically on nitrite and ferrocyanide concentrations.[1]

The NO˙ trapping experiments described above were performed using ccNiR concentrations of 0 – 100 nM. In the presence of micromolar concentrations of ccNiR catalytic reduction of nitrite by ferrocyanide was fast enough that detectable amounts of the colored ferricyanide product accumulated over the course of an hour, thus obviating the need for the catalase indicator. In these experiments one could also follow by UV/Vis a biphasic reduction of nitrite-loaded ccNiR.[1] The faster ccNiR reduction phase took place within the reagent mixing time, and it's amplitude decreased if 10 – 100 μM of ferricyanide were added to the reaction mixture at the start. The slower phase had a typical half-life of ~100 s at ferrocyanide concentrations > 1 mM; the half-life increased as the initial ferrocyanide concentration decreased below ~1 mM, but it was difficult to analyze the low-ferrocyanide concentration experiments quantitatively. The extent of

heme reduction over both phases was invariant with respect to initial ferricyanide concentration. Importantly, the rate of ferricyanide formation associated with release of free NO· was linear over the entire monitoring interval and was not affected by the extent of ccNiR reduction.

The experiments with ferrocyanide and micromolar concentrations of ccNiR provided many intriguing mechanistic insights. However, they were difficult to analyze quantitatively for two primary reasons. First, the ferricyanide product has very weak absorbance, so monitoring micromolar changes in ferricyanide concentration pushes the limit of UV/Vis detection. This is exacerbated by the second difficulty, which is that the first-order reduction of ccNiR by ferrocyanide occurs over hundreds of seconds, and thus overlaps the appearance of ferricyanide that is coupled to NO· release. Together, these two factors severely limited the range of conditions under which ccNiR-catalyzed reduction of nitrite by ferrocyanide could be meaningfully investigated.

This chapter describes a systematic kinetic analysis of the ccNiR-catalyzed reduction of nitrite to NO· by TMPD, using steady-state UV/Vis and stopped-flow spectroscopy. The study builds on the results obtained using ferrocyanide as electron donor but exploits two big advantages offered by TMPD. First, the product of TMPD 1-electron oxidation ($TMPD^+$, Scheme 3.1) has an intense blue color that is much more readily detectable by UV/Vis spectroscopy than ferricyanide. Second, TMPD reduces nitrite loaded ccNiR substantially more rapidly than the weaker reducing agent ferrocyanide; while complete reduction of the ccNiR by ferrocyanide takes several hundred seconds, reduction by TMPD is complete within less than a minute. This allowed spectral components arising from ccNiR reduction to be cleanly separated from the component that arises as $TMPD_{ox}$ is slowly generated during ccNiR-catalyzed reduction of nitrite to free NO·. CcNiR

reduction could be monitored by stopped-flow, while TMPD oxidation by nitrite was readily monitored by conventional UV/Vis spectroscopy.

2.2. Materials and Methods

2.2.1. General instrumentation

Routine UV/Vis spectroscopy was performed using a CARY Bio 50 UV/Vis spectrophotometer. Two of these spectrophotometers are already placed inside nitrogen-filled gloveboxes (MBraun and Innovative Technologies) which provide an anaerobic environment. The oxygen level was strictly monitored and maintained at less than 2 ppm; the glovebox catalysts were regenerated with 5% or 7% Hydrogen (Airgas) once a month or whenever the oxygen level rose above 2 ppm.

2.2.2. General Materials

All reagents were of high bio-grade purity and purchased from Thermo-Fisher, Dot Scientific, or MP Biomedicals unless mentioned specifically.

2.2.3. Large Scale *Shewanella oneidensis* TSP-C cells culture for wild type ccNiR protein

2.2.3.1. Culture preparation and harvesting. Wild type ccNiR (wtccNiR) was obtained from an *S. oneidensis* TSP-C expression system first reported by Youngblut et al.[3] A petri dish containing autoclaved LB agarose, and the antibiotics kanamycin (Kan, 50 μg/mL), and rifampicin (Rif, 30 μg/mL) was inoculated with *S. oneidensis* TSP-C cells containing the plasmid with the wtccNiR gene and incubated overnight at 30 °C. A single bacterial colony from the petri dish was suspended in 5mL LB (20 mg/mL), Kan (50 μg/mL), Rif (30 μg/mL) solution and was incubated for 10-11 hours in an incubator shaker at 200 rpm and 30 °C. After that period, 1 mL of bacterial

culture was transferred into 1 L of the same medium, which was then incubated for 16 hours under the same conditions as in the first step. In a final step, 1 L of bacterial cell culture was transferred into a 50 L carboy that already contained 45 L LB, Kan (50 μg/mL), Rif (30 μg/mL) thermostatted at 30 °C in a constant temperature water bath (Fig. 2.1). The culture was incubated for 16 - 18 hours at 30 °C while being continually sparged with compressed air, which served to agitate the culture suspension and to keep it aerated until late in the growth process when high bacterial density consumed oxygen faster than it could be replenished. The cells were harvested from the 45 L cell culture by centrifuging aliquots in 1 L bottles for 10 minutes at 5,800 × g. The pooled cell pellets were resuspended using 50 mM HEPES, pH=7.0 (final volume ~500 mL), and the two protease inhibitors leupeptin (1-10 μM), AEBSF/PMSF (0.1 - 1.0 mM) were immediately added. The resuspended pooled cell pellet was frozen and stored at −80 °C in a stainless-steel beaker until needed.
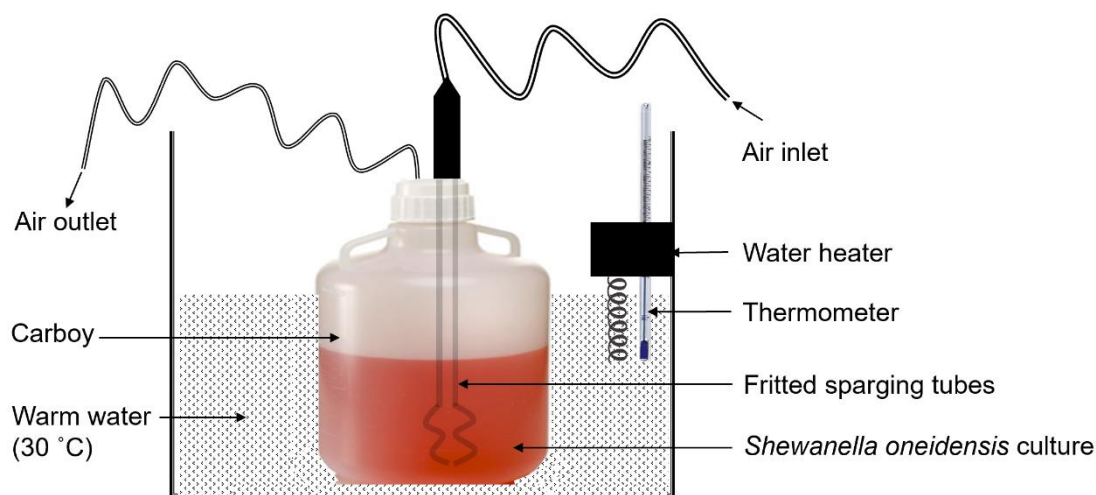
Figure 2.1. Large scale (45 L) *Shewanella oneidensis* culture for high amount wtccNiR enzyme purification. A carboy used for this culture was surrounded by water. A thermostat maintains the constant optimum temperature (30 ˚C). To keep the culture aerated and to avoid cell settling, two fritted sparging tubes inside of the carboy provided compressed air circulation that continuously agitated the culture.

2.2.3.2. Wild type ccNiR enzyme purification from overexpressing *S. oneidensis* TSP-C cells. Concentrated suspensions of cells containing the overexpressed wtccNiR were lysed by sonication in an ice-cooled stainless steel beaker, using cycles of 30 s ultrasonic bursts at 70% amplitude followed by 45 s pauses, repeated for 10 minutes. The lysed cell products were centrifuged for 30 minutes at $41,500 \times g$ and the supernatant solution was collected to remove cell debris. Finely ground ammonium sulfate (AS) was added very slowly to make the final 50 % saturated solution at 4 °C. The AS was very slowly introduced to reduce unwanted ccNiR precipitation and stirred simultaneously with a magnetic stirrer. The final mixed salt sample was centrifuged at $41,500 \times g$ for 30 min, and then the supernatant was collected.

In total, three columns were used sequentially to purify wtccNiR protein. First, the collected supernatant protein sample was loaded to a 400 mL octyl-sepharose column (hydrophobic interaction chromatography, HIC, by GE Healthcare). This column was pre-equilibrated with a buffer that contained 3 M AS, 20 mM HEPES and 1 mM EDTA, adjusted to pH = 7.0 (Buffer A). The HIC column was deemed to be equilibrated when the UV reading at 280 nm of the column flow-through was constant. After the clarified cell extract had been loaded, the column was washed with at least 2 column volumes of Buffer A until the UV reading at 280 nm of the column flow-through was once again constant. The loaded protein sample was then washed with at least 2 column volumes of a mixture containing 60% Buffer A and 40% of a pH 7.0 low salt buffer containing 20 mM HEPES and 1 mM EDTA, pH = 7 (Buffer B) until the UV at 280 nm once again dropped to a stable baseline. The eluant contained mostly non ccNiR protein and nucleic acids and was discarded. In a third step, the column was washed with a solution containing 20% Buffer A and 80 % Buffer B. All fractions from this step for which the A280 deviated significantly from the baseline were pooled and transferred to Snake-Skin dialysis tubes (9 mL /1

cm, ThermoFisher) for dialysis at 4 °C for roughly 4 hours in Buffer B. The dialysis tube was then transferred into another buffer reservoir (20 mM NaHEPES, 1 mM EDTA pH = 7.0; Buffer C) which was an optimum buffer for the second column, an 80 mL Q-sepharose anion exchange column (GE Healthcare).

The dialyzed sample was centrifuged at $41{,}500 \times g$ for 10 min. The supernatant solution was collected leaving any precipitate that accumulated during overnight dialysis. The supernatant was loaded onto the Q-sepharose column that had been pre-equilibrated with Buffer C, and the unretained flow-through was collected. The Q column retains only negatively charged proteins, and ccNiR ccNiR is nearly neutral at pH = 7.0. **Important:** it is *critical* to employ buffer made with the HEPES sodium salt rather than the HEPES acid. HEPES buffer made with 20 mM HEPES acid has an ionic strength of 10 mM and at this ionic strength ccNiR binds weakly to Q-Sepharose, which greatly decreases the resolution. HEPES buffer made with 20 mM HEPES sodium salt has an ionic strength of 20 mM and passes through the column cleanly without binding.

The eluant buffer from the Q-Sepharose column was exchanged for one containing 2 M AS, 20 mM HEPES, 1 mM EDTA, pH = 7.0 (Buffer D) using a tangential flow filtration device (TFF,30 K, OAPMP220, Pall Life Sciences) that simultaneously concentrated the sample. If necessary, the conductivity of the concentrated protein sample was adjusted to exactly that of Buffer D by adding ground solid AS. The concentrated protein sample was loaded onto a 3.5 mL RESOURCE isopropyl HIC column (GE Healthcare, capacity 25 mg protein/mL) that had been pre-equilibrated with Buffer D, and then eluted with a 0 to 40 % gradient of Buffer B. Pure ccNiR eluted at 20 – 30 % Buffer B, and was detectable as a sharp peak in the UV(280 nm) chromatogram. The purity of ccNiR was initially checked by UV/Vis spectrophotometry (pure ccNiR has an A_{409}/A_{280} absorbance ratio ≥ 4) and confirmed by observing a single band at ≈ 55 kDa in SDS-

PAGE. After exchanging the enzyme buffer for one with 50 mM HEPES, pH 7.0, and concentrating the solution to about 2-3 mL using the TFF device, the sample was stored at −80 °C until needed.

2.2.4. Pyridine hemochromagen assay for determining the concentration of wtccNiR

The pyridine hemochromagen assay was performed to determine the concentration and the extinction coefficient spectrum of wtccNiR. The method used was similar to that described by Berry and Trumpower,[4] and Barr and Guo,[5] but with the following minor modifications. Briefly, Solution-I containing 10 μL 0.1 M potassium ferricyanide was mixed with 800 μL of 0.5 M NaOH, 800 μL of pyridine (Anhydrous, 99.8% pure, Sigma-Aldrich) and 390 μL nano-pure water make 2 mL of Solution-II. The final concentrations in solution II were 500 μM $K_3[Fe(CN)_6]$, 0.2 M NaOH and 40% v/v pyridine. A solution containing equal volumes of Solution-II and 50 mM HEPES buffer, pH 7, was used to set the baseline for the UV/Vis spectrophotometer. CcNiR samples were dissolved in a 50 mM HEPES buffer, pH = 7.0, to make Solution-III. Equal volumes of Solution-II and Solution-III were mixed in a cuvette, and the UV/Vis spectrum was recorded in the range 450 nm – 800 nm. This was the oxidized pyridine hemochrome sample and was labeled as Dataset-1. A few grains of solid sodium dithionite (sodium hydrosulfite) were added into the cuvette, the solution was carefully mixed, and then several UV/Vis spectra were recorded at 30 s intervals until the spectra remained unchanged. The final spectrum was the reduced pyridine hemochrome sample and was labeled as Dataset-2; the reduced solution is distinctly pink, compared to the orange oxidized pyridine hemochrome. The difference spectrum (Dataset-2) – (Dataset-1) was fit in the range from 525 nm – 620 nm using the known extinction coefficient difference spectrum[4] to determine the concentration of pyridine hemochrome in solution. This concentration was divided by 5 to obtain the ccNiR protomer concentration in the pyridine

hemochrome solutions (as each ccNiR protomer contains 5 hemes), and then multiplied by 2 to obtain the ccNiR protomer concentration in Solution-III. To obtain the extinction coefficient spectrum of ccNiR, the spectrophotometer baseline was first reset in the range from 250 nm – 800 nm with a 50 mM HEPES buffer, pH 7. A known volume of Solution-III was diluted to 1 mL such that the Soret band absorbance (409 nm) was $\leq$ 1.0, and the UV/Vis spectrum was recorded from 250 nm – 800 nm. As the ccNiR concentration was known from the pyridine hemochrome assay, the extinction coefficient spectrum was readily obtained by dividing the absorbances obtained between 250 nm and 800 nm by the concentration and pathlength (Beer's law). A complementary extinction coefficient spectrum for the lower intensity region from 500 nm – 800 nm was also obtained from less diluted samples of Solution-III.

2.2.5. Rapid freeze pump thaw method to degas ccNiR

This procedure was performed to remove oxygen dissolved in the enzyme solution prior to transfer into the glovebox. A concentrated ccNiR solution (typically ~100 μL) was introduced into a Schlenk flask.[6] The flask was capped and its sidearm connected to a vacuum line via a vacuum hose; Apiezon M Economical High-Vacuum Lubricant was used to grease the Schlenk flask cap and sidearm stopcock. The sample was frozen with liquid nitrogen (step-1), then the stopcock was opened to evacuate the headspace gas above the frozen enzyme sample for a few minutes (step-2). The stopcock was again closed and the enzyme sample was thawed under vacuum by warming with a room temperature water bath to the release dissolved gaseous species (step-3). This freeze-pump-thaw cycle (steps 1-3) was repeated three times to remove the dissolved oxygen gas in the protein solution. The Schlenk flask containing the degassed enzyme solution could then be passed through the glovebox antechamber. *Note:* it is not generally advisable to use the freeze-pump-thaw method on protein solutions because the foam that forms during the thaw step usually denatures

proteins. However, ccNiR survived the process with no apparent changes to its chemical and physical properties.

2.2.6. Reduction of nitrite-loaded *S. oneidensis* ccNiR by *N, N, N′, N′*-tetramethyl-*p*-phenylenediamine (TMPD): UV/Vis steady steady-state experiments

TMPD was used as a weak reducing agent (+0.260 V vs SHE).[7] All the required solid reagents (TMPD, nitrite, ferricyanide) were weighed out and then transferred to a glovebox, where they were dissolved in 50 mM HEPES pH = 7.0 buffer to make stock solutions. The ferricyanide solutions were found to slowly dissociate cyanide, which binds strongly to the ccNiR active site,[8] and so were made fresh for each experiment. TMPD and nitrite stock solutions were stable indefinitely in the glovebox. Steady-state experiments were performed as described below to assess the kinetic dependence of the ccNiR-catalyzed reduction of nitrite by TMPD on TMPD, $TMPD^+$, nitrite and *S. oneidensis* ccNiR concentrations. Attempts to repeat the pH 7 experiments at pH 8 failed because the $TMPD^+$ product (Scheme 2.1) was found to be unstable at the higher pH on the timescale monitored in the steady-state experiments.

All steady-state experiments were performed in the presence of 10 μM $TMPD^+$, except those in which $TMPD^+$ concentration was the variable parameter. To determine the effect of the 1- electron oxidized TMPD free radical ($TMPD^+$, Scheme 2.1) on the kinetics of ccNiR-catalyzed reduction of nitrite by TMPD, small quantities of ferricyanide (5 μM – 50 μM) were added to large excesses of TMPD (400 μM – 3 mM). In a typical experiment to follow the kinetics in the presence of 600 μM TMPD, 5 μM $TMPD^+$, 1 μM wtccNiR and 1 mM nitrite, 1 mL of reaction mixture was made by mixing 575 μL 50 mM HEPES, pH = 7, 10 μL 100 mM nitrite, 300 μL 2 mM TMPD, 100 μL 50 μM ferricyanide, and 15 μL 66.7 μM wtccNiR in a cuvette, pre-installed in the spectrophotometer cuvette holder. The reagents were rapidly mixed using a cuvette mixer

(Fireflysci P68 mixer for semi-micro cuvettes), and data collection was immediately initiated. Spectra were collected every 15 s for 1 h in the range 300 nm - 800 nm (240 scans total). Data were collected in csv format and later analyzed by using programs written for Mathcad 15.0 (PTC Software) and Origin 9.0 (Microcal Software).[9-10] Note that in the example given ferricyanide was added to the cuvette as a fairly high volume, low concentration aliquot. This is an important detail because when smaller volumes of highly concentrated ferricyanide were added they could rapidly generate local pockets of the 2-electron oxidized $TMPD^{2+}$ species before the reaction mixtures could be stirred. $TMPD^{2+}$ is unstable,[11-12] and solutions prepared by addition of concentrated ferricyanide aliquots gave poorly reproducible results.
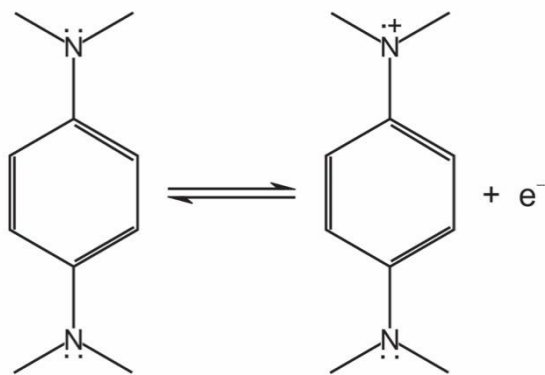
Scheme 2.1. *N,N,N´,N´*-tetramethyl-*p*-phenylenediamine (TMPD) and its 1-electron oxidized radical TMPD⁺.

2.2.7. Reduction of nitrite-loaded *S. oneidensis* **ccNiR by** *N, N, N′, N′***-tetramethyl-***p***-phenylenediamine (TMPD): stopped-flow experiments**

2.2.7.1. Stopped-Flow Experiments at varying TMPD concentrations. A single mixing SX-20 stopped-flow spectrophotometer (Applied Photophysics) was used to monitor the pre-steady-state kinetics of nitrite-loaded wtccNiR reduction by TMPD. A mixture of 20 mM α-D-glucose and 200 U/mL *Aspergillus niger* glucose oxidase (MP biomedical) enzyme was used to scrub oxygen from the stopped-flow apparatus. Lyophilized glucose oxidase and glucose were dissolved in buffer inside a glovebox, and the solution was transferred to a tonometer whose stopcocks and caps were greased with Apiezon M Economical High-Vacuum Lubricant. The sealed tonometer was removed from the glovebox and connected to one of the stopped-flow loading ports, from which both stopped flow syringes and the observation cell could subsequently be filled with the scrubbing solution, according to the instructions provided in the SX-20 manual. This solution was left in the stopped-flow overnight to make the system completely anaerobic, after which it was washed out with anaerobic 50 mM HEPES, pH=7.0 buffer, again following the SX-20 manual instructions. Stock reagent solutions were made in a glovebox as described previously in section 2.2.6. From these, one solution containing approximately 2.6 μM wtccNiR and 4 mM nitrite in 50 mM HEPES, pH = 7.0 was prepared and transferred into one tonometer, while 50 mM HEPES, pH = 7.0 solutions containing TMPD concentrations ranging from 100 μM to 10 mM TMPD and 20 μM ferricyanide (to generate TMPD$^+$) were used to fill a second set of tonometers. A tonometer containing only buffer was also prepared in the glovebox, and the solution from this tonometer was used to wash out the glucose-glucose oxidase scrubbing solution (see above), and also to blank the stopped-flow spectrophotometer. The tonometer containing nitrite-loaded ccNiR was used to fill one of the stopped-flow drive syringes, while one of the

69

TMPD solutions was used to fill the other. The solutions were mixed 1:1 by the stopped-flow drive piston. Initially, data sets were collected on 2 s, 10 s, 50 s and 120 s timescales. These preliminary experiments showed that the optimal collection mode was logarithmic over a 50s time period, after which all subsequent experiments were collected in this mode. Each experiment at a certain TMPD concentration was repeated 3 – 5 times; the first two datasets were typically discarded, and the 3rd, 4th and 5th signal-averaged. All the data were collected in photodiode array (PDA) mode. Data were collected in csv format and later analyzed by using programs written for Mathcad 15.0 (PTC Software) and Origin 9.0 (Microcal Software).[9-10]

2.2.7.2. Stopped-Flow Experiments at varying pH. A procedure similar to that described in section 2.2.7.1 was used to study the effect of pH on the kinetics of nitrite-loaded wtccNiR reduction by TMPD. Experiments were carried out in the pH range from 6.0 to 8.4 at pH intervals of 0.2 units. Buffer solutions were made in 50 mL batches on the benchtop, purged with argon for 30 minutes, then taken into the glove box. Bis-tris was used for making buffers at pH 6.00, 6.20, 6.40, 6.60, HEPES for buffers at pH 6.80, 7.00, 7.20, 7.40, 7.80 and HEPPS for 8.00, 8.20, 8.40. In all experiments one of the stopped-flow drive syringes was filled with a solution containing 8 mM nitrite with 2 μM wtccNiR, and the other with a solution containing 16 mM TMPD and 20 μM ferricyanide; both solutions were made up in buffers of the desired pH.

2.3. Results

2.3.1. Steady-state experiments

2.3.1.1. Effect of TMPDox on ccNiR-catalyzed reduction of nitrite by TMPD. The blue traces in Fig. 2.2a show the typical UV/Vis spectral changes observed after mixing *S. oneidensis* ccNiR with large excesses of nitrite and TMPD, at pH 7, using the protocol previously

described in ref. [2]. The reaction mixture was monitored by UV/vis at 15 s intervals for 1h, but for clarity the blue traces in Fig. 2.2a are at 600 s intervals. Figure 2.2b shows an absorbance vs time slice taken at 611 nm. SVD analysis[13-14] showed that only two components were needed to faithfully reconstruct a noise-reduced absorbance matrix. The SVD-treated data were then fit to Eq 2.1 using a global fitting routine (red traces, Fig. 2.2a).[9-10] In Eq 2.1 $A_{\lambda,t}$ is the absorbance obtained at wavelength λ and time t, and the spectral component Λ_0 is present immediately after adding nitrite (taken as $t = 0$). The second component in Eq. 2.1, Λ_1, grows in almost linearly with time, but with a slight acceleration that is apparent in Fig. 2.2b. To account for the acceleration, Λ_1 is multiplied by the quadratic binomial $t+qt^2$ in Eq. 2.1, where q is a manually adjusted empirical parameter that allows small admixture, typically ~0.015%, of the quadratic term that improves the empirical fit.

$$A_{\lambda,t} = \Lambda_{0(\lambda)} + \Lambda_{1(\lambda)}(t + qt^2) \qquad (2.1)$$

Figure 2.3 shows the spectral components obtained from the fitting process. The component Λ_0 (Fig. 2.3a) was in its turn fit with the independently obtained extinction coefficient spectrum of 2-electron reduced nitrite loaded ccNiR, $\{Fe_{H1}NO\}^7$, and that of the blue TMPD$^+$ radical.[2] As noted in our earlier work, the fit shows that nitrite-loaded ccNiR is rapidly reduced by two equivalents of TMPD to generate the $\{Fe_{H1}NO\}^7$ active site. The spectral component Λ_1 (Fig. 2.3b) was fit with the extinction coefficient spectrum of the TMPD$^+$ radical,[15] and shows that TMPD continued to oxidize at an initial rate of $\sim 4.3 \times 10^{-8}$ M s^{-1}, with a slight acceleration with time, after the initial oxidation burst. This TMPD$^+$ generation correlated with the catalytic reduction of nitrite to NO·, previously observed in our laboratories under weakly reducing conditions.[1]
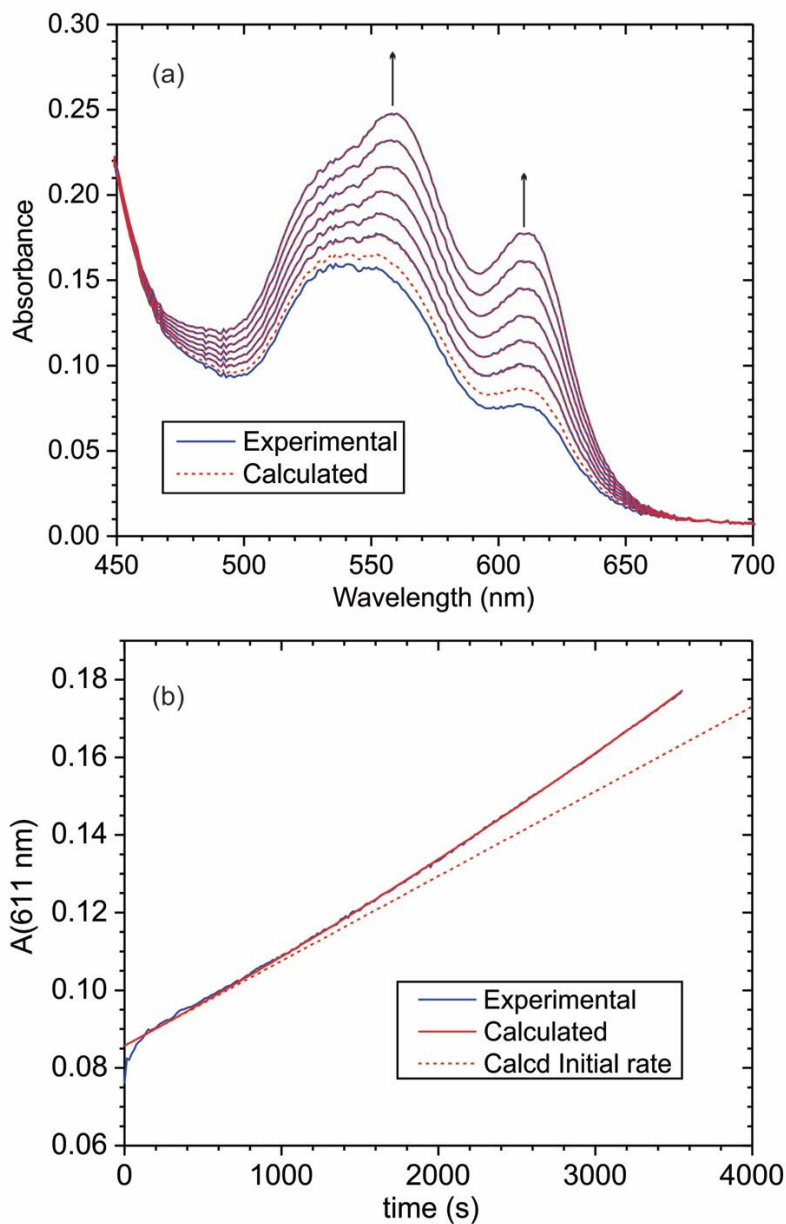
Figure 2.2. (a) Blue traces: typical UV/Vis spectral changes observed after mixing *S. oneidensis* ccNiR (2 μM) with 1 mM nitrite and 600 μM TMPD, at pH 7. Red traces: least-squares best fit to Eq. 2.1. The reaction mixture was monitored at 15 s intervals for 1h, but for clarity the selected traces are at 600 s intervals. (b) Absorbance vs time slice taken at the 611 nm maximum of the data set above. The solid red line is the best fit to Eq. 2.1, while the dashed red line is the initial rate calculated from the first derivative of Eq. 2.1. The fit to Eq. 2.1 deviates from the experimental data near t = 0 where ccNiR reduction is still taking place (see Section 2.3.2).
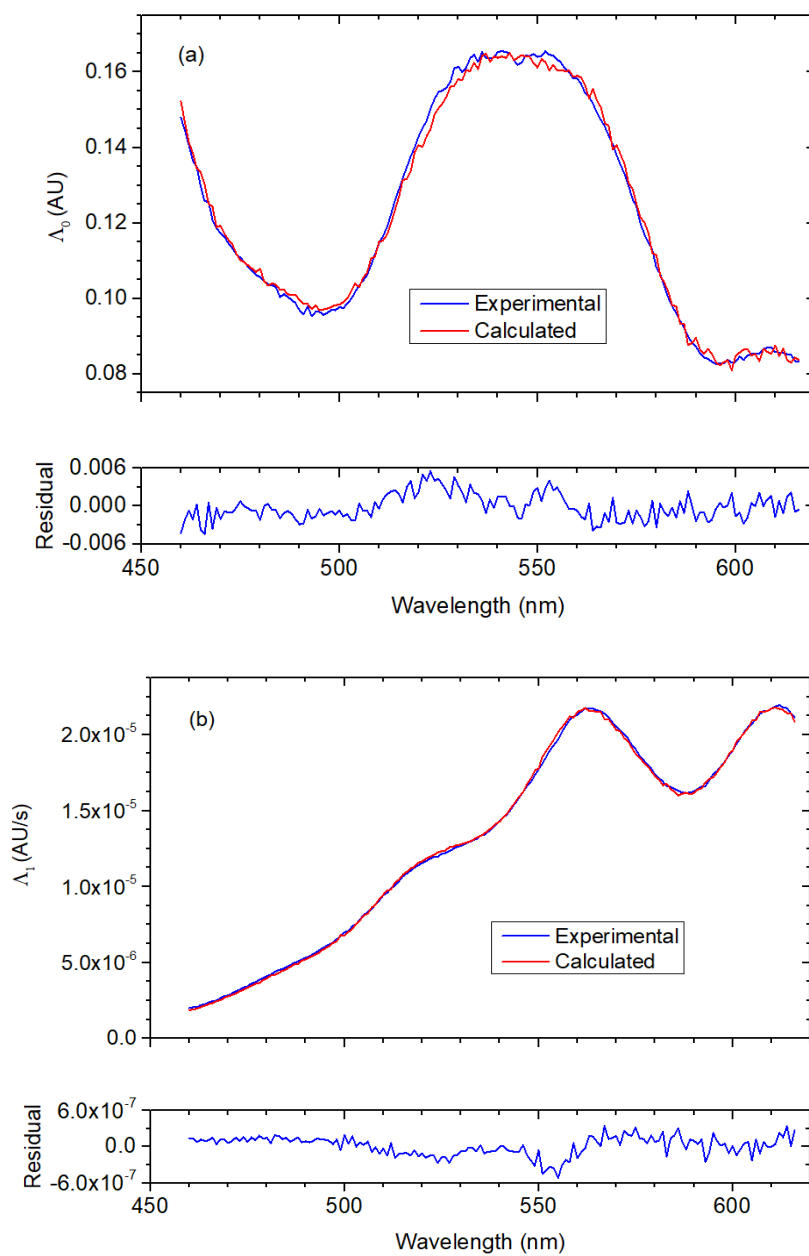
Figure 2.3. Spectral components Λ_0 (a) and Λ_1 (b) generated by fitting the SVD-processed Fig. 2.2 data to Eq 2.1 (blue traces). Λ_0 was in turn fit with the extinction coefficient spectra of reduced nitrite-loaded ccNiR and of the blue TMPD$^+$ radical, while Λ_1 was fit using only the TMPD$^+$ extinction coefficient spectrum.[2] The red traces show the calculated spectra in each case.

That ccNiR was catalyzing TMPD oxidation by nitrite was confirmed by monitoring the dependence of the TMPD oxidation rate on ccNiR concentration.

The acceleration with time seen in TMPD$^+$ formation suggests that TMPD$^+$ itself could be causing the acceleration. To test this hypothesis, a series of experiments analogous to the one shown in Fig. 2.2 was carried out in the presence of varying initial concentrations of TMPD and TMPD$^+$; two representative data sets are shown in Fig. 2.4. Figure 2.4a shows that, in the presence of 600 μM TMPD, the ratio of initial rate of TMPD oxidation to ccNiR concentration (V_o/[ccNiR], obtained from fits of the corresponding Λ_1 components) increased linearly when the initial concentration of TMPD$^+$ was varied from 0 to 50 μM. The slope of the line was 29.0 ± 0.1 M^{-1}s^{-1}, and the intercept in the absence of TMPD$^+$ was $(8.3\pm0.4)\times10^{-4}$ s^{-1}. Similar results were obtained with TMPD concentrations of 400 μM and 800 μM. However, when the initial TMPD concentration was increased to 3 mM, V_o/[ccNiR] remained constant at $(1.02\pm0.07)\times10^{-3}$ s^{-1} as the initial TMPD$^+$ concentration was varied from 0 to 50 μM (Fig. 2.4b). These results confirm that the rate of TMPD oxidation is accelerated as the TMPD$^+$ concentration increases, but that the effect of TMPD$^+$ becomes less pronounced as the total TMPD concentration increases. The results also show that TMPD oxidation can take place in the absence of any TMPD$^+$, in a base process with a first-order rate constant of $\sim10^{-3}$ s^{-1}.

2.3.1.2. Effect of nitrite concentration on ccNiR-catalyzed reduction of nitrite by TMPD. Figure 2.5 shows the dependence of V_o/[ccNiR] on nitrite concentration. Surprisingly, V_o/[ccNiR] *decreases* hyperbolically as the nitrite concentration increases from 50 μM to 10 mM. This behavior is quite different to that seen in the standard assay where methyl viologen monocation radical serves as the electron donor,[3] and is also different from that seen when
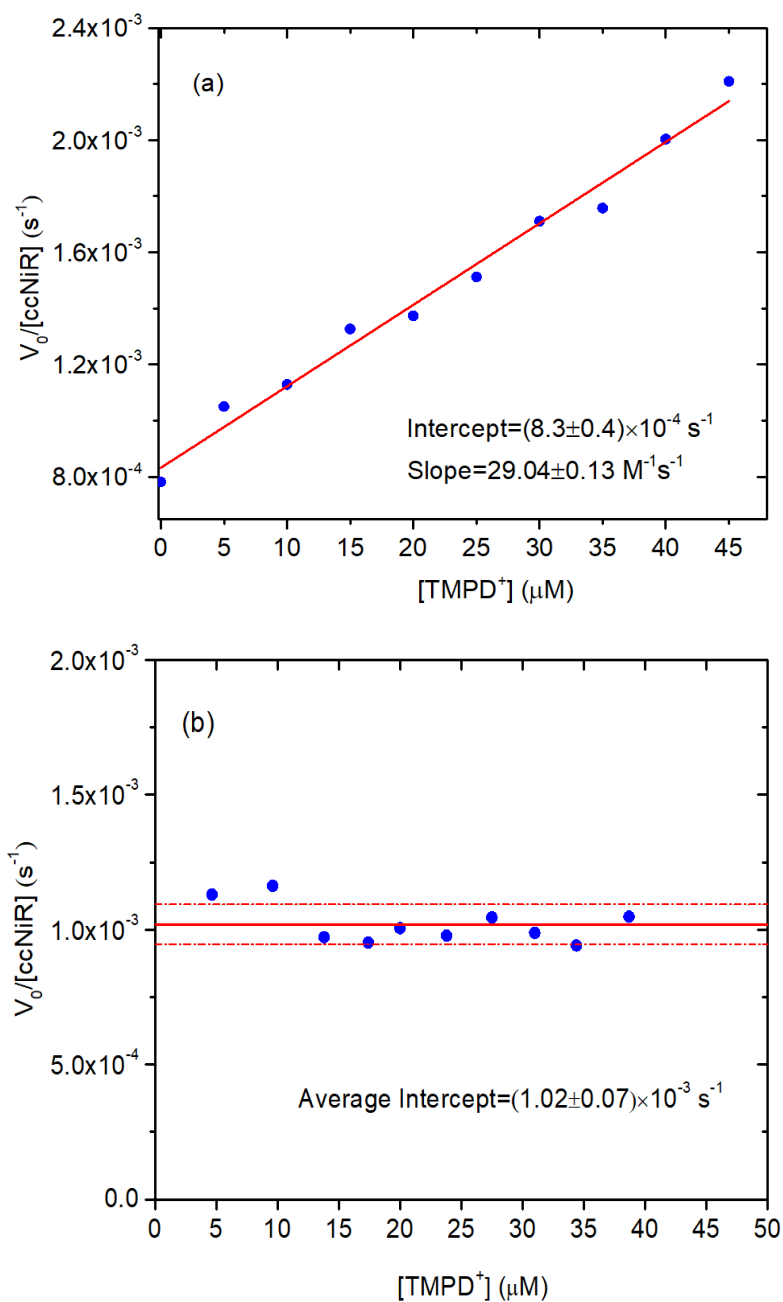
Figure 2.4. Dependence of $V_0/$[ccNiR] (where V_0 is the initial rate of TMPD oxidation in M/s, obtained from fits of the corresponding Λ_1 components) on initial TMPD$^+$ concentrations in the presence of (a) 600 μM TMPD, and (b) 3 mM TMPD. The nitrite concentration was 1 mM in all experiments, and the ccNiR concentration was roughly 2 μM, with the exact concentration being obtained from the Λ_0 fits in each experiment. All experiments were in 50 mM HEPES buffer, pH 7.0

ferrocyanide was the electron donor.[1] In both those cases V_o/[ccNiR] increases hyperbolically with nitrite concentration. The Fig. 2.5 data were fit to Eq. 2.2, in which $k_{cat(i)}$ is the value of V_o/[ccNiR] expected as the nitrite concentration approaches

$$\frac{V_o}{[ccNiR]} = k_{cat(i)} + \frac{\left(k_{cat(f)} - k_{cat(i)}\right)[NO_2^-]}{K_m + [NO_2^-]}$$ (Eq 2.2)

zero, $k_{cat(f)}$ is the value of V_o/[ccNiR] expected as the nitrite concentration goes to infinity, and K_m is the nitrite concentration at which V_o/[ccNiR] is half-way between $k_{cat(i)}$ and $k_{cat(f)}$. The values obtained from the fit were $(2.4\pm0.2)\times10^{-3}$ s^{-1} for $k_{cat(i)}$, $(6\pm2)\times10^{-4}$ s^{-1} for $k_{cat(f)}$, and $(1.5\pm0.4)\times10^{-4}$ M for K_m.
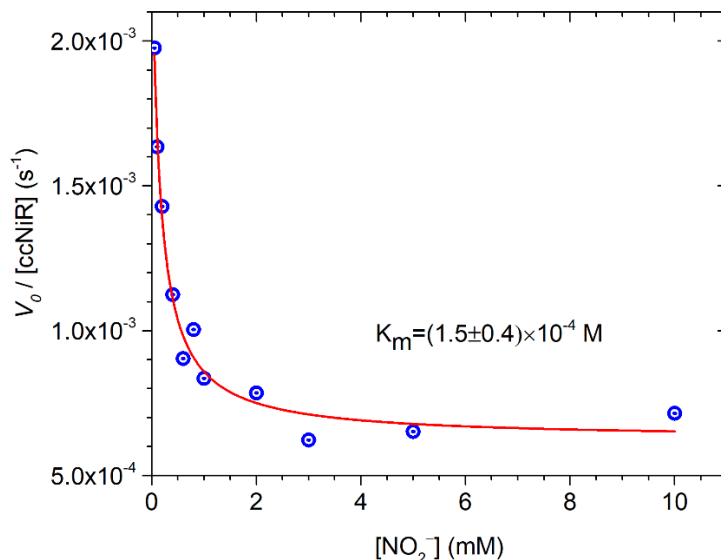
Figure 2.5. Dependence of V_0/[ccNiR] on initial nitrite concentrations (where V_0 is the initial rate of TMPD oxidation in M/s, obtained from fits of the corresponding Λ_1 components). Blue circles are the experimental data, and the red curve is the least-squares best fit to Eq. 2.2. Experimental conditions: [TMPD], 1 mM; [ccNiR], ~1.8 μM (exact concentration measured in each experiment from the Λ_0 component fits); 50 mM HEPES, pH 7.0.

2.3.2. Stopped-flow experiments

2.3.2.1. Reaction of nitrite-loaded ccNiR with TMPD at pH 7. Figure 2.2 shows that, in the first several seconds after mixing, the fit of steady-state data to Eq. 2.1 deviates from the experimental data because ccNiR reduction is still taking place. To explore the kinetics of ccNiR reduction, this timescale was therefore monitored using UV/Vis stopped-flow. The experiments were carried out with diode array detection so that spectral changes could be monitored across a wide range of wavelengths. Figure 2.6a shows the spectral changes obtained when a solution containing 3 μM ccNiR and 4 mM nitrite was mixed 1:1 with a solution containing 10 mM TMPD and 20 μM ferricyanide; both solutions were in 50 mM HEPES buffer, pH 7.0. Figure 2.6b shows Absorbance vs time slices taken at selected wavelengths from the spectra of Fig. 2.6a. SVD analysis[13-14] showed that four components were needed to faithfully reconstruct a noise-reduced absorbance matrix. The SVD-treated data were then fit to Eq 2.3 using a global fitting routine (red traces, Fig. 2.6a).[9-10, 16] In Eq. 2.3, $A_{\lambda,t}$ is the absorbance obtained at wavelength λ and time t, and Λ_0 to Λ_3 are the spectral components.

$$A_{\lambda,t} = \Lambda_{0(\lambda)} + \Lambda_{1(\lambda)} \cdot f_1(t) + \Lambda_{2(\lambda)} \cdot f_2(t) + \Lambda_{3(\lambda)} \cdot f_3(t)$$
$$where:$$
$$f_1(t) = \frac{k_{1app}}{k_{2app} - k_{1app}} \left[\exp\left(-k_{1app}t\right) - \exp\left(-k_{2app}t\right) \right] \qquad \text{Eq. 2.3}$$
$$f_2(t) = \frac{1}{k_{2app} - k_{1app}} \left[k_{2app}\left(1 - \exp\left(-k_{1app}t\right)\right) - k_{1app}\left(1 - \exp\left(-k_{2app}t\right)\right) \right]$$
$$f_3(t) = 1 - \exp\left(-k_3 t\right)$$

Component Λ_0 is present at t = 0, Λ_1 grows in exponentially at a rate governed by k_{1app}, and then decays exponentially at a rate governed by k_{2app}, and Λ_2 grows in as Λ_1 decays, at a rate
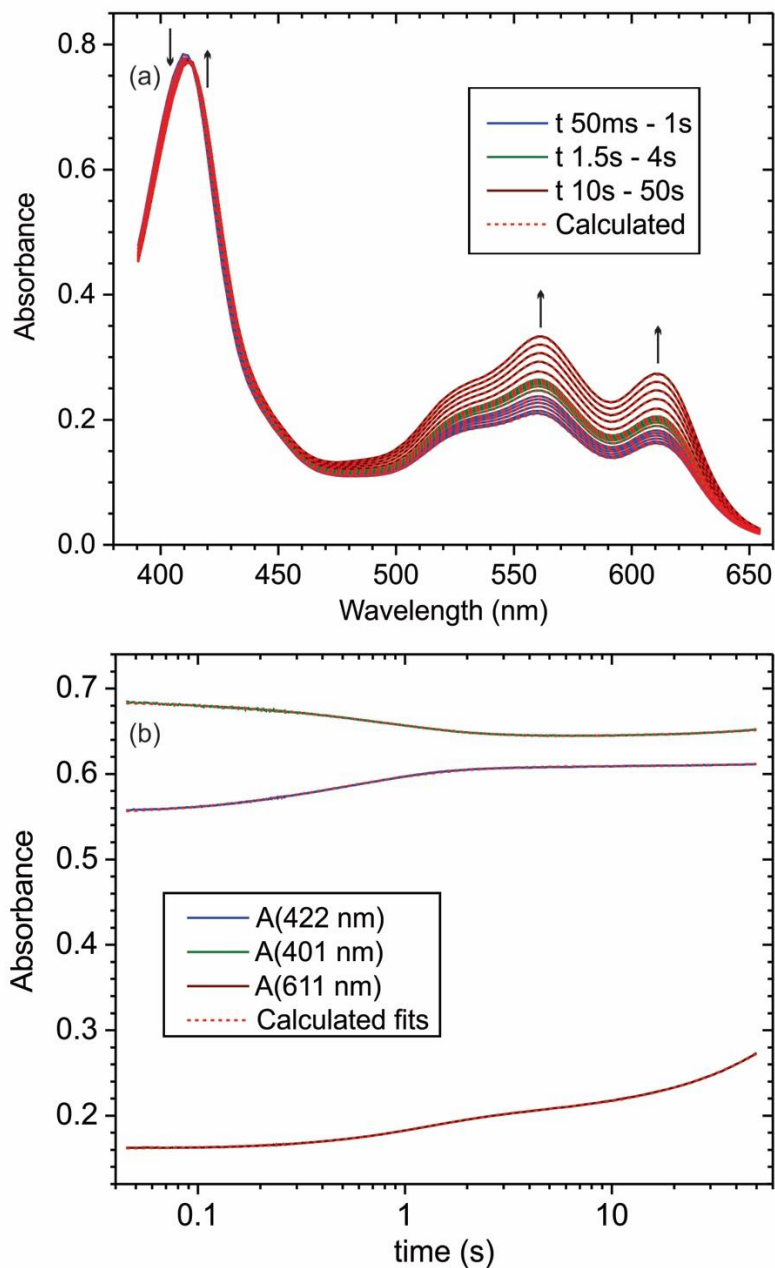
Figure 2.6. (a) Spectral changes obtained when a solution containing 3 μM ccNiR and 4 mM nitrite was mixed 1:1 with a solution containing 10 mM TMPD and 20 μM ferricyanide; both solutions were in 50 mM HEPES buffer, pH 7.0. The blue traces are at 50 ms, 200 ms, 400 ms, 600 ms 800 ms and 1s; the green traces are at 500 ms intervals from 1.5 s to 4s, and the purple traces are at 10 s intervals from 10s to 50 s. The dashed red traces are least-squares best fits to Eq. 2.3. (b) Absorbance vs time slices taken at selected wavelengths from the spectra of Fig. 2.6a. Again, the dashed red traces are the least-squares best fits to Eq. 2.3.

governed by both k_{1app} and k_{2app}. Note that Λ_0 should decay exponentially as Λ_1 grows in, at a rate governed by k_{1app}. By treating Λ_0 as a constant, Λ_1 and Λ_2 will appear as difference spectra.

The component Λ_3 can be attributed almost exclusively to the linear appearance of TMPD$^+$ predicted from the steady-state experiments of Section 2.3.1 (see below); however, a better fit was obtained when Λ_3 was multiplied by the empirical exponential function $f_3(t)$, in which a rate constant k_3 allowed a very slight curvature to be introduced to the Λ_3 evolution. The nonlinearity of this component is likely an artifact that arises because components Λ_2 and Λ_3 are not perfectly resolved by SVD and mix a little.

Figure 2.7 shows the spectral components Λ_0 - Λ_3 obtained from the least-squares fit to Eq. 2.3. As mentioned above, Λ_3 (Fig. 2.7d) can be attributed almost exclusively to the steady-state formation of TMPD$^+$ during ccNiR-catalyzed nitrite reduction by TMPD and will not be further discussed here. The component Λ_0 (Fig. 2.7a), present at t = 0, was fit with the extinction coefficient spectra of nitrite-loaded ccNiR, and of the blue TMPD$^+$ radical, to obtain the initial concentrations of the species. For this experiment, the total ccNiR and TMPD$^+$ concentrations at t = 0 were measured at 1.4 μM and 10 μM, respectively, as expected from the nominal reagent concentrations in the drive syringes (3 μM for ccNiR in syringe 1 and 20 μM ferricyanide in syringe 2; see above). The third component, Λ_2 (Fig. 2.7c), was well fit with the extinction coefficient difference spectrum {Fe$_{H1}$NO}^{7} – [Fe$_{H1}^{III}$ (NO$_2^-$)] and the extinction coefficient spectrum of the TMPD$^+$ radical.[2] As mentioned above, the spectrum appears as a difference because Λ_0 isn't multiplied by exp($-k_{1app}t$) in Eq. 2.3. This is advantageous because the spectral changes due to ccNiR reduction are small and difficult to see clearly in the absolute spectra (Fig. 2.6a). The best fit was obtained with the concentration of [Fe$_{H1}^{III}$ (NO$_2^-$)] reduced to {Fe$_{H1}$NO}^{7} set to 1.3 μM, and that of TMPD oxidized to TMPD$^+$ set to 3.6 μM. The ratio of TMPD oxidized
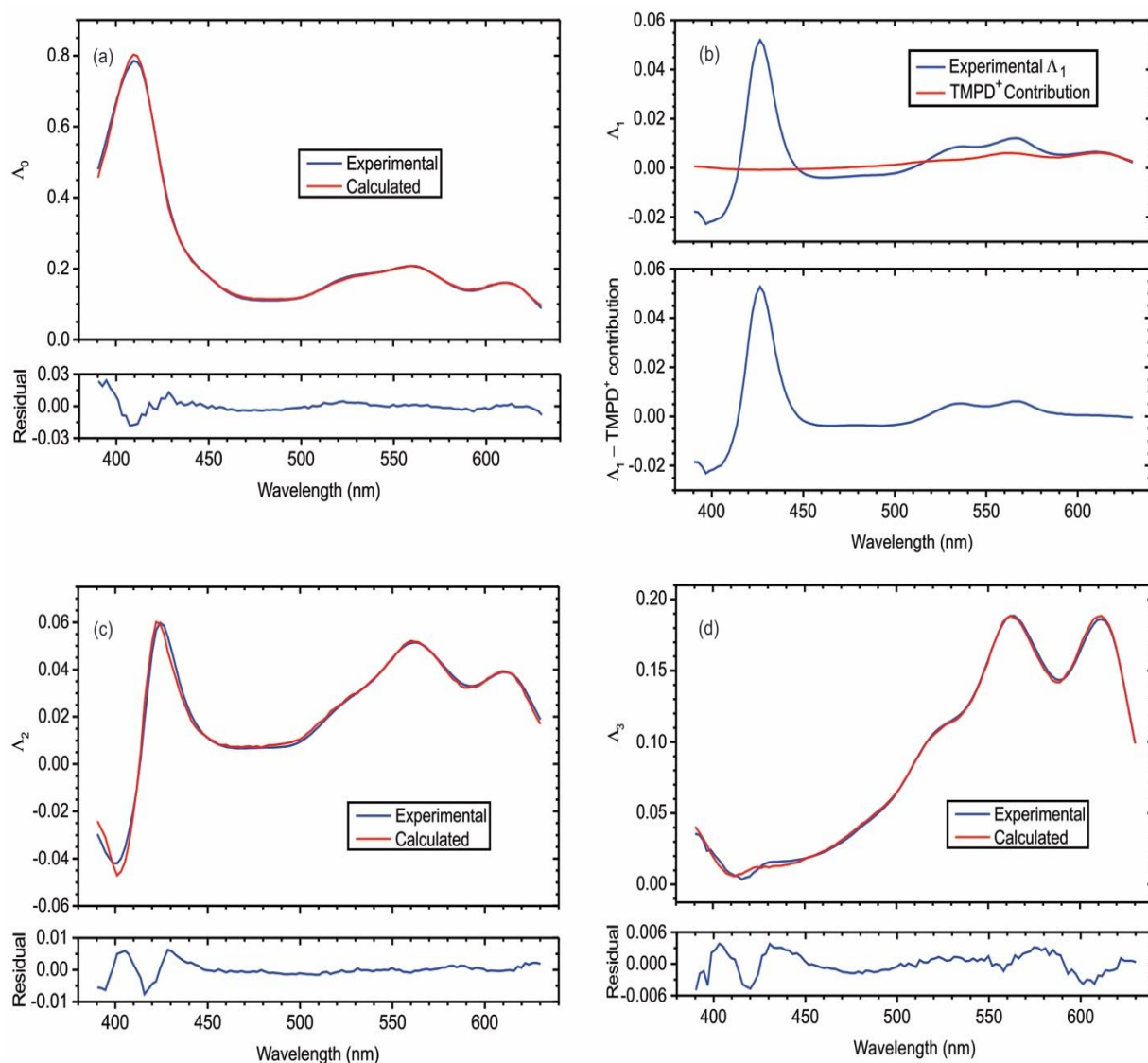
Figure 2.7. Spectral components $\Lambda_0 - \Lambda_3$ generated by fitting the SVD-processed Fig. 2.6 data to Eq 2.3 (blue traces, upper panels of (a) – (d). (a) Red trace: Λ_0 was fit with the extinction coefficient spectra of nitrite-loaded ccNiR and of the blue TMPD$^+$ radical to obtain the initial concentrations of the species. (b) Red trace upper panel: contribution from the TMPD$^+$ radical that was subtracted from Λ_1 to give the difference spectrum in the lower panel; this is taken to be the difference spectrum of 1-electron reduced and oxidized nitrite-loaded ccNiR. (c) Red trace: Λ_2 was fit with the extinction coefficient difference spectrum $\{Fe_{H1}NO\}^7 - [Fe_{H1}{}^{III}(NO_2{}^-)]$ and the extinction coefficient spectrum of the TMPD$^+$ radical to obtain the concentrations of the species as t $\to\infty$.[2] (d) The red trace is the least-squares fit of Λ_3 with the extinction coefficient spectrum of the TMPD$^+$ radical. The excellent fit shows that the final component is due exclusively to TMPD oxidation (a very minor contribution from c-heme reduction is most likely artifactual mixing in the SVD process).

to ccNiR reduced is 2.8, higher than the 2.0 expected for a 2-electron reduction of $[Fe_{H1}^{III}(NO_2^-)]$ to $\{Fe_{H1}NO\}^7$. The absolute concentration of ccNiR reduced, 1.3 μM, is close to the total ccNiR concentration verified by the Λ_0 analysis above (1.4 μM).

The transient spectral component Λ_1 (top panel, Fig. 2.7b) is attributed to a mix of $TMPD^+$ and the 1-electron reduced ccNiR species $[Fe_{H1}^{II}(NO_2^-)]$ (see Discussion section 2.4.2.1 below), for which the UV/Vis extinction coefficient spectrum is not yet available. To obtain a rough estimate of what the $[Fe_{H1}^{II}(NO_2^-)]$ - $[Fe_{H1}^{III}(NO_2^-)]$ difference spectrum looks like, the spectral contribution due to $TMPD^+$ (red trace, Fig. 2.7b) was subtracted from Λ_1, taking advantage of the fact that the $TMPD^+$ spectrum has a sharp absorbance maximum at 611 nm where the ccNiR spectrum is relatively smooth. The resulting difference spectrum is shown in the lower panel of Fig. 2.7b. The difference spectrum looks similar to that of $\{Fe_{H1}NO\}^7 - [Fe_{H1}^{III}(NO_2^-)]$, except that it has relatively well defined maxima at 537 nm and 568 nm, whereas the $\{Fe_{H1}NO\}^7 - [Fe_{H1}^{III}(NO_2^-)]$ difference spectrum displays a single broad band at 555 nm.[2]

When the experiment of Figs. 2.6 and 2.7 was repeated in the presence of varying TMPD concentrations, both k_{1app} and k_{2app} were found to vary linearly with [TMPD] (Fig. 2.8). For k_{1app} (Fig. 2.8a), the linear fit gave a slope of 400±10 $M^{-1}s^{-1}$ and an intercept of 0.63± 0.02 s^{-1}, which indicates that k_{1app} is governing a reaction towards an equilibrium.[17] In that case, the linear dependence of k_{1app} on TMPD concentration can be interpreted as shown in Eq. 2.4,

$$k_{1app} = k_1[TMPD] + k_{-1app} \qquad \text{Eq. 2.4}$$

where k_1 is the second-order rate constant for the forward reaction of a process that is first order in [ccNiR] and first order in [TMPD], and k_{-1app} is the [TMPD]-independent first-order rate

constant for the reverse reaction. Presumably, k_{-1app} would depend on the concentration of $TMPD^+$ (see Discussion); however, this has not yet been verified. From the values of k_1 and k_{-1app} one can calculate an apparent equilibrium constant at 10 μM $TMPD^+$ of $K_1 = 635\pm35$ M^{-1}. Perhaps more useful is the inverse equilibrium constant, $K_1^{-1} = 1.57\pm0.09$ mM, which predicts the TMPD concentration at which $[Fe_{H1}^{III}(NO_2^-)]$ and the putative 1-electron reduced ccNiR species $[Fe_{H1}^{II}(NO_2^-)]$ will be 1:1 at equilibrium (in the presence of 10 μM $TMPD^+$).

For k_{2app} (Fig. 2.8b), the linear fit gave a slope k_2 of 160 ± 6 $M^{-1}s^{-1}$ and an intercept of effectively zero, meaning that the reverse reaction for this process is too small to measure from analysis of the k_{2app} dependence on [TMPD]. However, the amplitude of the Λ_2 component (Fig. 2.7c) was also found to depend on TMPD concentration; as $[Fe_{H1}^{III}(NO_2^-)]$ reduction to $\{Fe_{H1}NO\}^7$ is a major contributor to the Λ_2 difference spectrum, the dependence of the Λ_2 amplitude on [TMPD] indicates that some measurable back-reaction from $\{Fe_{H1}NO\}^7$ to $[Fe_{H1}^{III}(NO_2^-)]$ also takes place. Figure 2.9 shows how the accumulation of $\{Fe_{H1}NO\}^7$, obtained by fitting the corresponding Λ_2 components with the known extinction coefficient spectra, as shown in Fig. 2.7c, varies with TMPD concentration. The data were fit with the rectangular hyperbola of Eq. 2.5. The fit gave $(5.5\pm0.8)\times10^{-4}$ M as the value of K_2^{-1}, and 1.34 ± 0.06 μM for the

$$\{Fe_{H1}NO\}^7 = \frac{ccNiR_{tot} \cdot [TMPD]}{K_2^{-1} + [TMPD]}$$
Eq. 2.5

total ccNiR concentration. The latter was in agreement with the average ccNiR concentration used in the experiments, 1.24 ± 0.15 μM, as measured from the corresponding Λ_0 components.
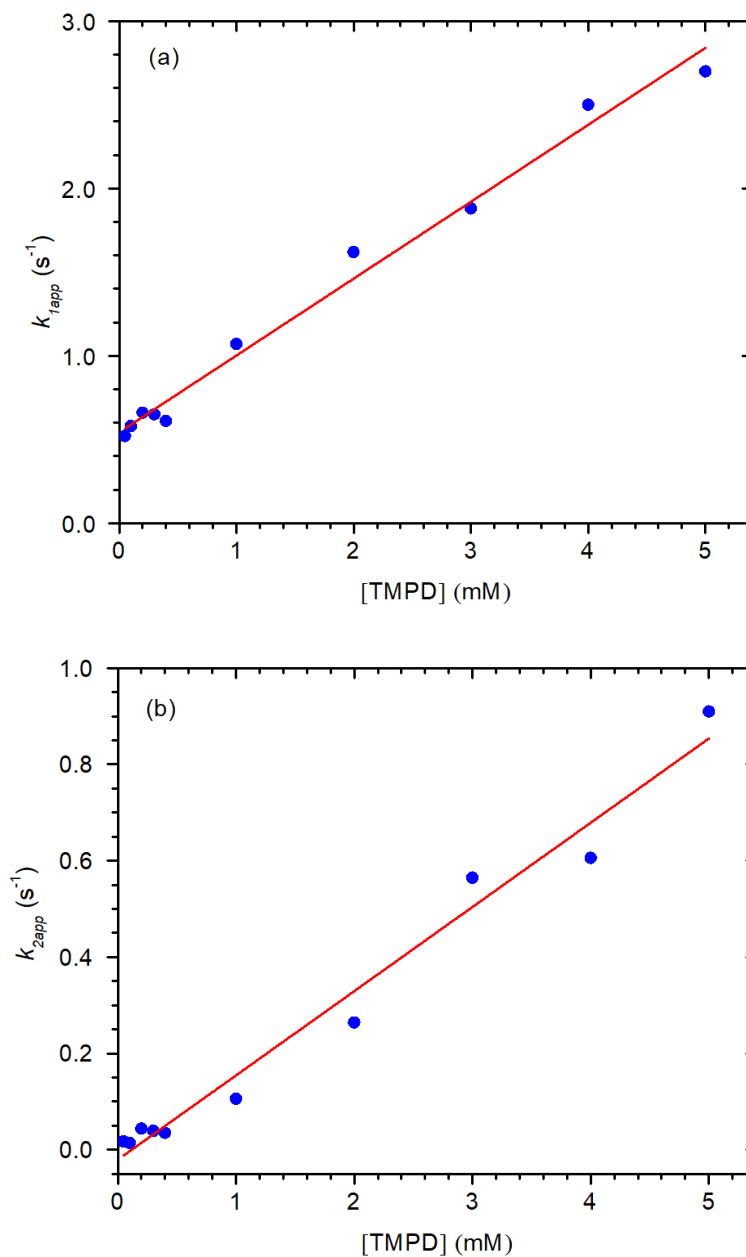
Figure 2.8. The dependence of k_{1app} (a) and k_{2app} (b) from Eq. 2.3 on TMPD concentration. Blue circles: experimental data; red lines: linear least-squares fit to the data. For k_{1app}, the linear fit gave a slope of 400 ± 10 $M^{-1}s^{-1}$ and an intercept of 0.63 ± 0.02 s^{-1}. For k_{2app}, the linear fit gave a slope of 160 ± 6 $M^{-1}s^{-1}$ and an intercept of effectively zero (0.01 ± 0.01 s^{-1}). For all experiments the total ccNiR concentration was 1.24 ± 0.15 μM, the initial TMPD$^+$ concentration (generated by addition of ferricyanide) was 9 ± 2 μM, and the nitrite concentration was 4 mM.
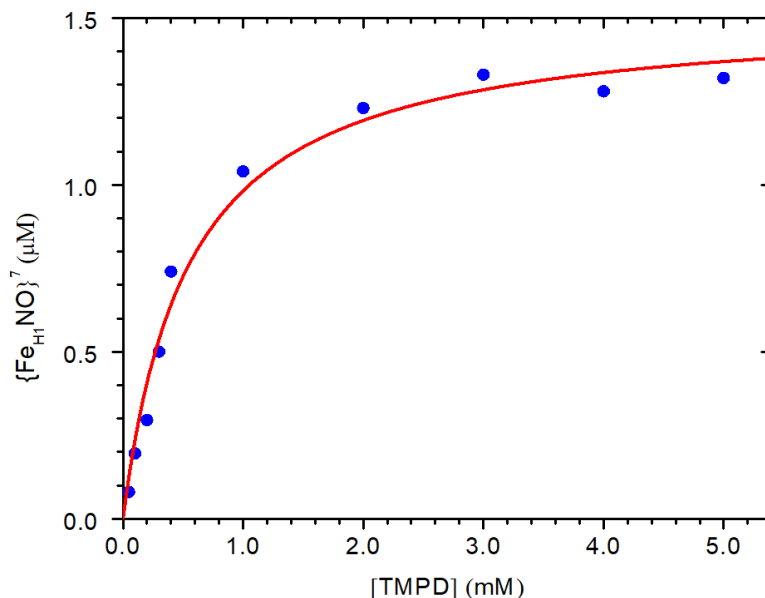
Figure 2.9. Accumulation of $\{Fe_{H1}NO\}^7$ following 2-electron reduction of nitrite loaded ccNiR by TMPD. Blue circles: experimental results; red curve: least-squares fit to the rectangular hyperbola of Eq. 2.5. The fit gave $(5.5\pm0.8)\times10^{-4}$ M^{-1} as the value of K_2^{-1}. The $\{Fe_{H1}NO\}^7$ concentrations were obtained by fitting the corresponding Λ_2 components with the known extinction coefficient spectra, as shown in Fig. 2.7c.

2.3.2.2. pH-dependence for the reaction between nitrite-loaded ccNiR and TMPD.

Figure 2.10 shows how k_{1app} and k_{2app} vary with pH, in the range from 6.0 to 8.4, when the initial concentrations of ccNiR, nitrite, TMPD and TMPD$^+$ are held constant at 1.2 µM, 4 mM, 8 mM and 10 µM, respectively. Figure 2.10a shows that the value of k_{1app} is essentially invariant at 3.31 $\pm$ 0.01 s^{-1} as the pH is varied; the value is as predicted from the Fig 2.8a results for 8 mM TMPD. On the other hand, Figure 2.10b shows that k_{2app} varies appreciably with pH. The rate constant initially increases as pH increases from pH 6, reaches a maximum at approximately pH = 6.8, then decreases again, leveling out above pH 8. The experimental data were well fit by Eq. 2.6, which is based on the model shown in Scheme 2.2. In the model, ccNiR goes from a fully

$$k_{2app} = \frac{k_{pH1} + k_{pH2} \cdot 10^{(pH-pKa1)} + k_{pH3} \cdot 10^{(pH-pKa1)} \cdot 10^{2(pH-pKa2)}}{1 + 10^{(pH-pKa1)} + 10^{2(pH-pKa2)} + 10^{(pH-pKa1)} \cdot 10^{2(pH-pKa2)}} \qquad \text{Eq. 2.6}$$

protonated form EH_3 to a form EH_2 in a process governed by pK_{a1}, and then loses two protons simultaneously in a process governed by pK_{a2}. The two pK_a values are adjustable parameters in Eq. 2.6, as are $k_{pH1} - k_{pH3}$, which are the k_{2app} rate constants associated with ccNiR-catalyzed nitrite reduction by EH_3, EH_2 and E, respectively. The fit is much better if the second deprotonation involves two protons rather than one. From the fit with Eq. 2.6, pK_{a1} and pK_{a2} were found to be 7.25 and 6.93, respectively

$$EH_3 \rightleftharpoons EH_2 + H^+ \quad pK_{a1}$$

$$EH_2 \rightleftharpoons E + 2H^+ \quad pK_{a2}$$
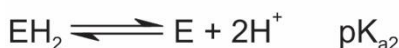
Scheme 2.2. Minimal model to explain the observed pH dependence of ccNiR-catalyzed nitrite reduction to NO· by TMPD. Low-pH enzymatic species EH_3 loses a single proton (pK_{a1}) to yield the maximally active species EH_2, which then loses two protons (pK_{a2}) in a concerted step to generate the minimally active high-pH species E. The fit is much better if two protons are involved in step 2.

2.4. Discussion

The steady-state and stopped-flow results presented herein can be understood in terms of the species and steps shown in Scheme 2.3, which are consistent with earlier results from our laboratory,[2] and for the most part, also consistent with the theoretical studies of Bykov and Neese (Section 1.6.2).[18-21] At high concentrations of nitrite most of the ccNiR active site will initially be in the nitrite-loaded form $Fe_{H1}^{III}(NO_2^-)$. Upon addition of the reducing agent TMPD, $Fe_{H1}^{III}(NO_2^-)$ will be rapidly reduced to $Fe_{H1}^{II}(NO_2^-)$, and then more slowly to the 2-electron reduced species

{Fe$_{H1}$NO}^{7}, in a pH-dependent step. These are the steps observed in the stopped-flow studies of Section 2.3.2.
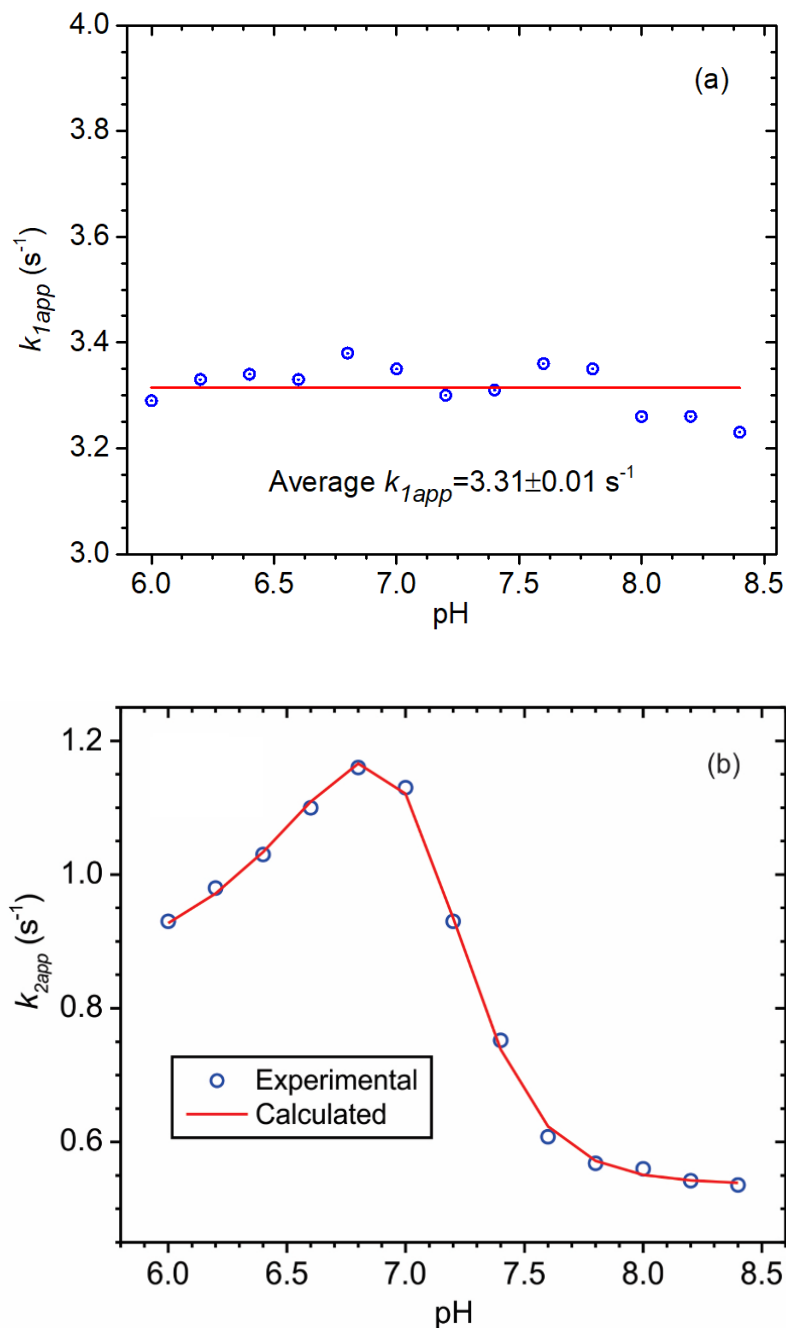
Figure 2.10. The dependence on pH of the rate constants (a) k_{1app} and (b) k_{2app} obtained by fitting the corresponding stopped-flow data to Eq. 2.3. For all experiments the initial concentrations of ccNiR, nitrite, TMPD and TMPD$^+$ are held constant at 1.2 μM, 4 mM, 8 mM and 10 μM, respectively. In Fig. 2.10a the red line represents the average value of k$_{1app}$ across the pH range. The red curve in Fig. 2.10b is the least-squares best fit to Eq. 2.6.

Presumably, reduction of $Fe_{H1}^{III}(NO_2^-)$ to $\{Fe_{H1}NO\}^7$ proceeds via the transient intermediate $\{Fe_{H1}NO\}^{6,[18-19]}$ but both theoretical and experimental studies indicate that the species doesn't accumulate to detectable levels. In spectropotentiometric studies, $Fe_{H1}^{III}(NO_2^-)$ reduced to $\{Fe_{H1}NO\}^7$ in a concerted 2-electron step.[2] In theoretical studies, dehydration of nitrite in $Fe_{H1}^{II}(NO_2^-)$ was identified as the rate-limiting step in reduction of $Fe_{H1}^{III}(NO_2^-)$ to $\{Fe_{H1}NO\}^6$, after which $\{Fe_{H1}NO\}^6$ reduction to $\{Fe_{H1}NO\}^7$ was found to be highly exergonic, and the $\{Fe_{H1}NO\}^7$ state was calculated to be a thermodynamic minimum.[19] These results are consistent with $Fe_{H1}^{II}(NO_2^-)$ rather than $\{Fe_{H1}NO\}^6$ being the intermediate observed by stopped-flow. In their 2012 paper, Bykov and Neese also predicted that $\{Fe_{H1}NO\}^7$ could be further reduced to $\{Fe_{H1}HNO\}^8$ in a nearly thermoneutral CPET step with a 6.5 kcal/mol activation barrier (Step 2, Scheme 1.3).[19] This step is not included in Scheme 2.3 because we have not yet seen convincing evidence for it in our studies; however, the possibility of the step occurring is discussed further in below.

The steady-state results of Section 2.3.1, and earlier results using ferrocyanide as a reductant,[1] show that, under weakly reducing conditions, ccNiR is catalyzing very slow reduction of nitrite to NO·. As a general rule, $\{FeNO\}^6$ heme species tend to be much more labile than their $\{FeNO\}^7$ counterparts, and we had initially assumed that NO· was released exclusively from $\{Fe_{H1}NO\}^6$. However, as discussed further in Section 2.4.1 below, the steady-state results indicate that $\{Fe_{H1}NO\}^7$ also releases NO·, albeit much more slowly than $\{Fe_{H1}NO\}^6$. This pathway is therefore also included in Scheme 2.3.

2.4.1. Steady-state results

2.4.1.1. {Fe$_{H1}$NO}^{7} releases NO·. Figure 2.4 shows that at low TMPD concentrations the steady-state rate of ccNiR-catalyzed reduction of nitrite to NO has linear dependence on [TMPD$^+$], but at higher concentrations it stays constant as TMPD$^+$ concentration increases. At all concentrations, plots of V_0/[ccNiR] vs [TMPD$^+$] have an intercept of ~10^{-3} s^{-1}. These results can be explained with the simple model shown in Scheme 2.4. The model assumes that NO· is released from both {Fe$_{H1}$NO}^{6} and {Fe$_{H1}$NO}^{7} as shown also in Scheme 2.3, and that at steady-state, NO· release is governed by both the rates of dissociation and by the equilibrium between {Fe$_{H1}$NO}^{6} and {Fe$_{H1}$NO}^{7}, which lies far to the right. Applying steady-state treatment to all species except {Fe$_{H1}$NO}^{7}, and making the simplifying assumption that at equilibrium all ccNiR is in the {Fe$_{H1}$NO}^{7} form, gives Eq. 2.7 for the rate of NO· (or TMPD$^+$) formation.

$$V \equiv \frac{d[\text{NO·}]}{dt} = \frac{d[\text{TMPD}^+]}{dt} = [\text{ccNiR}]_{total} \left\{ \frac{(k_{1NO}/k_{red}) \cdot k_{ox}}{[\text{TMPD}] + (k_{1NO}/k_{red})} [\text{TMPD}^+] + k_{2NO} \right\} \qquad \text{Eq. 2.7}$$

Based on Eq. 2.7, the intercept in the Fig. 2.4 plots (~10^{-3} s^{-1}) is k_{2NO}, the constant for dissociation of NO· from {Fe$_{H1}$NO}^{7}. The slopes in plots of V_0/[ccNiR] vs [TMPD$^+$] will be given by the expression in Eq. 2.8. In Fig. 2.4a, obtained with [TMPD] = 600 µM, [NO$_2^-$] = 1 mM and varying [TMPD$^+$], the slope was found to be 29 M^{-1}s^{-1}. In principle, the parameter

$$slope = \frac{(k_{1NO}/k_{red}) \cdot k_{ox}}{[\text{TMPD}] + (k_{1NO}/k_{red})} \qquad \text{Eq. 2.8}$$

k$_{1NO}$/k$_{red}$ could be deconvoluted from k_{ox} by doing experiments at varying TMPD concentrations. Initial attempts to do this by plotting V_0/[ccNiR] vs [TMPD$^+$] at varying [TMPD] concentrations

gave ambiguous results (Fig. 2.4). A better strategy in future may be to do experiments in which [TMPD$^+$] is fixed and [TMPD] is varied over a wider range than was practical when varying both [TMPD] and [TMPD$^+$].

$$\{Fe_{H1}NO\}^6 = [Fe^{II}(NO^+) \longleftrightarrow Fe^{III}(NO^-)]$$

$$\{Fe_{H1}NO\}^7 = [Fe^{II}(NO^-) \longleftrightarrow Fe^{III}(NO^-)]$$

Scheme 2.3. Proposed reaction mechanism of early-stage nitrite loaded *S. oneidensis* ccNiR reduction by TMPD. The initial enzyme-substrate complex, $Fe^{III}_{H1(}NO_2^-)$, undergoes two-electron reduction to form putative intermediate, $\{Fe_{H1}NO\}^7$. At early state when TMPD concentration is low, a quick equilibrium form following one-electron reduction from $Fe^{III}_{H1(}NO_2^-)$ to $Fe^{II}_{H1(}NO_2^-)$ (red dot box), simultaneously the reduction reaction continue to form $\{Fe_{H1}NO\}^7$ (purple dot box). At low TMPD concentration, the equilibrium redirects to initial complex $Fe^{III}_{H1(}NO_2^-)$, and $\{Fe_{H1}NO\}^7$ doesn't accumulate. The second reduction step is proton dependent electron transfer reaction. Here, H1 symbolizes the active site (Heme#1), $\{Fe_{H1}NO\}^7$ conveys the Enemark-Feltham notation (details in the main text).

Scheme 2.4. Steps that are consistent with the steady-state experiments of Section 2.3.1.1.

Scheme 2.4 assumes that at equilibrium all the ccNiR is in the $\{Fe_{H1}NO\}^7$ form. This makes it easy to explain the steady-state results of Fig. 2.4 but is not consistent with the stopped-flow results of Fig. 2.9, which show that at steady-state the $\{Fe_{H1}NO\}^7$ concentration varies hyperbolically with [TMPD] (Eq. 2.5). Indeed, according to the Fig. 2.9 results, the $\{Fe_{H1}NO\}^7$ concentration should only be ~50% of the total ccNiR at 600 μM TMPD. It's easy enough to adjust Eq. 2.7 using the information obtained in the later stopped-flow experiments, but such an adjustment won't change the general mechanistic interpretation presented above. However, accounting for the fraction of ccNiR reduced as a function of [TMPD] present will be critical if future investigators attempt to deconvolute k_{1NO}/k_{red} from k_{ox} in experiments where [TMPD] is varied at fixed [TMPD$^+$], as suggested in the previous paragraph.

2.4.1.2. Nitrite is a substrate inhibitor of ccNiR-catalyzed reduction of nitrite to NO·.
Figure 2.5 shows that V_0/[ccNiR] decreases hyperbolically as nitrite concentration is increased from 50 μM to 10 mM. This was a surprise because, in the standard assay where methyl viologen monocation radical serves as the electron donor,[3] V_o/[ccNiR] *increases* hyperbolically with nitrite concentration with a K_m value of 23 ± 4 μM. A possible explanation for the discrepancy is that different products are released in each case. In the standard assay, where MV_{red} is the electron donor, the product is NH_4^+ which exits the active site via an exit tunnel different from the entrance tunnel used by the anionic nitrite when accessing the active site (Fig. 1.6b).[22] By contrast, in the present case, the product is neutral NO·, which could presumably exit via either the physiological exit channel, lined with anionic residues, or the entry channel lined by cationic ones. One or more nitrites interacting with the cationic residues lining the entry channel could prevent NO· from exiting via that path, thus forcing it to use the NH_4^+ exit channel exclusively. The rate constant for NO· release decreases 4× as nitrite increases, from $(2.4\pm0.2)\times10^{-3}$ s^{-1} for $k_{cat(i)}$ to $(6\pm2)\times10^{-4}$

s^{-1} for $k_{cat(f)}$ (Eq. 2.2). Assuming that the proposed mechanism is correct, this suggests that the nitrite entry channel is a significantly more efficient NO· exit path than the NH_4^+ exit channel.

A possible inconsistency with the mechanism proposed in the previous paragraph is that V_o/[ccNiR] was found to increase hyperbolically with nitrite concentration in ccNiR-catalyzed nitrite reduction to NO· when ferrocyanide was used as the electron donor.[1] This is in agreement with the results seen for ccNiR-catalyzed reduction of nitrite to ammonia by MV_{red}, but opposite to those seen for ccNiR catalyzed reduction of nitrite to NO· by TMPD. However, although the product is the same when ferrocyanide and TMPD are the electron donors, the enzyme species distribution is quite different in the two cases and can explain the kinetic differences.

Ferrocyanide is a much weaker reducing agent than TMPD, so under initial steady-state conditions ccNiR is fully oxidized when the latter is the electron donor. For fully oxidized *S. oneidensis* ccNiR the nitrite dissociation constant is roughly 300 μM, which compares favorably with the K_m value of $(4.5 \pm 0.9) \times 10^{-4}$ M obtained from a hyperbolic fit of V_o/[ccNiR] vs $[NO_2^-]$ for ccNiR-catalyzed nitrite reduction by ferrocyanide.[1] Therefore, when ferrocyanide is the electron donor, the fractional occupancy of the active site by nitrite appears to be a dominant factor in determining the catalytic turnover rate. Even if substrate inhibition does take place under these conditions, it will be masked by the dependence of V_o/[ccNiR] on active site fractional occupancy because the two phenomena evolve in comparable nitrite concentration ranges (~100 μM – 500 μM). On the other hand, when the stronger reducing agent TMPD is the electron donor, it can promote reduction of the nitrite-loaded active site, which drives up its fractional occupancy because both nitrite and NO· have much stronger affinity for ferrous heme compared to ferric.[23] This in turn would make fractional occupancy less of a factor in determining the catalytic turnover rate, and unmask the effects of substrate inhibition of NO· release.

2.4.2. Stopped-flow results

2.4.2.1. Identification of a new intermediate, $Fe_{H1}^{II}(NO_2^-)$. The stopped-flow results of Section 2.3.2.1 clearly show that $Fe_{H1}^{III}(NO_2^-)$ reduction by TMPD is biphasic and reveal a transient intermediate that had not previously been experimentally detected. Scheme 2.5 shows a minimal mechanism that is consistent with the Section 2.3.2.1 results, with the pH-dependence studies of Section 2.3.2.2 (see below), and also with the theoretical calculations of Bykov and Neese.[18-19]

Based on the Scheme 2.5 mechanism, the transient intermediate that rapidly accumulates and then disappears is ascribed to the 1-electron reduced nitrite-loaded active site species $Fe_{H1}^{II}(NO_2^-)$. This is consistent with the observed linear dependence of the apparent rate constant k_{1app} on [TMPD] (Fig. 2.8a and Eq. 2.4), where the slope is the true forward rate constant k_1 (400 ± 10 $M^{-1}s^{-1}$) and the intercept is $k_{-1}[TMPD^+]$ (0.63 ± 0.02 s^{-1} in the presence of 10 μM $TMPD^+$), in step 1 of Scheme 2.5. The Scheme 2.5 interpretation is also consistent with the theoretical studies of Bykov and Neese, which predict that the rate limiting step in reduction of $Fe_{H1}^{III}(NO_2^-)$ to $\{Fe_{H1}NO\}^6$ is addition of the second proton to bound nitrite prior to N – O bond cleavage (Section 1.6.2.2).[18] Theory also predicts that the subsequent reduction of $\{Fe_{H1}NO\}^6$ to $\{Fe_{H1}NO\}^7$ (Step 3, Scheme 2.5) is highly exergonic,[19] so accumulation of this species is not expected.[19]

$$(1) \quad Fe_{H1}^{III}(NO_2^-) + TMPD \underset{k_{-1}}{\overset{k_1}{\rightleftharpoons}} Fe_{H1}^{II}(NO_2^-) + 2TMPD^+$$

$$(2) \quad Fe_{H1}^{II}(NO_2^-) + 2H^+ \underset{k_{-pH}}{\overset{k_{pH}}{\rightleftharpoons}} \{Fe_{H1}NO\}^6 + H_2O$$

$$(3) \quad \{Fe_{H1}NO\}^6 + TMPD \underset{k_{ox}}{\overset{k_{red}}{\rightleftharpoons}} \{Fe_{H1}NO\}^7 + TMPD^+$$
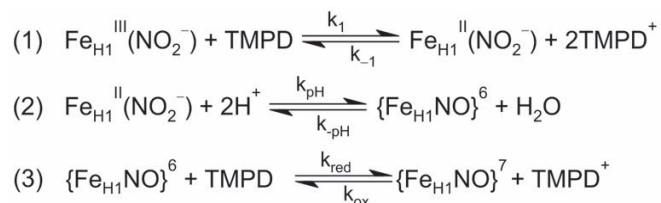
Scheme 2.5. Steps that are consistent with the stopped-flow experiments of Section 2.3.2; NO· formation is assumed to be negligible on this timescale. The rate constants k_{red} and k_{ox} are labeled to be consistent with Scheme 2.4, and k_{pH} is labeled to identify the step that is expected to be pH-dependent.

Assuming that the intercept of Eq. 2.4 is indeed linearly dependent on [TMPD$^+$], which

has not yet been confirmed, the value of the true reverse rate constant k_{-1} is $(7\pm2)\times10^4$ M^{-1}s^{-1}.

This yields an equilibrium constant K_1 of $(6\pm2)\times10^{-3}$, which translates to an unfavorable standard

cell potential of -130 mV for the first equilibrium of Scheme 2.5. From this, and the known

midpoint potential of TMPD (260 mV vs SHE),[7] one can estimate the midpoint potential for 1-

electron reduction of Fe$_{H1}$^{III}(NO$_2$$^-$) to Fe$_{H1}$^{II}(NO$_2$$^-$) to be ~130 mV vs SHE.

2.4.2.2. Reduction of Fe$_{H1}$^{II}(NO$_2$$^-$) to {Fe$_{H1}$NO}^{7}. Applying the steady-state

approximation to {Fe$_{H1}$NO}^{6}, and treating the second reduction step from Fe$_{H1}$^{II}(NO$_2$$^-$) to

{Fe$_{H1}$NO}^{7} (Scheme 2.5, steps 2, 3) independently from the initial reduction of Fe$_{H1}$^{III}(NO$_2$$^-$) to

Fe$_{H1}$^{II}(NO$_2$$^-$) (Scheme 2.5, step1), yields Eq. 2.9 as a theoretical interpretation of k_{2app}, the rate

constant for the second stopped-flow reduction phase. The experiments of Section 2.3.2 show that

k_{2app} is dependent on both pH and [TMPD] (Figs. 2.8b and 2.10), so rate constants for steps 2 and

3 from Scheme 2.5 must both appear in the rate law. Furthermore, step 2 must be set as reversible

to prevent {Fe$_{H1}$NO}^{6} from accumulating at low [TMPD]. Because k_{2app} depends linearly on

[TMPD] and not hyperbolically, the relationship $(k_{-pH}/k_{red}) \gg$ [TMPD] must hold for all TMPD

concentrations tested. This leads to the simplified relationship for k_{2app} in Eq. 2.9 and defines k_2,

the slope of the Fig. 2.8b line, as $k_2 = (k_{pH}/k_{-pH})k_{red}$. Experimentally, this was measured at 160 ± 6

M^{-1}s^{-1} at pH 7 (Section 2.3.2.1).

$$k_{2app} = \frac{k_{pH}[\text{TMPD}]}{\left(k_{-pH}/k_{red}\right)+[\text{TMPD}]} \approx \frac{k_{pH}}{k_{-pH}}k_{red}[\text{TMPD}]$$

Eq. 2.9

The least-squares fit of the Fig. 2.10b pH-dependence data to Eq. 2.6 yielded a pK_{a2} value

of 6.93 for a deprotonation step that lowers the enzymatic activity at high pH by about 50% from

its high point at pH 6.8. These results are in agreement with an earlier pH dependence study done in our lab, in which ccNiR-catalyzed nitrite reduction to NO· by ferrocyanide was monitored by capturing the NO· product with catalase.[1] However, the Fig. 2.10b results showed substantially less scatter than the earlier ones, and allowed the data to be confidently fit with *two pKa* parameters and three enzymatic species, each with different catalytic activity (Section 2.3.2.2). Furthermore, the deprotonation governed by pK_{a2} in the current data fit much better to a model involving a concerted two-proton loss; the earlier data were too noisy to reach such a conclusion with any confidence.

In the earlier pH-dependence experiment, the deprotonation with pK_a = 6.9 was attributed to His257.[1] The apparent involvement of two protons in the pK_{a2} deprotonation of Fig. 2.10b makes assignment to a single amino acid less certain in the current study. A more conservative interpretation is that His257 modulates the pK_a values of one or more of the waters that form a complex hydrogen bonding network in the active site,[2, 22-24] and that pK_{a2} is associated with these waters *and* His253. This interpretation treats pK_{a2} as an empirical parameter more reflective of the broad active site environment than of a single amino acid.

As a final note, in the earlier study, the high-pH species was modeled as being catalytically inactive,[1] whereas the Fig. 2.10 fit shows the high pH species to have about 20% of the most active species' activity (k_{pH2} = 2.4 s^{-1}, k_{pH3} = 0.54 s^{-1} in Eq. 2.6). This may be due to the fact that the weaker reductant ferrocyanide was used in the earlier study, or it may be that the earlier study's large scatter made it difficult to determine the high pH species' activity with any precision.

The linear least-squares fit of the Fig. 2.8b data (k_{2app} vs [TMPD]) yields a zero intercept, indicating that the rate constant for any reverse reaction is too small to be detected from the fit.

However, an equilibrium constant for the second stopped-flow reduction phase can be extracted from the hyperbolic dependence of final $\{Fe_{H1}NO\}^7$ concentration on [TMPD] (Fig. 2.9). The hyperbolic least-squares fit yielded a value of $K_2^{-1} = (5.5\pm0.8)\times10^{-4}$ M (Eq. 2.5, Section 2.3.2.1). From this value, one can extract an estimate of the reverse rate constant. Derivation of a theoretical rate law for the reverse reaction in the second stopped-flow reduction phase yields Eq. 2.10 for the putative observed rate constant k_{-2app}. The equation simplifies to linear form for

$$k_{-2app} = \frac{\left(k_{-pH}/k_{red}\right)k_{ox}[\mathrm{TMPD^+}]}{\left(k_{-pH}/k_{red}\right)+[\mathrm{TMPD}]} \approx k_{ox}[\mathrm{TMPD^+}] \qquad \text{Eq. 2.10}$$

the same reason that Eq. 2.9 does; if $(k_{-pH}/k_{red}) \gg$ [TMPD] in Eq. 2.9, the relationship must also hold in Eq. 2.10. Combining Eq. 2.10 and the definition of k_2 obtained from Eq. 2.9 yields Eq. 2.11 as the theoretical definition of K_2^{-1}. Equation 2.11 can then be used to obtain a value of

$$K_2^{-1} = \frac{k_{-2app}}{k_2} = \frac{k_{ox}[\mathrm{TMPD^+}]}{\left(k_{pH}/k_{-pH}\right)k_{red}} \qquad \text{Eq. 2.11}$$

$(9\pm2)\times10^{-2}$ s^{-1} for k_{ox}[TMPD$^+$] from the experimental values of k_2 and K_2^{-1} obtained from the fits of the Fig. 2.8b and 2.9 data, respectively. Note that this value is also the theoretically predicted intercept for the Fig. 2.8b linear fit. Though the k_{ox}[TMPD$^+$] value calculated from Eq. 2.11 has a large uncertainty, it is clearly non-zero, in contrast to the intercept seen in the Fig. 2.8b linear fit.

There are several possible reasons for the discrepancy between the k_{-2app} value obtained from the linear fit of Fig. 2.8b, zero, and that obtained from the hyperbolic fit of Fig. 2.9, $(9\pm2)\times10^{-2}$ s^{-1}. Most probably, the discrepancy arises from a breakdown of the approximation made in the analysis of Figs. 2.8 and 2.9 that the first and second stopped-flow reduction steps are uncoupled from each other. This is convenient for preliminary analysis of the equilibria involved,

but the approximation is very rough. Indeed, the raw data were fit to Eq. 2.3, which does couple the first and second steps; the uncoupling strategy was used only in the replot analyses of the parameters obtained from the Eq. 2.3 fits. A future analysis that doesn't uncouple the first and second reduction steps may resolve the observed discrepancy. Such an analysis will be much easier to do now that the kinetic parameter values are at least approximately known.

The rate laws used to analyze the Fig. 2.8 and 2.9 data also neglected NO· dissociation, and this too could contribute to the observed discrepancy in k_{-2app} values obtained by the different methods, though the contributions are likely to be minor. At the highest TMPD$^+$ and lowest TMPD concentrations studied, the apparent rate constants for NO· dissociation were in the range of 2×10^{-3} s^{-1} (Fig. 2.4a), which is an order of magnitude below the smallest k_{2app} values obtained by stopped-flow (0.03 s^{-1} when [TMPD] = 40 μM, [TMPD$^+$] = 10 μM, Fig. 2.8b). As TMPD concentrations are lowered while maintaining [TMPD$^+$] fixed, the apparent rate constant for NO· dissociation should increase (Eq. 2.8). Future studies of this type will help clarify the effect of NO· dissociation on the stopped-flow kinetics.

2.4.3. Summary

The stopped-flow results presented in this chapter revealed for the first time that reduction of nitrite-loaded ccNiR by the weak reductant TMPD generates a transient intermediate, assigned as the 1-electron reduced species $Fe_{H1}^{II}(NO_2^-)$. Generation of this species is pH-independent (Fig. 2.10a), whereas its decay to the previously characterized[2] 2-electron reduced intermediate $\{Fe_{H1}NO\}^7$ is fastest at pH 6.8, and significantly slower at higher pH (Fig. 2.10b). This is good evidence that the transient intermediate is indeed $Fe_{H1}^{II}(NO_2^-)$ and not $\{Fe_{H1}NO\}^6$; cleavage of the nitrite N – O bond is presumably the pH-dependent rate limiting step in the 1-electron reduction

of $Fe_{H1}^{II}(NO_2^-)$ to $\{Fe_{H1}NO\}^7$ (Scheme 2.5), as predicted by computational analysis.[18-19] Future experiment are planned by the Pacheco group that will further characterize the $Fe_{H1}^{II}(NO_2^-)$ and $\{Fe_{H1}NO\}^7$ species, putative catalytic intermediates in the ccNiR-catalyzed reduction of nitrite to ammonia, using spectroscopic techniques such as EPR and Mossbauer, and also time-resolved X-ray crystallography. The latter technique promises to shed light on the active site residues and waters that give rise to the pH-dependence seen in Fig. 2.10b.

Steady-state analysis of the ccNiR-catalyzed reduction of nitrite to NO· by TMPD showed that the rate is directly proportional to the concentration of $TMPD^+$ at low TMPD concentrations (Fig. 2.4a). This provides good evidence that the primary mechanism of NO· release is via the more labile $\{Fe_{H1}NO\}^6$ moiety (Scheme 2.4). However, a small amount of NO· release is observed even in the absence of $TMPD^+$, and at high concentrations of TMPD, where oxidation of $\{Fe_{H1}NO\}^7$ to $\{Fe_{H1}NO\}^6$ can't occur. This shows that $\{Fe_{H1}NO\}^7$ must release NO· as well, albeit very slowly. The steady-state studies also showed that nitrite is a substrate inhibitor of NO· release when TMPD is the electron source (Fig. 2.5), probably because it blocks facile egress of the NO· via the nitrite entry channel (Section 2.4.1.2). On the whole, ccNiR appears to be optimized to capture nitrite and minimize release of free NO·. Capture is achieved by reducing bound nitrite with even weak electron donors such as ferrocyanide and TMPD, and NO· release is minimized by stabilizing the comparatively substitutionally inert $\{Fe_{H1}NO\}^7$ over the more labile $\{Fe_{H1}NO\}^7$. Future experiments are planned that will quantify the dependence of NO· release on [TMPD] at fixed [$TMPD^+$] concentrations. Such experiments could deconvolute the parameters k_{1NO}/k_{red} and k_{ox} (Eq. 2.8 and Scheme 2.4), which in turn could aid in a more rigorous analysis of the Section 2.3.2 stopped-flow results.

2.5 References

1.   Ali, M. Probing the early steps in the catalytic reduction of nitrite to ammonia, catalyzed by cytochrome c nitrite reductase. University of Wisconsin-Milwaukee, Milwaukee, WI, 2019.

2.   Ali, M.; Stein, N.; Mao, Y.; Shahid, S.; Schmidt, M.; Bennett, B.; Pacheco, A. A., Trapping of a Putative Intermediate in the Cytochrome c Nitrite Reductase (ccNiR)-Catalyzed Reduction of Nitrite: Implications for the ccNiR Reaction Mechanism. *J Am Chem Soc* **2019,** *141* (34), 13358-13371.

3.   Youngblut, M.; Judd, E. T.; Srajer, V.; Sayyed, B.; Goelzer, T.; Elliott, S. J.; Schmidt, M.; Pacheco, A. A., Laue crystal structure of *Shewanella oneidensis* cytochrome c nitrite reductase from a high-yield expression system. *J Biol Inorg Chem* **2012,** *17* (4), 647-62.

4.   Berry, E. A.; Trumpower, B. L., Simultaneous determination of hemes a, b, and c from pyridine hemochrome spectra. *Anal Biochem* **1987,** *161* (1), 1-15.

5.   Barr, I.; Guo, F., Pyridine Hemochromagen Assay for Determining the Concentration of Heme in Purified Protein Solutions. *Bio Protoc* **2015,** *5* (18).

6.   Atkins, P.; Overton, T., *Shriver and Atkins' inorganic chemistry*. Oxford University Press, USA: 2010.

7.   Fultz, M. L.; Durst, R. A., Mediator compounds for the electrochemical study of biological redox systems: a compilation. *Analytica Chimica Acta* **1982,** *140* (1), 1-18.

8.   Stein, N.; Love, D.; Judd, E. T.; Elliott, S. J.; Bennett, B.; Pacheco, A. A., Correlations between the Electronic Properties of *Shewanella oneidensis* Cytochrome c Nitrite Reductase (ccNiR) and Its Structure: Effects of Heme Oxidation State and Active Site Ligation. *Biochemistry* **2015,** *54* (24), 3749-58.

9.   Koebke, K. J.; Pauly, D. J.; Lerner, L.; Liu, X.; Pacheco, A. A., Does the oxidation of nitric oxide by oxymyoglobin share an intermediate with the metmyoglobin-catalyzed isomerization of peroxynitrite? *Inorganic chemistry* **2013,** *52* (13), 7623-7632.

10.   Koebke, K. J.; Waletzko, M. T.; Pacheco, A. A., Direct Monitoring of the Reaction between Photochemically Generated Nitric Oxide and Mycobacterium tuberculosis Truncated Hemoglobin N Wild Type and Variant Forms: An Assessment of Computational Mechanistic Predictions. *Biochemistry* **2016,** *55* (4), 686-696.

11.   Chaka, G.; Bakac, A., Two-electron oxidation of N,N,N',N'-tetramethylphenylenediamine with a chromium(v) salen complex. *Dalton Trans* **2009,** (2), 318-21.

12.   Nematollahi, D.; Hosseinzadeh, S.; Dadpou, B., Comproportionation and Michael addition reactions of electrochemically generated N,N,N ',N '-tetramethyl-1,4-phenylenediamine dication. Synthesis of new unsymmetrical aryl sulfones containing N,N,N ',N '-tetramethyl-1,4-phenylenediamine moiety. *J Electroanal Chem* **2015,** *759*, 144-152.

13.   Press, W. H.; Teukolsky, S. A.; Vetterling, W. T.; Flannery, B. P., *Numerical recipes 3rd edition: The art of scientific computing*. Cambridge university press: 2007.

14.   Henry, E.; Hofrichter, J., [8] Singular value decomposition: Application to analysis of experimental data. In *Methods in enzymology*, Elsevier: 1992; Vol. 210, pp 129-192.

15.   Albrecht, A. C.; Simpson, W. T., Spectroscopic Study of Wurster's Blue and Tetramethyl-p-phenylenediamine with Assignments of Electronic Transitions1. *Journal of the American Chemical Society* **1955,** *77* (17), 4454-4461.

16.   Youngblut, M.; Pauly, D. J.; Stein, N.; Walters, D.; Conrad, J. A.; Moran, G. R.; Bennett, B.; Pacheco, A. A., *Shewanella oneidensis* cytochrome c nitrite reductase (ccNiR) does not

disproportionate hydroxylamine to ammonia and nitrite, despite a strongly favorable driving force. *Biochemistry* **2014,** *53* (13), 2136-44.

17.   McGarry, J. M.; Pacheco, A. A., Upon further analysis, neither cytochrome c 554 from Nitrosomonas europaea nor its F156A variant display NO reductase activity, though both proteins bind nitric oxide reversibly. *JBIC Journal of Biological Inorganic Chemistry* **2018,** *23* (6), 861-878.

18.   Bykov, D.; Neese, F., Substrate binding and activation in the active site of cytochrome c nitrite reductase: a density functional study. *J Biol Inorg Chem* **2011,** *16* (3), 417-30.

19.   Bykov, D.; Neese, F., Reductive activation of the heme iron–nitrosyl intermediate in the reaction mechanism of cytochrome c nitrite reductase: a theoretical study. *JBIC Journal of Biological Inorganic Chemistry* **2012,** *17* (5), 741-760.

20.   Bykov, D.; Neese, F., Six-electron reduction of nitrite to ammonia by cytochrome c nitrite reductase: insights from density functional theory studies. *Inorg Chem* **2015,** *54* (19), 9303-16.

21.   Bykov, D.; Plog, M.; Neese, F., Heme-bound nitroxyl, hydroxylamine, and ammonia ligands as intermediates in the reaction cycle of cytochrome c nitrite reductase: a theoretical study. *JBIC Journal of Biological Inorganic Chemistry* **2014,** *19* (1), 97-112.

22.   Einsle, O.; Messerschmidt, A.; Stach, P.; Bourenkov, G. P.; Bartunik, H. D.; Huber, R.; Kroneck, P. M., Structure of cytochrome c nitrite reductase. *Nature* **1999,** *400* (6743), 476-80.

23.   Einsle, O.; Messerschmidt, A.; Huber, R.; Kroneck, P. M.; Neese, F., Mechanism of the six-electron reduction of nitrite to ammonia by cytochrome c nitrite reductase. *J Am Chem Soc* **2002,** *124* (39), 11737-45.

24.   Bamford, V. A.; Angove, H. C.; Seward, H. E.; Thomson, A. J.; Cole, J. A.; Butt, J. N.; Hemmings, A. M.; Richardson, D. J., Structure and spectroscopy of the periplasmic cytochrome c nitrite reductase from Escherichia coli. *Biochemistry* **2002,** *41* (9), 2921-31.

Chapter 3

Expression, purification, and electrochemical characterization of the H257Q ccNiR variant

3.1. Overview

Shewanella oneidensis cytochrome *c* nitrite reductase (ccNiR), like other bacterial ccNiRs, contains three conserved active site amino acids, R103, Y206, and H257. These active site residues, along with a nearby Ca^{2+} ion, form a finely-tuned acidic environment for the negatively charged nitrite substrate. CcNiR crystal structures that contain nitrite or hydroxylamine bound at the active site clearly showed that the three conserved residues play crucial roles in correctly orienting the substrate for reduction events.[1] Furthermore, as summarized in Section 1.6.2 of the introduction, a series of computational studies suggest that the residues, particularly H257, are important in coupled proton-electron transfer steps during catalysis.[2-5] This chapter describes the expression, purification, and spectropotentiometric characterization of the H257Q variant of *S. oneidensis* ccNiR. The expression and purification of four *S. oneidensis* ccNiR variants, H257Q, R103Q, R103K, and Y206F, were carried out in collaboration with fellow Pacheco graduate student Steven Reinhardt. Chapter 4 describes kinetic experiments with H257Q and compares the variant's kinetic behavior to that of R103Q and Y206F, which are currently being investigated by Mr. Reinhardt and another Pacheco group graduate student, Shahama Alam.

3.2. Materials and Methods

3.2.1. General instrumentation and reagents

All reagents were of high bio-grade purity and purchased from Thermo-Fisher, Dot Scientific, or MP Biomedicals unless mentioned specifically. Routine UV−vis spectroscopy was performed using a CARY Bio 50 UV/Vis spectrophotometer.

3.2.2. Overexpression of the *S. oneidensis* H257Q ccNiR variant

3.2.2.1. Constructing active site variants of the ccNiR gene. The active site variants H257Q, Y206F, R103K, and R103Q were prepared in collaboration with Steven Reinhardt from our laboratory. All four variants were prepared from the same His-tagged variant with wild type active site, kindly provided by Mr. Reinhardt. As with previous ccNiR genes used in our laboratories, the ccNiR N-terminal signal sequence for periplasmic translocation in the parent variant was replaced by the signal sequence for *S. oneidensis* small tetraheme *c*,[6-7] which leads to improved ccNiR expression.[8] In addition, the modified parent gene also contained a TEV protease cleavage site (Glu-Asn-Leu-Tyr-Phe-Gln-Ser) and 10 histidine codons at the C-terminal.

The H257Q active site variant was prepared from the His-tagged parent variant as follows. The polymerase chain reaction (PCR) was performed using NEB Phusion High Fidelity DNA polymerase and the two sets of primers, forward: CTTAAAGCACAGCAACCTGAATACGAG, reverse: CATTGGGGTCTTACTAAGGGCATGG. These primers contained a 5´-phosphate to allow blunt-end ligation. The size of the PCR product was tested by running ethidium bromide (EtBr) containing 1% agarose gel electrophoresis (120 V, 60 min) and comparing it to a commercially available NEB Quick Load Purple 1 kb DNA ladder under UV light. A 4.2 kb band on the gel confirmed that the ccNiR-containing plasmid amplified correctly by PCR (Fig. A2.1).

The band containing the right sized plasmid was cut out with a sharp knife and cleaned using a gel cleaning kit (Qiagen) to obtain linear plasmid (30 μL according to the manufacturer's protocol). The instant sticky-end ligase master mix (5 μL, New England Biolabs) was used to ligate the linear plasmids (5 μL) and make them circular. The circular plasmid was then transformed into chemically competent NEB5-α cells (New England Biolabs) following the manufacturer's protocol. The transformation was confirmed by inoculating the bacterial culture overnight on LB and kanamycin (50 μg/mL) containing petri dishes at 37 °C. The bacterial colonies grown on the plate confirmed the positive transformation of plasmid DNA into the NEB 5-α cells. A few single colonies were picked and grown separately in mini culture (5 mL LB with 50 μg/mL kanamycin) to isolate the plasmid. This plasmid was used as a template for PCR using sequencing primers. The PCR products of the right size were again confirmed by gel electrophoresis, and after cleaning with the PCR clean-up kit (Qiagen), a sample of the PCR product was sent to the University of Chicago Comprehensive Cancer Center for sequencing. The newly sequenced plasmid was compared to the one containing wild type ccNiR by using ApE software (a free software suite for plasmid editing) to confirm the presence of the H257Q mutation.

3.2.2.2. Transformation of the mutant plasmid into *S. oneidensis* TSP-C cells. The plasmid containing the H257Q ccNiR gene was transferred to the TSP-C strain of *S. oneidensis* by electroporation. The TSP-C strain has a rifampicin resistance gene. TSP-C cells were grown overnight (~16 hours) at 30 °C with 30 μg/mL rifampicin. Approximately 2 mL of overnight culture were spun at $4300 \times g$ to obtain a cell pellet, washed with 500 μL 1 M sorbitol, decanted, and then resuspended in 80 μL 1M sorbitol. A 20 μL aliquot of mutant ccNiR plasmid was added to the resuspended cells, which were then electroporated at 1500 V, mixed with 800 μL of SOC growth medium, and incubated at 30 °C for 1-2 hours at 200 rpm in an incubator shaker. The newly

transformed cells were incubated overnight at 30 °C on a plate containing LB, kanamycin (50 µg/mL), and rifampicin (30 µg/mL). Only positively transformed bacteria grew on this plate, and they appeared as pink colonies. To doubly confirm the result, colony PCR was also performed, and the PCR products were loaded onto an EtBr-containing agarose gel. The presence of a new 1.5 kb band on the gel confirmed the presence of the bacterial plasmid that contained the variant (Fig. A2.2). After this confirmation, the bacterial colony from the petri dish was further cultured and then stored at –80 °C in 10% glycerol for future experiments.

3.2.3. Large scale purification of ccNiR active site variants from *S. oneidensis* TSP-C cells

3.2.3.1. Culture preparation and harvesting. A petri dish containing autoclaved LB agarose, and the antibiotics kanamycin (Kan, 50 µg/mL), and rifampicin (Rif, 30 µg/mL) was inoculated with *S. oneidensis* TSP-C cells containing the H257QccNiR gene and incubated overnight at 30°C. A single bacterial colony from the petri dish was suspended into 5mL LB (20 mg/mL), Kan (50 µg/mL), Rif (30 µg/mL) solution and was incubated for 10-11 hours in an incubator shaker at 200 rpm and 30 °C. After that period, 1 mL of bacterial culture was transferred into 1 L of the same medium, which was then incubated for 16 hours under the same conditions as in the first step. In a final step, 1 L of bacterial cell culture was transferred into a 50L carboy that already contained 45 L LB, Kan (50 µg/mL), Rif (30 µg/mL) thermostatted at 30 °C in a constant temperature water bath. The culture was incubated for 16 - 18 hours at 30 °C while being continually sparged with compressed air, which served to agitate the culture suspension and to keep it aerated until late in the growth process when high bacterial density consumed oxygen faster than it could be replenished. The cells were harvested from the 45 L cell culture by centrifuging aliquots in 1 L bottles for 10 minutes at $5,800 \times g$. The pooled cell pellets were resuspended using 20 mM tris buffer, pH = 8.1 (final volume ~500 mL), and either PMSF (0.1 - 1 mM) or AEBSF

(0.1 - 1.0 mM) was immediately added as a protease inhibitor. The resuspended pooled cell pellet was frozen and stored at −80 °C in a stainless steel beaker until needed.

3.2.3.2. Purification of H257Q ccNiR from *S. oneidensis* TSP-C cells. Concentrated suspensions of cells containing the H257Q ccNiR variant were lysed by sonication in an ice-cooled stainless steel beaker, using cycles of 30 s ultrasonic bursts at 70% amplitude followed by 45 s pauses, repeated for 10 minutes. The suspension was then centrifuged at $41,500 \times g$ for 60 minutes to remove cell debris, and the clarified supernatant was separated and loaded into an affinity column (GE Healthcare HisTrap FF, 20 mL). This column was pre-equilibrated with a buffer (Buffer A) that contained 40 mM Imidazole, 20 mM tris base, and 500 mM NaCl, adjusted to pH = 8.1. Determination of the optimal imidazole concentration in this buffer is described in A2.2, Fig. A2.3. The column was deemed to be equilibrated when the UV reading at 280 nm of the column flow-through was constant. After the clarified cell extract had been loaded, the column was washed with 5-10 column volumes of Buffer A until the UV reading at 280 nm of the column flow-through was once again constant. The his-tagged H257Q variant was eluted by mixing Buffer A with 80% of a pH 7.0 buffer containing 500 mM Imidazole, 20 mM HEPES, and 500 mM NaCl (Buffer B). All fractions for which the A280 deviated significantly from the baseline were pooled and immediately transferred to Snake-Skin dialysis tubes (9 mL /1 cm, ThermoFisher) for roughly 4 hours of dialysis at 4 °C in a low salt buffer reservoir (20 mM HEPES, 500 mM NaCl, pH = 7.0; Buffer C). The His-tag was removed by incubating the protein with tobacco etch virus (TEV) protease (purification protocol: A.2.1). TEV protease was added to the dialysis tube containing the H257Q variant according to the rule of thumb protocol of adding 1.0 O.D TEV protease to 10 O.D mutant ccNiR (TEV protease purification discussed in A2.3 and Fig A2.4). The dialysis tube was then transferred into another buffer reservoir (50 mM Tris, 100 mM NaCl, 1 mM DTT, 250 μM

EDTA, pH = 8.0; Buffer D) which was an optimum buffer for TEV protease activity. The digestion of His-tag by TEV protease was continued overnight at 4 °C. The digested protein solution was centrifuged at $41,500 \times g$ for 10 min and the supernatant was collected. A small HisTrap FF column (5 mL, GE Healthcare) was equilibrated with a buffer containing 25 mM tris, 300 mM NaCl, pH = 8.0 (Buffer E), after which the clarified protein solution was loaded onto it. This column captured undigested H257Q ccNiR and the TEV protease, which is also His-tagged, but allowed the H257Q ccNiR from which the His-tag had been successfully cleaved to pass through. The buffer from the flow-through was exchanged for a buffer containing 50 mM HEPES, 150 mM NaCl, pH = 7.0 (Buffer F), and then concentrated using centrifugal concentrators (Amicon) spun at 4,000 g for 10 min intervals. Size exclusion chromatography (SEC, Sephacryl-S200, GE Healthcare) was used as the final step of purification. The SEC column (320 mL) was equilibrated with Buffer F and then loaded with a concentrated H257QccNiR sample (not more than 2.5 mL). Two distinct UV280 peaks were observed in the chromatograph. The second of these displayed a UV/Vis ratio $A_{409}/A_{280} > 3.8$, and was confirmed to be the pure H257Q ccNiR by SDS-PAGE (Fig. A2.5). The pure protein's buffer was exchanged for 50 mM HEPES at pH = 7.0, after which the solution was concentrated using centrifugal concentrators and stored at –80 °C.

3.2.4. UV/Visible spectropotentiometric titrations of H257Q ccNiR

The H257QccNiR extinction coefficient spectrum was obtained in the wavelength range from 250 nm – 800 nm (Fig. 3.1) from the UV/Vis spectrum of a solution whose concentration had been established using the pyridine hemochromagen assay.[9] UV/Vis spectropotentiometry experiments were performed using a BASi Epsilon EC potentiostat to set the potential, and a CARY Bio 50 UV/Vis spectrophotometer to record the spectrum at each applied potential.
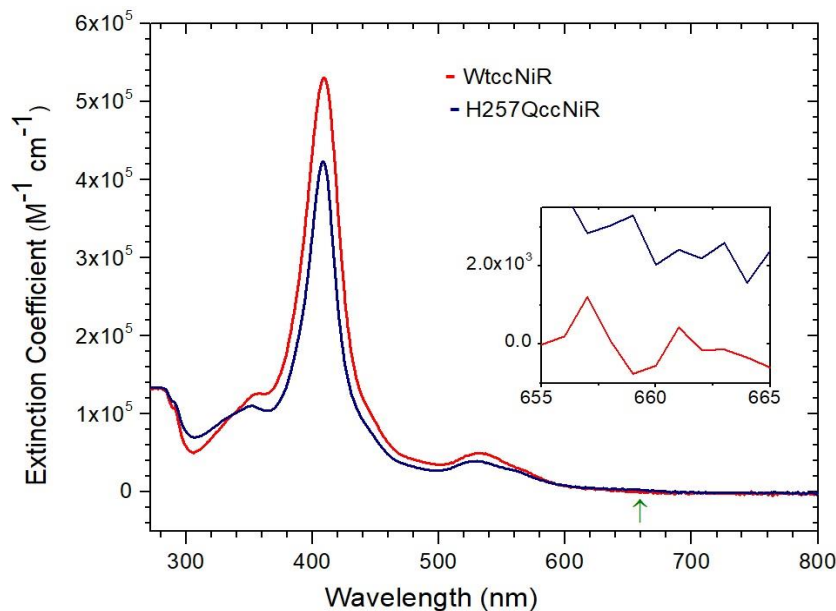
Figure 3.1. The extinction coefficient comparison of H257QccNiR (blue line) and wtccNiR (red line). Arrow (green) shows the location of the LMCT band that is present in the variant, but not the wild type spectrum, enlarged in inset (see main text for details).

The apparatus was housed in an anaerobic glove box. An Ag/AgCl electrode (BASi, model RE-5B) was used as a reference. The electrode was checked prior to collection of the spectropotentiometric data sets by using it to obtain cyclic voltammograms of methyl viologen, whose midpoint potential is known to be -0.449 V vs SHE.[10] An optically transparent thin-layer electrode (OTTLE) cell, of design previously used in our laboratory,[8] was used to do controlled potentiometric electrolysis on the H257Q variant. For the experiment, a solution containing H257Q ccNiR (70-90 μM protomer), the redox mediators listed in Table 3.1, 300 mM NaCl, and 5 mM nitrite, in a 50 mM HEPES buffer, pH 7.0, was loaded into the OTTLE cell. UV/visible

spectra in the range 360 nm − 620 nm were collected at 10 mV intervals between −40 mV and +200 mV vs SHE. The data sets were analyzed using programs written within the commercially available software package Mathcad 15 (PTC Software). Data analysis broadly followed the methodology used previously by this group,[8] with specifics described more fully in the Results section below.

Table 3.1. Mediators used for spectropotentiometric experiments

Mediator	$\varepsilon_{0.5}$ (V vs SHE)	Concentration (μM)
1,2-naphthoquinone-4-sulfonic acid	+ 0.168	100
Phenazine methosulfate	+ 0.08	25
Hexaammineruthenium (III) chloride	- 0.02	100

3.3. Results

3.3.1. UV/Vis spectrum of the H257Q ccNiR

Figure 3.1 shows the UV/Vis extinction coefficient spectrum of the H257Q ccNiR variant in comparison to the wild type spectrum. There are significant differences between the two spectra. Most notably, the Soret (409 nm) and 530 nm absorbance maxima are substantially weaker in the variant than in the wild type. On the other hand, just as in the *E. coli* homologs, the H257Q variant displays a band at 660 nm that the wild type does not (green arrow, Fig. 3.1).[11] Weak bands above 620 nm in *c*-hemes are assigned as ligand-to-metal charge transfer (LMCT) bands, which are seen in high-spin, but not low-spin hemes.[12] The position of these bands is sensitive to the heme coordination environment. In the case of *E. coli* ccNiR, the LMCT band was found at 630 nm in the wild type, and 660 nm in the His variant. This was ascribed to the fact that the wild type resting enzyme has water in the distal site, whereas the His variant is 5-coordinate.[11] The presence of the 660 nm band in the H257Q *S. oneidensis* variant suggests that it too has a vacant distal site in the

absence of substrate. The result demonstrates how strongly disrupted the active site's delicate hydrogen bonding network is in the variant.

3.3.2. Effect of nitrite on the electrochemical properties of *S. oneidensis* **H257Q ccNiR**

Figure 3.2a shows the UV/Vis spectral changes observed in the range from 360 nm to 620 nm, upon decreasing the applied potential from 200 mV to -40 mV (vs SHE), in a solution initially containing 89 μM H257QccNiR, 5 mM nitrite, the mediators listed in Table 3.1, and 300 mM NaCl, in a 50 mM pH 7.0 HEPES buffer. The difference spectra show maximal absorbance increases at 375 nm and decreases at 409 nm. These spectral changes are unlike those seen for wild type ccNiR reduction in either the presence or absence of nitrite.[13-14] In the presence of nitrite, wtccNiR displays maximal absorbance increases at 424 nm and 555 nm, and a maximal decrease at 402 nm.

$$C_{ox} + ne^- \longrightarrow C_{red}$$

$$\Delta A_{\lambda,\varepsilon_{app}} = \frac{\Delta A_{max(\lambda)} \cdot \exp\left[\dfrac{nF}{RT}(\varepsilon_m^0 - \varepsilon_{app})\right]}{1 + \exp\left[\dfrac{nF}{RT}(\varepsilon_m^0 - \varepsilon_{app})\right]}$$

Scheme 3.1. Nernst equation used to fit the Fig. 3.1 data. C_{ox} and C_{red} refer to fully oxidized ccNiR and reduced ccNiR by n number electron, respectively.

The Fig. 3.2a spectra were fit with a single Nernstian equation (Scheme 3.1). In the equation, $\Delta A_{\lambda,\varepsilon app}$ is the absorbance change observed at wavelength λ upon application of potential ε_{app}, ε_m^o is the midpoint potential associated with the reduction event, $\Delta A_{max(\lambda)}$ is the limiting absorbance change at wavelength λ observed at sufficiently low applied potentials, and n is the

number of electrons transferred in the Nernstian step. Functionally, ε_{app} and $\Delta A_{\lambda,\varepsilon app}$ are the independent and dependent variables, respectively, while $\varepsilon_m{}^o$ and $\Delta A_{(max)\lambda}$ are parameters obtained by nonlinear least-squares fitting of the Fig. 3.1 data set. The fitting process was performed twice, once with n fixed at 1 and the second time with n fixed at 2. In both cases, the midpoint potential was calculated as +87 mV from the least-squares fit.

Figure 3.2b shows an absorbance vs applied potential slice taken at 409 nm from the Fig. 3.2a spectra. The blue circles show the experimental data taken at 10 mV intervals, the solid red line is the least squares fit to the Scheme 3.1 equation obtained with n set to 1, while the dotted green line shows the fit with n set to 2. Though the data show a fair bit of scattering, the fit obtained with n set to 1 is clearly better than the one obtained with n set to 2.

3.4. Discussion

The spectroscopic and electrochemical behavior of the H257Q ccNiR variant upon reduction in the presence of nitrite differs substantially from that of the wild type enzyme. The Fig. 3.2a difference spectra show maximal absorbance increases at 375 nm and decreases at 409 nm. By contrast, reduction of wild type ccNiR results in maximal absorbance increases at 424 nm and decreases at 402 nm,[13,14] which is a more typical change upon low-spin c-heme reduction.[15-16] Notably, the characteristically sharp α,β bands at ~525 nm and ~550 nm that typically accompany low-spin c-heme reduction are absent in both Fig. 3.2a and in the difference spectra that accompany reduction of the nitrite-loaded wild type ccNiR. Figure 3.2a. instead displays a broad band with a maximum at ~570 nm, while a broad band grows in at 555 nm in the case of the wild type.[13]

The electrochemical behavior of H257Q ccNiR is also notably different from that of the wild type. While nitrite-loaded wild type ccNiR was reduced in a concerted 2-electron step to give

a $\{Fe_{H1}NO\}^7$ moiety,[13, 17] the UV/Vis spectropotentiometric results for the variant were clearly more consistent with a 1-electron reduction of the nitrite-loaded heme#1 center (Fig. 3.2b). The midpoint potential for nitrite-loaded H257Q ccNiR reduction was lower than that of the wild type, +87 mV compared to +240 mV vs SHE, but still significantly higher than the midpoint potential for wild type heme#1 reduction in the absence of nitrite. Without nitrite, wild type *S. oneidensis* ccNiR heme#1 has midpoint potentials of +20 mV vs SHE in the presence of the strong-field ligand cyanide, and −50 mV vs SHE when no strong-field ligand is present.[14]

Scheme 3.2 summarizes the species that could potentially be generated as the nitrite-loaded ccNiR active site is reduced under mild conditions. For the wild type, UV/Vis spectropotentiometric studies[18] showed that nitrite-loaded ferric ccNiR, $[Fe_{H1}^{III}(NO_2^-)]$, was reduced directly to $\{Fe_{H1}NO\}^7$, without accumulation of any 1-electron reduced intermediates. However, the stopped-flow studies of Chapter 2 showed that $[Fe_{H1}^{II}(NO_2^-)]$ does accumulate transiently in experiments with high concentrations of the reductant TMPD, then after a rate-limiting pH-dependent dehydration of the bound nitrite, is further reduced to the $\{Fe_{H1}NO\}^7$. The putative intermediate $\{Fe_{H1}NO\}^6$ is not detected. Fig. 3.2 shows that the H257Q variant is reduced by one, not two electrons, in UV/Vis spectropotentiometric experiments. However, the spectrum of the 1-electron reduced species does not match that of the $[Fe_{H1}^{II}(NO_2^-)]$ transient seen for the wild type in the stopped-flow experiments (Fig. 2.6, 2.7).
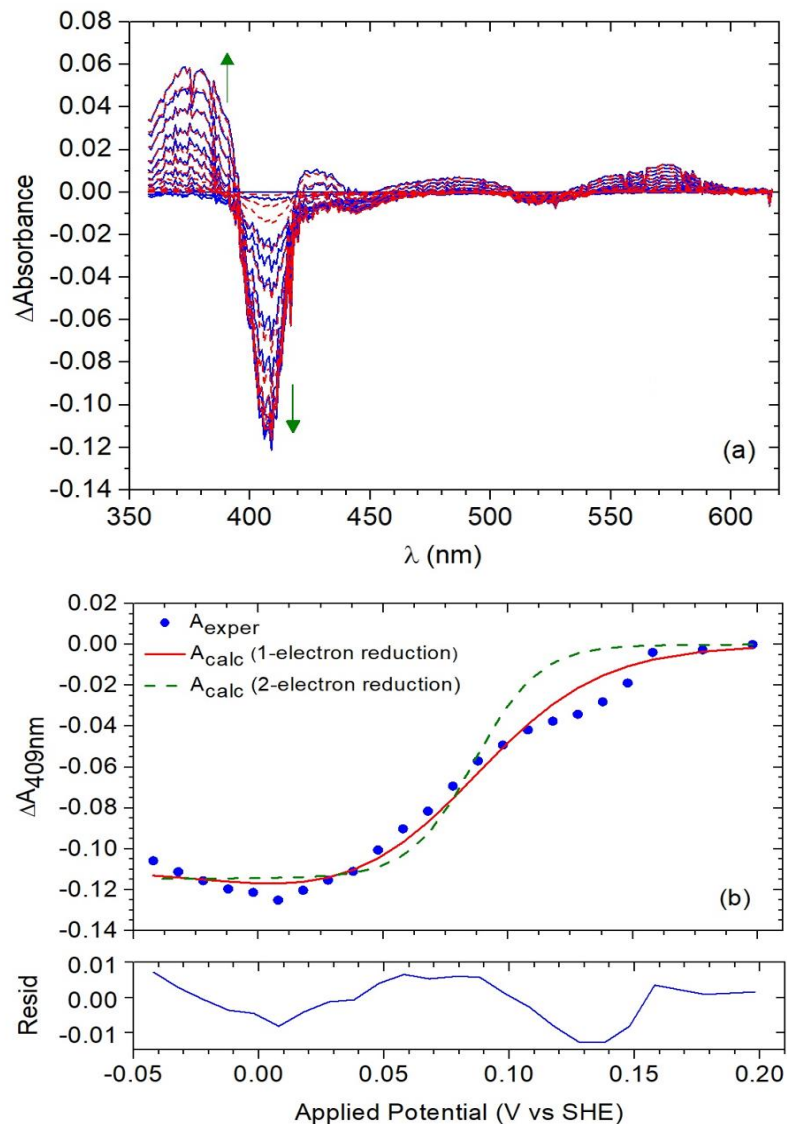
Figure 3.2.(a) UV/Vis spectral changes obtained upon exposing a solution initially containing 89 μM of fully oxidized H257QccNiR, 100 μM 1,2-naphthoquinone-4-sulfonic acid, 5 mM nitrite to progressively lower potentials. Solid blue lines show the experimentally obtained data, whereas the dashed red lines were calculated from least-squares fitting with a Nernstian 1-electron reduction and one spectral component (Scheme 3.1). The fit yields a midpoint potential of $\varepsilon_m^o = +0.087$ V vs SHE **(b)** Blue circles: an absorbance difference vs. applied potential slice taken at 409 nm from the spectra of part (a); solid red line: least-squares best fit obtained from a global analysis of the data with n fixed at 1 electron transferred in the Nernstian equation (Eq 3.1); dotted green line: same as the red line, but with n fixed at 2 electrons transferred in the Nernstian equation.

$$\{Fe_{H1}NO\}^6 = [Fe^{II}(NO^+) \longleftrightarrow Fe^{III}(NO^\cdot)]$$

$$\{Fe_{H1}NO\}^7 = [Fe^{II}(NO^\cdot) \longleftrightarrow Fe^{III}(NO^-)]$$
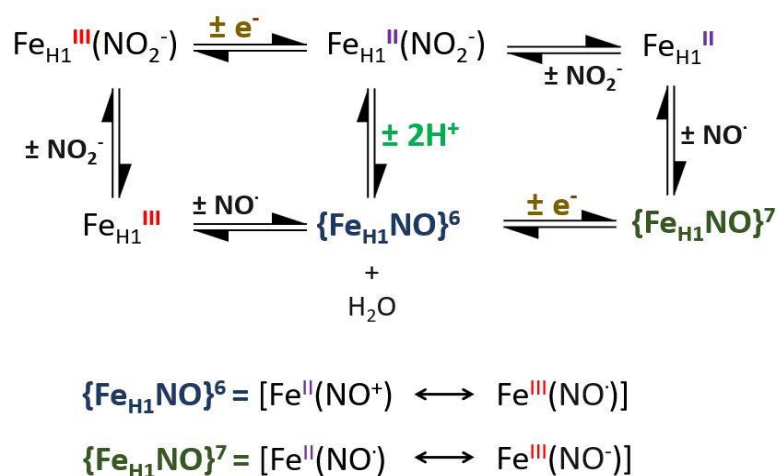
Scheme 3.2. The combined proposed mechanism is based on the 1 electron and two electrons reduction of H257QccNiR and wtccNiR, respectively. Previously reported by our group that under weak reducing agent nitrite reduction by wtccNiR release NO. Here, Fe_{H1} denotes the active site heme center in various states of oxidation and ligation.

An alternative possibility is that the 1-electron reduced species in Fig. 3.2 is an $\{Fe_{H1}NO\}^6$ moiety. However, such species tend to be labile, readily losing NO· and leaving behind a vacant Fe^{III} site that would subsequently re-bind nitrite. If that were the case, the H257Q ccNiR variant should be more effective than the wild type at catalyzing the 1-electron reduction of nitrite to NO·, yet the variant showed no such activity (Chapter 4). Another possibility is that, in the variant, nitrite binds the ferric site as a nitrito species (Chapter 1, Fig. 1.12), as has been proposed by Lockwood et al.[11] Distinguishing between these and other possibilities will require further experiments, such as EPR, Mossbauer or X-ray crystallography. However, the experiments described herein make some things clear. First, loss of H257 does not prevent the nitrite-loaded active site from reducing at a potential that is still substantially higher than the midpoint potential of the nitrite-free active site. It does, however, change the reduction product from a 2-electron to a 1-electron reduced moiety, which unlike typical $\{FeNO\}^6$ species,[19-20] does not appear to release

NO·. Judging from the UV/Vis differences seen between the wild type and H257Q variant (Fig. 3.1, Section 3.3.1), the change in redox behavior is almost certainly due to the disruption in the active site's hydrogen bonding network.

3.5. References

1.   Einsle, O.; Messerschmidt, A.; Huber, R.; Kroneck, P. M.; Neese, F., Mechanism of the six-electron reduction of nitrite to ammonia by cytochrome c nitrite reductase. *J Am Chem Soc* **2002,** *124* (39), 11737-45.

2.   Bykov, D.; Neese, F., Substrate binding and activation in the active site of cytochrome c nitrite reductase: a density functional study. *J Biol Inorg Chem* **2011,** *16* (3), 417-30.

3.   Bykov, D.; Neese, F., Reductive activation of the heme iron-nitrosyl intermediate in the reaction mechanism of cytochrome c nitrite reductase: a theoretical study. *J Biol Inorg Chem* **2012,** *17* (5), 741-60.

4.   Bykov, D.; Plog, M.; Neese, F., Heme-bound nitroxyl, hydroxylamine, and ammonia ligands as intermediates in the reaction cycle of cytochrome c nitrite reductase: a theoretical study. *J Biol Inorg Chem* **2014,** *19* (1), 97-112.

5.   Bykov, D.; Neese, F., Six-electron reduction of nitrite to ammonia by cytochrome c nitrite reductase: insights from density functional theory studies. *Inorg Chem* **2015,** *54* (19), 9303-16.

6.   Tsapin, A.; Nealson, K.; Meyers, T.; Cusanovich, M.; Van Beuumen, J.; Crosby, L.; Feinberg, B.; Zhang, C., Purification and properties of a low-redox-potential tetraheme cytochrome c3 from Shewanella putrefaciens. *Journal of bacteriology* **1996,** *178* (21), 6386-6388.

7.   Takayama, Y.; Akutsu, H., Expression in periplasmic space of Shewanella oneidensis. *Protein Expr Purif* **2007,** *56* (1), 80-4.

8.   Youngblut, M.; Judd, E. T.; Srajer, V.; Sayyed, B.; Goelzer, T.; Elliott, S. J.; Schmidt, M.; Pacheco, A. A., Laue crystal structure of *Shewanella oneidensis* cytochrome c nitrite reductase from a high-yield expression system. *J Biol Inorg Chem* **2012,** *17* (4), 647-62.

9.   Berry, E. A.; Trumpower, B. L., Simultaneous determination of hemes a, b, and c from pyridine hemochrome spectra. *Anal Biochem* **1987,** *161* (1), 1-15.

10.   Watanabe, T. H., K.,, Measurement of the extinction coefficient of the methyl viologen cation radical and the efficiency of its formation by semiconductor photocatalysis. *J. Phys. Chem.* **1982,** *86,* , 2617-2619.

11.   Lockwood, C. W.; Burlat, B.; Cheesman, M. R.; Kern, M.; Simon, J.; Clarke, T. A.; Richardson, D. J.; Butt, J. N., Resolution of key roles for the distal pocket histidine in cytochrome C nitrite reductases. *J Am Chem Soc* **2015,** *137* (8), 3059-68.

12.   Cheesman, M. R.; Watmough, N. J.; Gennis, R. B.; Greenwood, C.; Thomson, A. J., Magnetic-circular-dichroism studies of Escherichia coli cytochrome bo. Identification of high-spin ferric, low-spin ferric and ferryl [Fe(IV)] forms of heme o. *Eur J Biochem* **1994,** *219* (1-2), 595-602.

13.   Ali, M.; Stein, N.; Mao, Y.; Shahid, S.; Schmidt, M.; Bennett, B.; Pacheco, A. A., Trapping of a Putative Intermediate in the Cytochrome c Nitrite Reductase (ccNiR)-Catalyzed Reduction of Nitrite: Implications for the ccNiR Reaction Mechanism. *J Am Chem Soc* **2019,** *141* (34), 13358-13371.

14.   Stein, N.; Love, D.; Judd, E. T.; Elliott, S. J.; Bennett, B.; Pacheco, A. A., Correlations between the Electronic Properties of *Shewanella oneidensis* Cytochrome c Nitrite Reductase (ccNiR) and Its Structure: Effects of Heme Oxidation State and Active Site Ligation. *Biochemistry* **2015,** *54* (24), 3749-58.

15.   Arciero, D. M.; Balny, C.; Hooper, A. B., Spectroscopic and rapid kinetic studies of reduction of cytochrome c554 by hydroxylamine oxidoreductase from Nitrosomonas europaea. *Biochemistry* **1991,** *30* (48), 11466-72.

16.   Marritt, S. J.; Kemp, G. L.; Xiaoe, L.; Durrant, J. R.; Cheesman, M. R.; Butt, J. N., Spectroelectrochemical Characterization of a Pentaheme Cytochrome in Solution and as Electrocatalytically Active Films on Nanocrystalline Metal-Oxide Electrodes. *Journal of the American Chemical Society* **2008,** *130* (27), 8588-8589.

17.   Enemark, J. H.; Feltham, R. D., Principles of structure, bonding, and reactivity for metal nitrosyl complexes. *Coordination Chemistry Reviews* **1974,** *13* (4), 339-406.

18.   Ali, M. Probing the early steps in the catalytic reduction of nitrite to ammonia, catalyzed by cytochrome c nitrite reductase. University of Wisconsin-Milwaukee, Milwaukee, WI, 2019.

19.   Praneeth, V.; Paulat, F.; Berto, T. C.; George, S. D.; Näther, C.; Sulok, C. D.; Lehnert, N., Electronic Structure of Six-Coordinate Iron (III)− Porphyrin NO Adducts: The Elusive Iron (III)−NO (radical) State and Its Influence on the Properties of These Complexes. *Journal of the American Chemical Society* **2008,** *130* (46), 15288-15303.

20.   Hunt, A. P.; Lehnert, N., Heme-nitrosyls: electronic structure implications for function in biology. *Accounts of chemical research* **2015,** *48* (7), 2117-2125.

Chapter 4

A Mechanistic Study of CcNiR Catalyzed Reduction of Nitrite and Hydroxylamine: Determine the Primary Roles of Active Site Amino Acids by Steady-state Kinetics Experiments

4.1. Overview

Nitrite is considered to be the physiological substrate for ccNiR (Fig. 4.1), and in the standard assay with methyl viologen monocation radical (MV_{red}) as electron donor, it is reduced to ammonium in a six electron, eight proton process that releases no intermediates (Scheme 4.1.a). To complete the reaction, two nitrogen-oxygen bonds need to be cleaved and two oxygens need to be replaced by four protons. Though no intermediates have ever been detected in the standard assay, hydroxylamine is believed to be transiently generated because it is an alternative substrate for ccNiR in the assay (Scheme 4.1b).[1] Furthermore, for the *W. succinogenes* enzyme, a crystal structure of ccNiR with hydroxylamine bound to the active site was reported.[2]

As mentioned in Chapter 3, four *S. oneidensis* ccNiR variants, H257Q, R103Q, R103K, and Y206F have been prepared in collaboration with fellow Pacheco graduate student Steven Reinhardt to assess the roles that these active site amino acids play in proton delivery. In this chapter, the primary roles of R103 and H257 are examined by subjecting the variants R103Q and H257Q to the standard assay in which MV_{red} is the electron donor. The values of k_{cat} and K_m were determined for both the nitrite and hydroxylamine substrates and compared to those of the wild type enzyme.
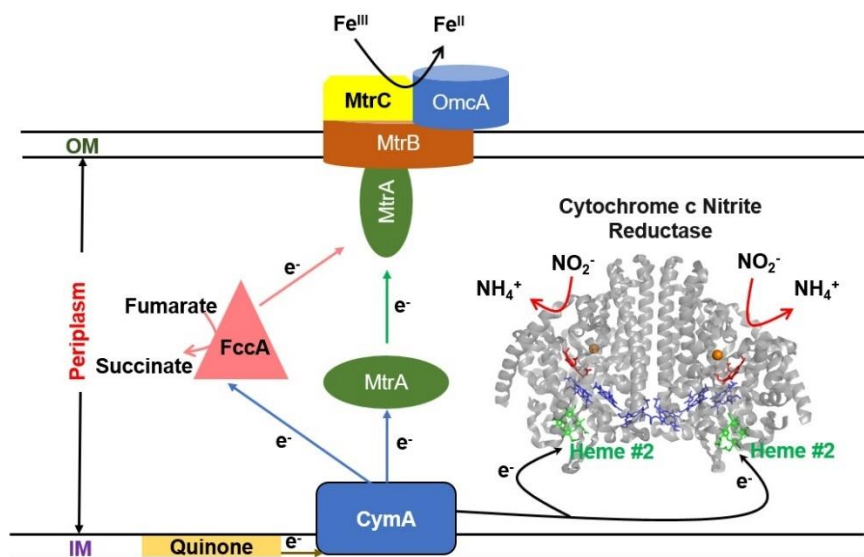
Figure 4.1. Inner membrane electron transport **Cy**toplasmic **m**embrane protein **A** (CymA) acts as a physiological electron donating partner to various proteins (ccNiR, FccA, and MtrA) in *S. oneidensis* (γ-proteobacterium). CymA acts as electron branching point and supplies electrons to ccNiR which reduces nitrite to ammonium, FccA which reduces fumarate to succinate and MtrA which ultimately reduces extracellular metal oxides. **IM:** Inner membrane, **OM:** Outer membrane.
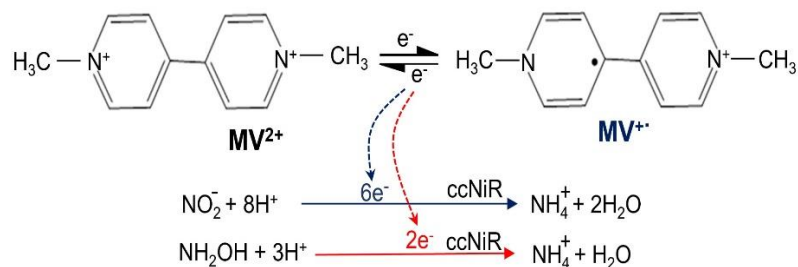
Scheme 4.1. Methyl viologen accepts an electron to produce MV_{red} ($MV^{+\bullet}$), a powerful reductant. The re-oxidation of MV_{red} provides electrons to the ccNiR to reduce to reduce substrates, **(a)** nitrite, and **(b)** hydroxylamine. The nitrite reduction requires six electrons and eight protons, the hydroxylamine one two electrons and three protons.

4.2. Materials and Methods

4.2.1. General materials

Sodium nitrite, hydroxylamine hydrochloride, potassium ferrocyanide (II) trihydrate, Tris-HCl (99% extra pure), and BisTris (ultra-pure) were purchased from Acros Organics; Ammonium sulfate (AS), EDTA and HEPES free acid and sodium salt were obtained from fisher scientific, Argon (high purity grade) from Airgas. Wild type *S. oneidensis* ccNiR and mutant ccNiRs were purified as described in Chapter 2.2 and Chapter 3.2 respectively.

### 4.2.2. General instrumentation

Cary 50 (Varian) spectrophotometers were used to record the UV/vis spectral data. Two of these spectrophotometers are housed in gloveboxes. Two gloveboxes (MBraun and Innovative Technology) were used to maintain anaerobic conditions while recording UV/vis spectra or doing controlled potential electrolysis. The gloveboxes are filled with high purity nitrogen (Airgas, 99.99 % pure), which is continually circulated through an oxygen scrubber to maintain an oxygen level of less than 2 ppm. The glovebox scrubbers were regenerated with 5% or 7% Hydrogen (Airgas) at least once a month, or whenever the oxygen level rose above 2 ppm. BASi Epsilon EC potentiostats were used to measure spectropotentiometric data and to reduce required reagents at the appropriate potentials. An Ag/AgCl electrode (BASi model RE-5B) was used as the reference, and routinely calibrated against the methyl viologen midpoint potential as described in Section 3.2.4. The pyridine hemochromagen assay[3] was used to obtain extinction coefficient spectra for all ccNiR variants, as described in Section 2.2.4.

4.2.3. Steady-state kinetics of ccNiR-catalyzed nitrite and hydroxylamine reduction by methyl viologen monocation radical

Kinetic experiments were carried out in one of the two gloveboxes; buffers were degassed by purging them with argon on a Schlenk line prior to being brought into the gloveboxes. The ability of wild type ccNiR and its variants to catalyze nitrite and hydroxylamine reduction by MV_{red} was measured at varying substrate concentrations to obtain the standard kinetic parameters, k_{cat}, K_m (Eqs. 4.2, 4.3).[4-5] The MV_{red} ($\varepsilon_m° = -0.449$ V vs SHE) was generated by applying a -700 mV vs SHE potential to the oxidized moiety. A large set of steady-state reactions was observed after mixing 100 μM MV_{red}, and varying substrate concentration (nitrite $\approx$ 2 μM – 3 mM or hydroxylamine $\approx$ 0.5 – 250 mM) at pH = 7.0. All the reactions were performed in two sets, one in the presence of enzyme (wtccNiR $\approx$ 100 pM, H257QccNiR $\approx$ 100 nM, R103QccNiR $\approx$ 100 nM) and one without enzyme (blank reaction). MV_{red} reacts with nitrite and hydroxylamine even in the the absence of ccNiR; the uncatalyzed contribution was measured in the blank experiments, and subtracted. MV_{red} oxidation was monitored by UV/Vis spectroscopy in the range from 500 nm-700 nm; spectra were collected at 15 s intervals for 3 – 5 minutes. MV_{red} exists as a mixture of monomer and dimer in proportions that vary with total MV_{red} concentration, and monitoring the 500 nm-700 nm visible range allowed the contributions from each species to be distinguished. In the kinetic experiments, the rate of change in total MV_{red} is reported, where $(MV_{red})_{tot} = MV_{red}+2(MV_{red})_2$.

Nitrite-dependence studies were carried out in 50 mM HEPES for the pH 7 experiments, and in 50 mM Tris for the pH 8 experiments. The K_m value for ccNiR-catalyzed reduction of hydroxylamine by MV_{red} is in the mM range, and at such high concentrations the hydroxylamine (pK_a 6.03) becomes part of the buffer system. Therefore, for hydroxylamine reduction

experiments, solutions were prepared by a method first developed by Youngblut et al,[5] and illustrated in Fig. 4.2. Aliquots of hydroxylamine hydrochloride and NaHEPES stock solutions were mixed in 1:1.2 mole ratios to give final solutions containing the desired hydroxylamine concentration. Varying amounts of sodium chloride were also added to the solutions to maintain the ionic strength constant at 0.3 M. As seen in Fig. 4.2, the pHs of solutions prepared in this way were close to 7.0 for a wide range of hydroxylamine concentrations.

$$E + S \xrightleftharpoons[k_{-1}]{k_1} ES \xrightarrow{k_{cat}} E + S \quad \text{------------} \quad (4.1)$$
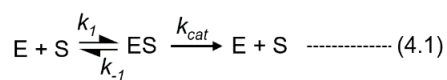
$$V = \frac{k_{cat}[E][S]}{K_m + [S]} \quad \text{----------------------} \quad (4.2)$$

$$V = \frac{V_{max}[S]}{K_m + [S]} \quad \text{----------------------} \quad (4.3)$$

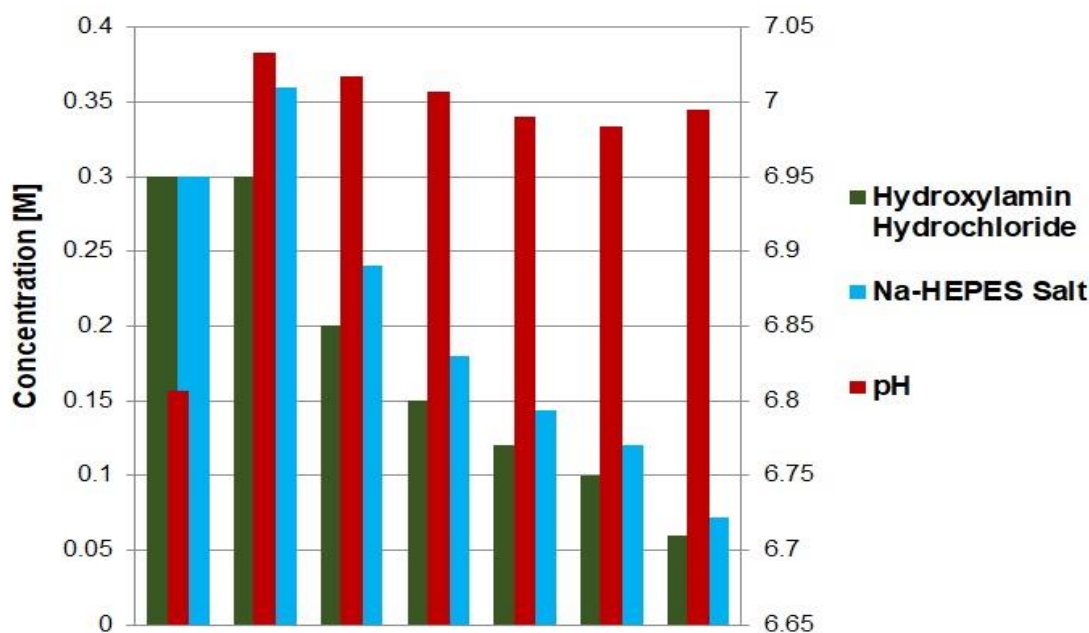$$K_m = [S] \text{ when, } V = V_{max}/2 \quad \text{--------------} \quad (4.4)$$

Figure 4.2. Determining the ratio of hydroxylamine hydrochloride (blue) and Na-HEPES (green) needed to maintain the pH constant at 7.0 in the reaction media. The left-hand *y-axis* scale shows the concentrations of hydroxylamine hydrochloride and Na-HEPES, and the right-hand *y-axis* shows the corresponding pH (red).

4.4. Results

4.4.1. WtccNiR-catalyzed nitrite reduction by methyl viologen monocation radical at varying pH

Figures 4.3 and 4.4 show how the initial rates of wtccNiR-catalyzed nitrite reduction by MV_{red} varied with nitrite concentration at pH 7 and pH 8, respectively. In both cases the experimental data were fit with the Michaelis-Menten equation (Eqs. 4.2 and 4.3). The value of K_m was found to be essentially invariant with pH, $(2.6 \pm 0.3) \times 10^{-5}$ M at pH 7 and $(2.0 \pm 0.4) \times 10^{-5}$ M at pH 8, while the value of k_{cat} decreased modestly from 4700 ± 90 s^{-1} at pH 7 to 3250 ± 100 s^{-1} at pH 8.

Figure 4.3. WtccNiR-catalyzed reduction of nitrite by MV_{red} at varying nitrite concentrations. Blue circles are the experimentally obtained values at each nitrite concentration, while the red curve is the least-squares fit of the data to the rectangular hyperbola Eq 4.2, 4.3, 4.4. This set of experiments was performed at pH 7.0 in the presence of 54 pM wtccNiR and 100 μM MV_{red}. The least-squares fit yielded the parameter values $K_m = (2.6 \pm 0.3) \times 10^{-5}$ M and $k_{cat} = 4700 \pm 90$ s^{-1}.
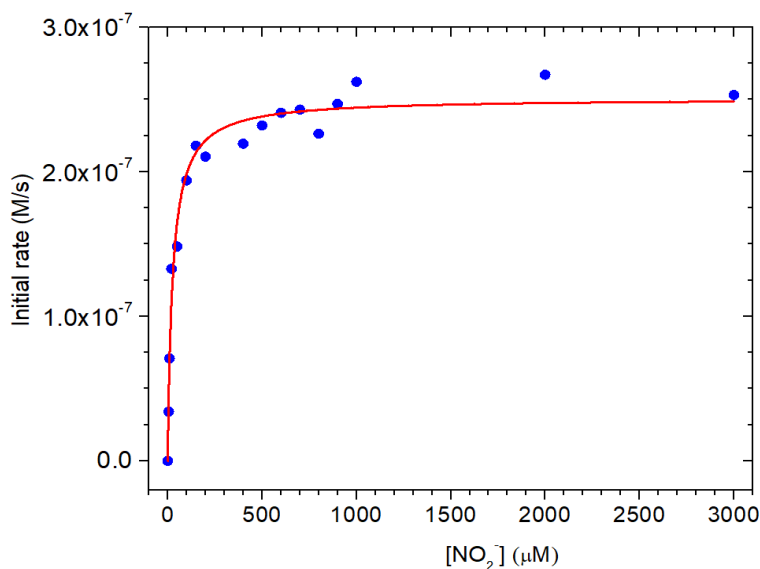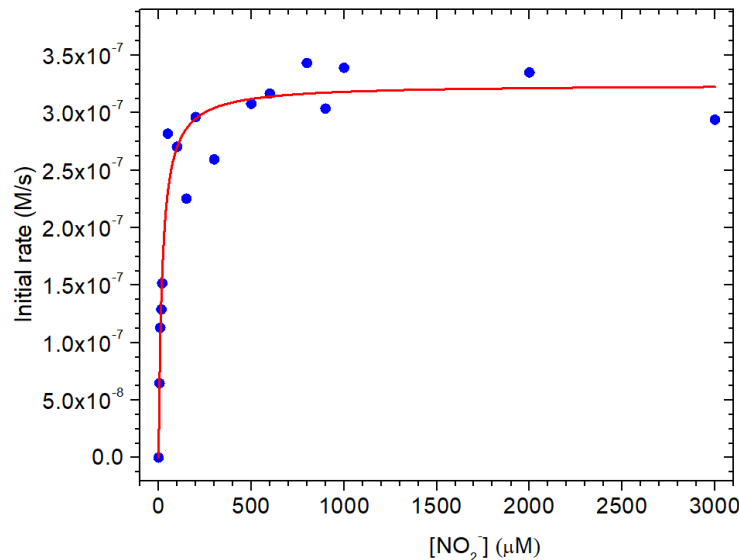
Figure 4.4. WtccNiR-catalyzed reduction of nitrite by MV_{red} at varying nitrite concentrations. Blue circles are the experimentally obtained values at each nitrite concentration, while the red curve is the least-squares fit of the data to the rectangular hyperbola Eq 4.2, 4.3, 4.4. This set of experiments was performed at pH 8.0 in the presence of approximately 100 pM wtccNiR and 100 μM MV_{red}. The least-squares fit yielded the parameter values $K_m = (2.0 \pm 0.4) \times 10^{-5}$ M and $k_{cat} = 3250 \pm 100$ s^{-1}.

Figure 4.5. H257QccNiR-catalyzed reduction of nitrite by MV_{red} at varying nitrite concentrations. Blue circles are the experimentally obtained values at each nitrite concentration, while the red curve is the least-squares fit of the data to the rectangular hyperbola Eq 4.2, 4.3, 4.4. This set of experiments was performed at pH 7.0 in the presence of approximately 7.7 nM H257QccNiR and 100 μM MV_{red}. The least-squares fit yielded the parameter values $K_m = (1.50 \pm 0.34) \times 10^{-4}$ M and $k_{cat} = 11.3 \pm 0.6$ s^{-1}.
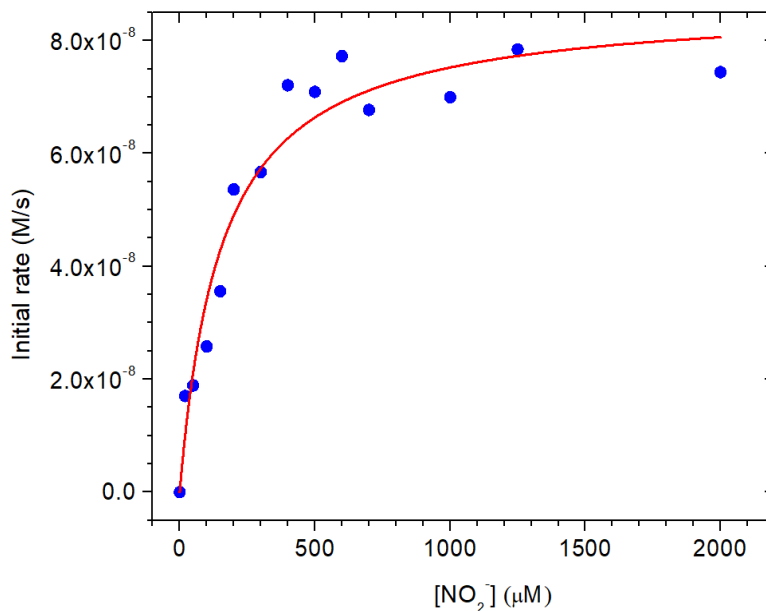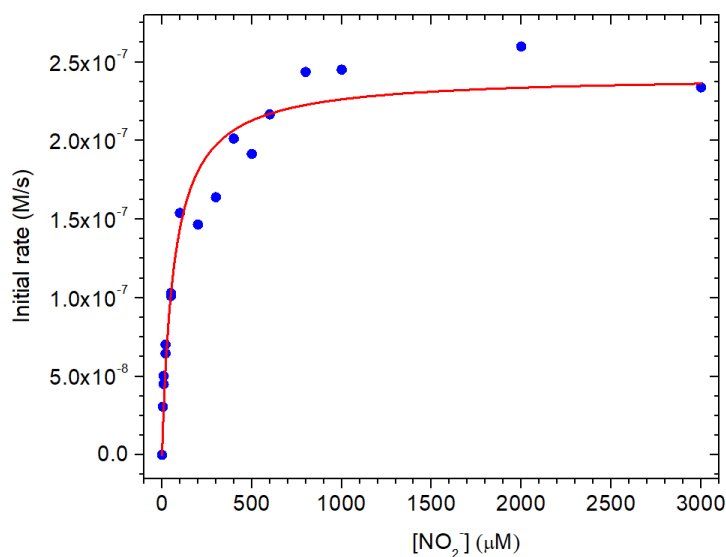
124

Figure 4.6. H257QccNiR-catalyzed reduction of nitrite by MV$_{red}$ at varying nitrite concentrations. Blue circles are the experimentally obtained values at each nitrite concentration, while the red curve is the least-squares fit of the data to the rectangular hyperbola Eq 4.2, 4.3, 4.4. This set of experiments was performed at pH 8.0 in the presence of approximately 100 nM H257QccNiR and 100 μM MV$_{red}$. The least-squares fit yielded the parameter values K_m = (6.8 ± 1.2)×10^{-5} M and k_{cat} = 2.4 ± 0.1 s^{-1}.

Table 4.1. Summary of k_{cat} values for WT and H257Q ccNiR-catalyzed reduction of nitrite by MV$_{red}$ at pH 7.0 and 8

Enzyme	k_{cat} (s^{-1}) at pH=7.0	k_{cat} (s^{-1}) at pH=8.0	k_{cat} change (pH 7.0 to 8.0)*
wtccNiR	4666 ± 90	3250 ± 100	- 30%
H257QccNiR	11.27 ± 0.6	2.42 ± 0.09	- 80%

*This is approximate value, negative (-) sign indicates activity decrease

4.4.2. H257QccNiR-catalyzed nitrite reduction by methyl viologen monocation radical at varying pH

The H257Q variant was found to be much less active than wtccNiR. However, plots of initial MV$_{red}$ oxidation rate vs H257QccNiR concentration at fixed MV$_{red}$ and nitrite concentrations were linear, confirming that the variant was still capable of catalyzing nitrite reduction by MV$_{red}$. Experiments analogous to those of Section 4.4.1 were conducted with H257QccNiR at pH 7.0 and pH 8.0. The results, shown in Figs. 4.5 and 4.6, were once again fit with the Michaelis Menten equation. The value of K_m was almost six-fold higher in H257QccNiR

than in the wild type, $(1.50 \pm 0.34) \times 10^{-4}$ M compared to $(2.6 \pm 0.3) \times 10^{-5}$ M at pH 7 (Fig. 4.5), though somewhat surprisingly, it was lower at pH 8, $(6.8 \pm 1.2) \times 10^{-5}$ M (Fig. 4.6). The biggest change from the wild type was seen in k_{cat}. At pH 7 this parameter decreased from 4700 ± 90 s^{-1} for the wild type to 11.3 ± 0.6 s^{-1} (Fig. 4.5), while at pH 8 it decreased from 3250 ± 100 s^{-1} to 2.4 ± 0.1 s^{-1} (Fig. 4.6). As the reaction rate was so slow when using H257QccNiR, much higher enzyme concentrations were required for experiments (10 nM – 100 nM compared to 50 pM – 100 pM of wild type).

4.4.3. WtccNiR- and H257QccNiR-catalyzed hydroxylamine reduction by methyl viologen monocation radical

Figures 4.7 and 4.8 show how the initial rates of wtccNiR- and H257Q-catalyzed hydroxylamine reduction by MV$_{red}$ varied with hydroxylamine concentration at pH 7. Figure 4.9 shows similar results obtained with the R103QccNiR variant, in collaboration with coworker Shahama Alam. Interestingly, the k_{cat} values for the wild type and H257Q variants were comparable when the substrate was hydroxylamine: 3110 ± 325 s^{-1} (Fig. 4.7) and 2050 ± 140 s^{-1} (Fig. 4.9), respectively. This is in contrast to the 1000× decrease observed in the variant k_{cat} when nitrite was the substrate (Sections 4.4.1 and 4.4.2 above). The R103QccNiR did display a significantly lower k_{cat} value, 570 ± 65 s^{-1}, when hydroxylamine was the substrate.

The K_m values obtained when hydroxylamine was the substrate were all in the millimolar range, which is much higher than the values obtained when nitrite was the substrate. However, the values were not significantly different in the three variants investigated: $(20 \pm 7) \times 10^{-3}$ M for wtccNiR (Fig. 4.7), $(20 \pm 5) \times 10^{-3}$ M for H257QccNiR (Fig 4.8), and $(27 \pm 6) \times 10^{-3}$ M for R103Q (Fig. 4.9), respectively.
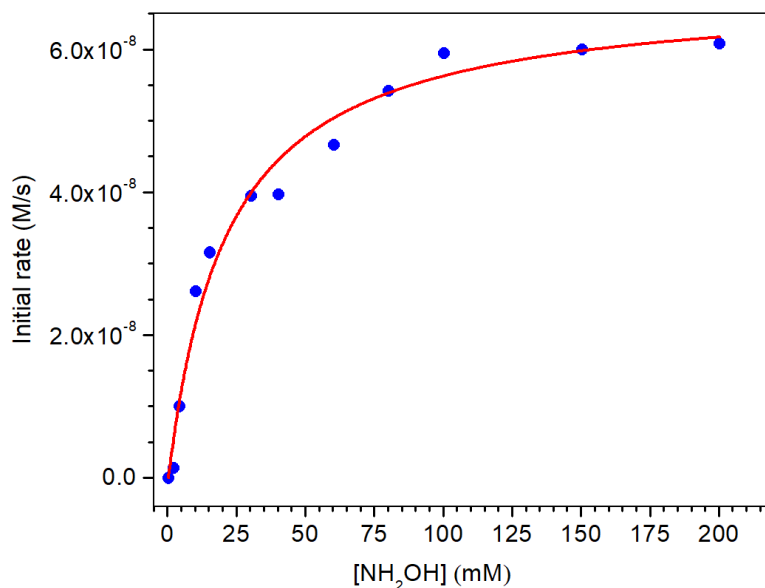
Figure 4.7. The reaction rate of wtccNiR dependence on hydroxylamine concentration. Blue circles are the experimentally obtained values at each nitrite concentration, while the red curve is the least-squares fit of the data to the rectangular hyperbola Eq 4.2, 4.3, 4.4. This set of experiments was performed at pH 7.0 in the presence of approximately 100 nM ccNiR, 100 uM methyl viologen and varying nitrite concentration. The least-squares fit yielded the parameter values $K_m = (21.3 \pm 0.6) \times 10^{-3}$ M and $k_{cat} = 3100 \pm 300$ s^{-1}.

4.5. Discussion

4.5.1. Role of H257 in cleavage of the first nitrite N-O bond

Tables 4.1 and 4.2 summarize the kinetic parameters obtained for wild type and variant ccNiR-catalyzed nitrite and hydroxylamine reduction by MV$_{red}$. By far the biggest loss of activity is seen in the H257Q variant's ability to catalyze nitrite reduction. Importantly, H257Q's ability to catalyze hydroxylamine reduction was not similarly affected, which demonstrates that H257 plays an essential role in cleaving the first nitrite N-O bond, but isn't as critical for cleaving the second. As summarized in Section 1.6.2, two N-O bonds need to be cleaved to form ammonia from nitrite, and these N-O bond cleavages rely on carefully choreographed transfers of six electrons and eight protons to the nitrogen moiety.
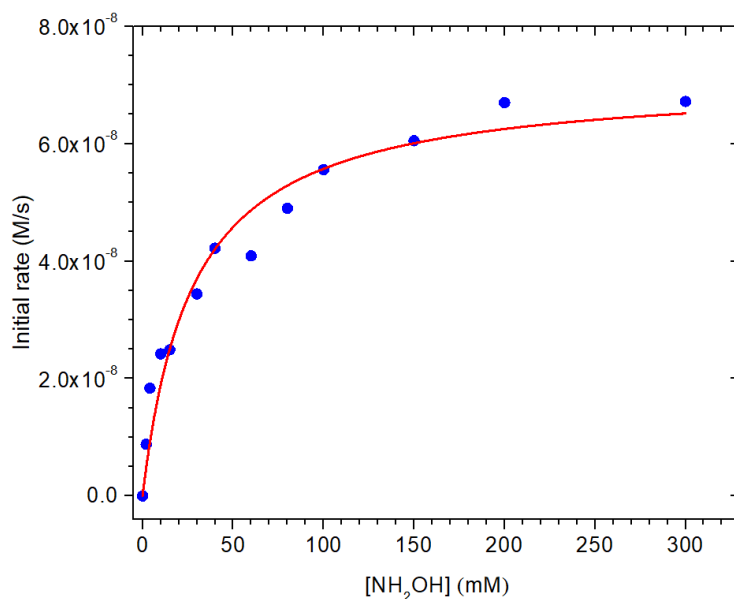
127

Figure 4.8. The reaction rate of R103QccNiR dependence on hydroxylamine concentration. Blue circles are the experimentally obtained values at each nitrite concentration, while the red curve is the least-squares fit of the data to the rectangular hyperbola Eq 4.2, 4.3, 4.4. This set of experiments was performed at pH 7.0 in the presence of approximately 118 pM R103QccNiR, 100 uM methyl viologen and varying nitrite concentration. The least-squares fit yielded the parameter values $K_m = (27.7 \pm 6) \times 10^{-3}$ M and $k_{cat} = 602 \pm 28$ s^{-1}.

Figure 4.9. The reaction rate of H257QccNiR dependence on hydroxylamine concentration. Blue circles are the experimentally obtained values at each nitrite concentration, while the red curve is the least-squares fit of the data to the rectangular hyperbola Eq 4.2, 4.3, 4.4. This set of experiments was performed at pH 7.0 in the presence of approximately 33 pM H257QccNiR, 100 uM methyl viologen and varying nitrite concentration. The least-squares fit yielded the parameter values $K_m = (21 \pm 5) \times 10^{-3}$ M and $k_{cat} = 2050 \pm 140$ s^{-1}
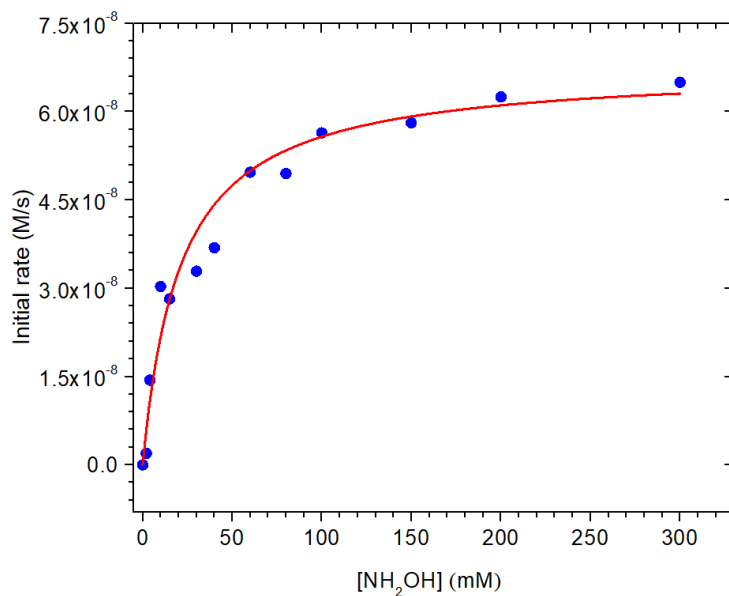
Table 4.2. Nitrite and hydroxylamine titration by wtccNiR, R103QccNiR and H257QccNiR at pH=7.0

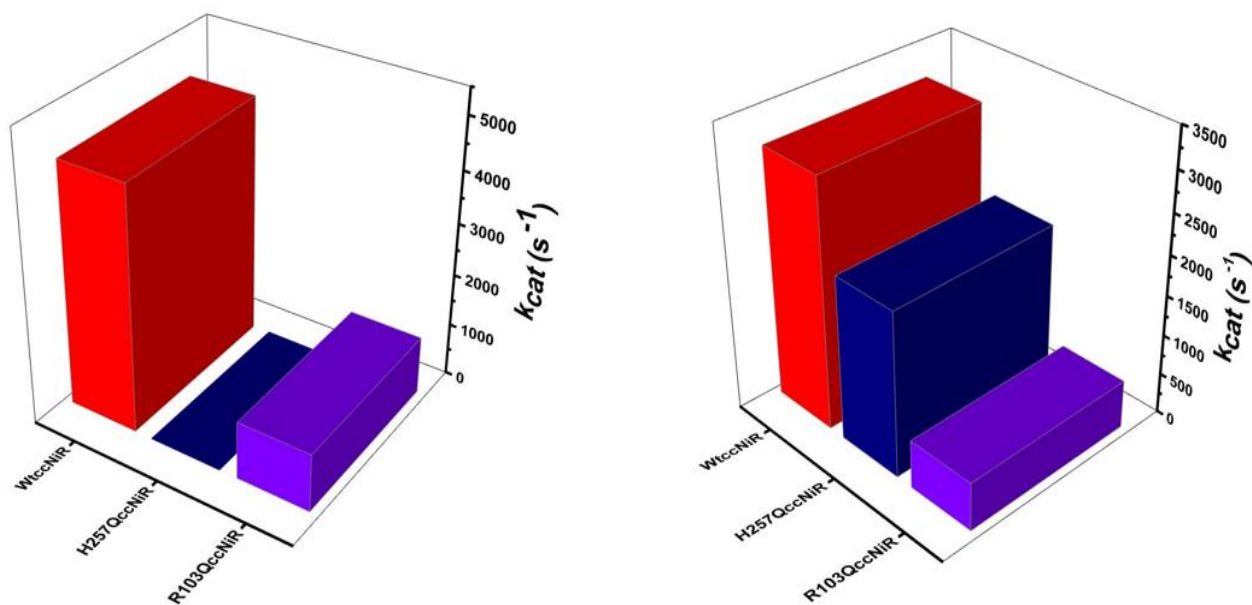| Enzyme	k_{cat} (s^{-1}) Nitrite as substrate	K_m (M) Nitrite as substrate	k_{cat} relative to wtccNiR	k_{cat} (s^{-1}) Hydroxylamine as substrate	K_m(M) Hydroxylamine as substrate	k_{cat} relative to wtccNiR
wtccNiR	4666±90	(2.62±0.34)x10^{-5}		3100±300	(21.3±7)x10^{-3}	
R103QccNiR	1107±24	(1.83±0.64)x10^{-4}	23%	602±28	(27.3 ± 6)x10^{-3}	19.4 %
H257QccNiR	11.27±0.6	(1.5±0.34)x10^{-4}	0.24%	2048±142	(21.1±5.4)x10^{-3}	66.06%

Figure 4.10. (a) Nitrite, and (b) hydroxylamine titration by wtccNiR, R103QccNiR, and H257QccNiR at pH=7.0
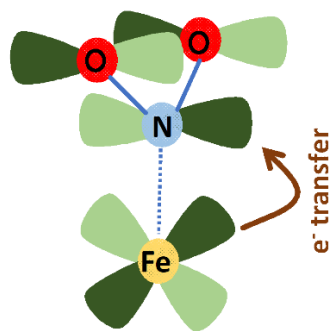

Figure 4.11. The pi back-bonding interaction between the nitrite molecule with the metal iron of heme.

The theoretical calculations of Bykov and Neese predict that the lowest energy path to the first N – O bond cleavage proceeds through successive direct protonations of a nitrite oxygen by H257 (Scheme 4.2).[6] The nearly complete suppression of nitrite reductase activity that we observe in the H257Q variant confirms H257's essential role in the first N – O bond cleavage step. However, the fact that wtccNiR is still active at pH 8 (Table 4.2), where H257 is likely to be mostly deprotonated, is less consistent with a *direct* protonating role for this amino acid. A direct protonating role is also inconsistent with the Chapter 2 results, which studied the effects of pH on the reduction of nitrite-loaded wtccNiR by TMPD (Section 2.3.2.2), for two reasons. First, loss of maximal activity as pH increases is not well modeled by deprotonation of a single amino acid residue such as H257 (Fig. 2.10, Section 2.4.2.2), and instead appears to involve two coupled proton losses. Second, similarly to its behavior in the standard assay, wtccNiR retains 20% of its activity even at pH 8.5, where the putative donor group(s) would be fully deprotonated. This contrasts with the near total loss of activity when H257 is absent entirely. As suggested in Chapter 2, a more conservative interpretation is that His273 modulates the pK_a values of one or more of the waters that form a complex hydrogen bonding network in the active site.[2, 7-9] In this view, it is the active site hydrogen bonding network that is disrupted by the H273 mutation, and that is essential for catalysis.

The 6× higher K_m value of the H257Q variant compared to wtccNiR also points to the importance of H257 for substrate binding. Nitrite binding to the active site iron likely involves substantial π-back bonding (Figure 4.11), and this bonding form is stabilized when two oxygen atoms from nitrite form hydrogen bonds with the H257 and R103 side chains.[6, 10] Mutation of H257 would therefore greatly affect nitrite binding, possibly altering the N – O bond orientation, which would also affect k_{cat}. Loss of H257 could even lead to a change in the preferred nitrite

linkage isomer from the N-bound nitro to the O-bound nitrito (Fig. 1.12, Section 1.6.2.1), as has been suggested for the *E. coli* ccNiR homologue.[11] A crystallographic study with H268NccNiR of the *E. coli* enzyme soaked with nitrite appeared to show the nitrito form in one protomer and the nitro form in that other, though the structure resolution was not high enough to be definitive.[12]

4.5.2. Tentative roles of conserved active site amino acids in cleavage of the second N-O bond

As mentioned earlier, a total of two N – O bonds need to be cleaved by ccNiR to form ammonium from nitrite. The hydroxylamine complex (Fe_{H1}-NH_2OH) is widely considered to be a reaction intermediate during nitrite ammonification by ccNiR. This conjecture is based on the fact that a hydroxylamine-bound ccNiR species has been crystallographically characterized,[2] and also on theoretical calculations.[13] The theoretical calculations suggested possible direct protonation roles for either H257 or Y206 (Section 1.6.2.3).

The results reported herein show that H257 is not absolutely required for the second bond cleavage, though k_{cat} is somewat smaller for H257Q than for the wild type (Fig. 4.10 and Table 4.2). More important for cleavage of the second N – O bond appears to be R103. Both the nitrite and hydroxylamine reductase activities of the R103Q variant are 20% - 25% those of the wild type in the standard assay (Table 4.2) indicating that, in this case, the mutation has affected the second N – O bond breaking step. Studies of the Y206F variant are currently under way in the Pacheco group to probe the role of Y206 in the catalytic process.
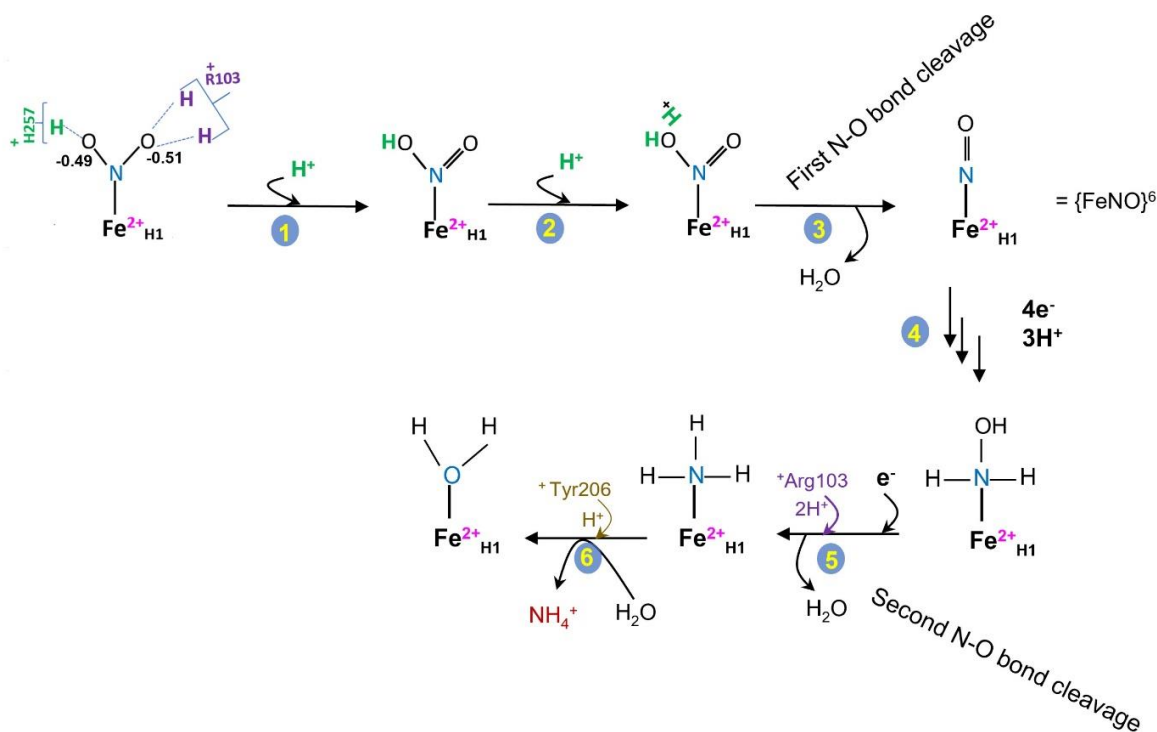
Scheme 4.2. Mechanism of nitrite ammonification by *S. oneidensis* ccNiR focusing the proton donation roles of active site amino acids. H1 indicates the heme#1 or active site heme. $^+$H257, $^+$R103 and $^+$Tyr206 indicate the protonation states. With strong reductants, H1 reduction likely precedes nitrite binding as shown here; TMPD (Chapter 2) is too weak a reductant to reduce the resting H1active site, so nitrite loading must precede reduction in that case. The theoretical model suggests a direct role for H257 in nitrite dehydration,[6] but our results are more consistent with a less direct role (see main text for details). The role of Y206 as a proton donor is based exclusively on the theoretical model of Bykov et al;[13] See section 1.6.2 for more details.

4.6. References

1.   Youngblut, M.; Judd, E. T.; Srajer, V.; Sayyed, B.; Goelzer, T.; Elliott, S. J.; Schmidt, M.; Pacheco, A. A., Laue crystal structure of Shewanella oneidensis cytochrome c nitrite reductase from a high-yield expression system. *J Biol Inorg Chem* **2012,** *17* (4), 647-62.

2.   Einsle, O.; Messerschmidt, A.; Huber, R.; Kroneck, P. M.; Neese, F., Mechanism of the six-electron reduction of nitrite to ammonia by cytochrome c nitrite reductase. *J Am Chem Soc* **2002,** *124* (39), 11737-45.

3.   Berry, E. A.; Trumpower, B. L., Simultaneous determination of hemes a, b, and c from pyridine hemochrome spectra. *Anal Biochem* **1987,** *161* (1), 1-15.

4.   Atkins, P., Overton, T., Rourke, J., Weller, M., Armstrong, F., and Hagerman, M. , *Shriver & Atkins' Inorganic Chemistry,* . 5th ed.; W. H. Freeman and Co., New York, NY: 2010.

5.   Youngblut, M.; Pauly, D. J.; Stein, N.; Walters, D.; Conrad, J. A.; Moran, G. R.; Bennett, B.; Pacheco, A. A., Shewanella oneidensis cytochrome c nitrite reductase (ccNiR) does not disproportionate hydroxylamine to ammonia and nitrite, despite a strongly favorable driving force. *Biochemistry* **2014,** *53* (13), 2136-44.

6.   Bykov, D.; Neese, F., Substrate binding and activation in the active site of cytochrome c nitrite reductase: a density functional study. *J Biol Inorg Chem* **2011,** *16* (3), 417-30.

7.   Ali, M.; Stein, N.; Mao, Y.; Shahid, S.; Schmidt, M.; Bennett, B.; Pacheco, A. A., Trapping of a Putative Intermediate in the Cytochrome c Nitrite Reductase (ccNiR)-Catalyzed Reduction of Nitrite: Implications for the ccNiR Reaction Mechanism. *J Am Chem Soc* **2019,** *141* (34), 13358-13371.

8.   Einsle, O.; Messerschmidt, A.; Stach, P.; Bourenkov, G. P.; Bartunik, H. D.; Huber, R.; Kroneck, P. M., Structure of cytochrome c nitrite reductase. *Nature* **1999,** *400* (6743), 476-80.

9.   Bamford, V. A.; Angove, H. C.; Seward, H. E.; Thomson, A. J.; Cole, J. A.; Butt, J. N.; Hemmings, A. M.; Richardson, D. J., Structure and spectroscopy of the periplasmic cytochrome c nitrite reductase from Escherichia coli. *Biochemistry* **2002,** *41* (9), 2921-31.

10.   Bykov, D.; Neese, F., Six-electron reduction of nitrite to ammonia by cytochrome c nitrite reductase: insights from density functional theory studies. *Inorg Chem* **2015,** *54* (19), 9303-16.

11.   Lockwood, C.; Butt, J. N.; Clarke, T. A.; Richardson, D. J., Molecular interactions between multihaem cytochromes: probing the protein-protein interactions between pentahaem cytochromes of a nitrite reductase complex. *Biochem Soc Trans* **2011,** *39* (1), 263-8.

12.   Lockwood, C. W. J.; Burlat, B.; Cheesman, M. R.; Kern, M.; Simon, J.; Clarke, T. A.; Richardson, D. J.; Butt, J. N., Resolution of Key Roles for the Distal Pocket Histidine in Cytochrome c Nitrite Reductases. *Journal of the American Chemical Society* **2015,** *137* (8), 3059-3068.

13.   Bykov, D.; Plog, M.; Neese, F., Heme-bound nitroxyl, hydroxylamine, and ammonia ligands as intermediates in the reaction cycle of cytochrome c nitrite reductase: a theoretical study. *JBIC Journal of Biological Inorganic Chemistry* **2014,** *19* (1), 97-112.

Chapter: 5. The Search for Low-Potential Intermediates in CcNiR-Catalyzed Reduction of Nitrite to Ammonia

5.1. Overview

As proposed in Fig. 1.14, the $Fe_{H1}^{II}(NO_2^-)$ and $\{Fe_{H1}NO\}^7$ moieties (Chapter 2) may not be the only catalytic intermediates that can be trapped by controlling the applied potential during nitrite reduction by *S. oneidensis* ccNiR. Based on the theoretical and experimental evidence reviewed in Section 1.6, Fig. 1.14 suggests that the rate-limiting step for ccNiR-catalyzed reduction of nitrite to ammonia is the final 2-electron reduction of a heme#1-bound hydroxylamine equivalent. A strong reducing agent such as MV_{red} can overcome this activation barrier, but weaker reducing agents will generate partially reduced nitrosylated ccNiR moieties. The results from Chapter 2 showed how the 1- and 2-electron reduced species $Fe_{H1}^{II}(NO_2^-)$ and $\{Fe_{H1}NO\}^7$ were trapped when TMPD was used to reduce nitrite-loaded ccNiR. If the Fig. 1.14 reaction path is acurate though, it might also be possible to trap 3- or 4-electron reduced intermediates by using more powerful reducing agents than TMPD that are nevertheless too weak to overcome the final activation barrier for reduction of ccNiR-bound hydroxylamine. Preliminary UV/Vis spectropotentiometric studies with nitrite-loaded ccNiR revealed evidence for a 4-electron reduced intermediate,[1] and a stopped-flow/freeze-quench investigation of the reaction between fully oxidized ccNiR and hydroxylamine generated further evidence for putative catalytic intermediates of the ccNiR-catalyzed reduction of nitrite to ammonium. This chapter summarizes preliminary studies of ccNiR-catalyzed nitrite reduction by reduced indigo trisulfonate (I3S$_{red}$), which is a stronger reductant ($\varepsilon_m° = -0.085$ V) than TMPD, but a weaker one than MV_{red}. The goal of this

study was to trap one or more nitrosylated ccNiR intermediates that are more reduced than $\{Fe_{H1}NO\}^7$.

5.2. Materials and Methods

5.2.1. General instrumentation and reagents

UV/Vis spectropotentiometry experiments were performed using a BASi Epsilon EC potentiostat to set the potential, and a CARY Bio 50 UV/Vis spectrophotometer to record the spectra at each applied potential. The complete apparatus was housed in an anaerobic glove box. All reagents were purchased from Thermo-fisher, Dot Scientific, MP Biomedicals unless mentioned specifically, are were of high bio-grade purity.

5.2.2. Determination the indigo trisulfonate extinction coefficient

A nominally 2 mM solution of potassium indigotrisulfonate (I3S, ACROS Organics™) in 50 mM HEPES pH =7 , also containing 0.5 M NaCl, was prepared in a glovebox using previously degassed buffer. The fully oxidized sample was then transferred into a special 0.022 cm pathlength optically transparent thin-layer electrode (OTTLE) UV/Vis cuvette and connected to all the electrodes as shown Fig. 5.1. An Ag/AgCl electrode was the reference, and was standardized prior to each use by collecting a cyclic voltammogram of methyl viologen and comparing the measured midpoint potential to the literature value ($\varepsilon_m° = -449$ mV vs SHE).[2] All potentials measured vs the Ag/AgCl electrode were subsequently converted to the SHE scale. An EC Epsilon (BASi) potentiometer was used to perform a "Controlled Potential Electrolysis (CPE)'' experiment by applying potentials from + 30 mV to – 200 mV vs SHE at 10 mV intervals. After a 10 minute interval at each applied potential, a UV/Vis spectrum was collected in the 200 nm - 800 nm range using the CARY Bio 50 UV/Vis spectrophotometer.
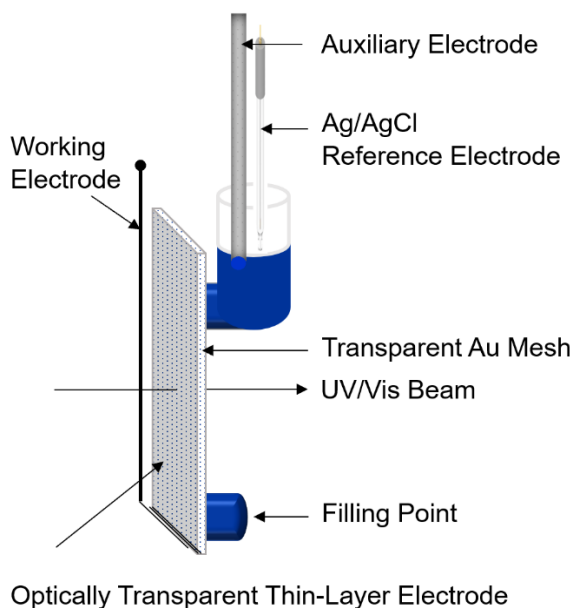
Figure 5.1. Determing the extinction coefficient and mid-point potential of the indigo tri-sulfonate (I3S) salt in a UV/Vis spectropotentiometric experiment. The special optically transparent thin-layer electrode (OTTLE) cell was used as the reaction compartment and an Ag/AgCl electrode was used as the reference. Potentials were applied from +30 mV to -200 mV (vs SHE) in 10 mV intervals.

5.2.3. Preparation of low-potential reducing agents by bulk controlled potential electrolysis

Solutions containing varying ratios of oxidized and reduced electroactive species were used to poise ccNiR at a desired state of reduction. As an example, to prepare a solution containing reduced and oxidized I3S ($\varepsilon_m° = -81$ mV vs SHE)[3] in slightly over 1:1 ratio, a stock solution of 100 mM oxidized I3S salt in 50 mM HEPES buffer at pH = 7.0, also containing 0.5 M NaCl, was prepared in a glovebox and transferred to a bulk electrolysis cell (Fig. 5.2). A magnetic stir bar that had previously been degassed for at least three days under vacuum in the glovebox antechamber was used to mix the sample during the CPE process. A fixed potential of -90 mV vs SHE was applied for 5 minutes, after which the solution in the cell's sidearm (Fig. 5.2) was mixed carefully with the solution in the main compartment using a 1 mL pipette. The sequence of 5-minute applied potential followed by mixing was repeated until the currents measured at the

beginning and end of the 5-minute intervals were within 50 μA of each other. The solution of

oxidized I3S was deep blue (Fig. 5.2a), and went to greenish-yellow when roughy 50% reduced
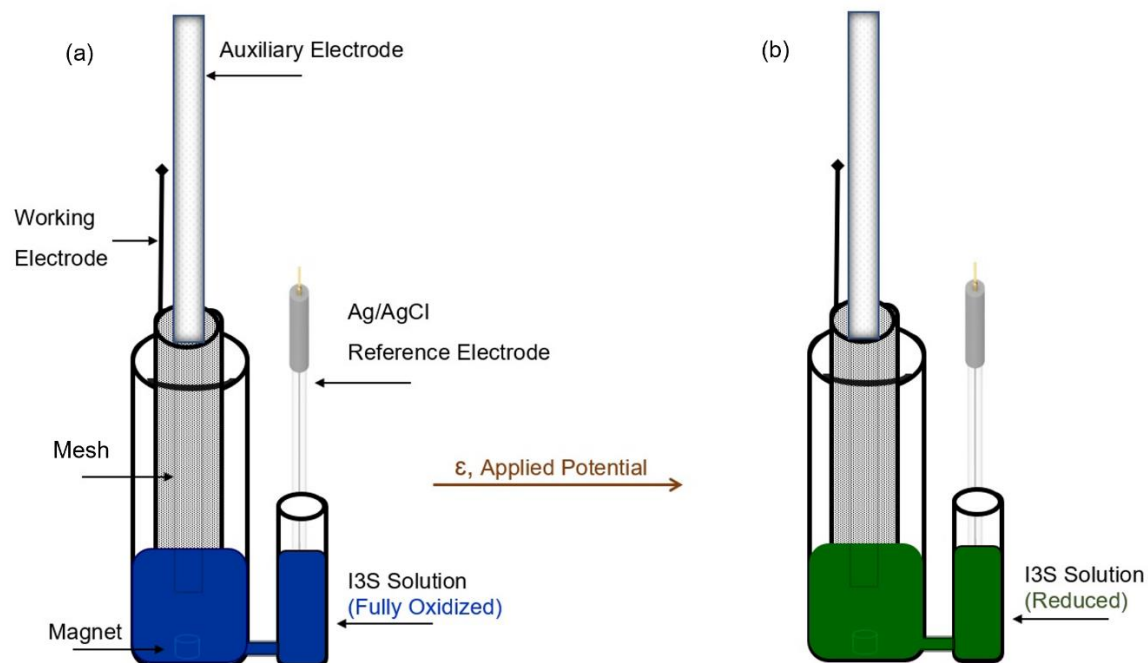
(Fig. 5.2b).

Figure 5.2. Bulk electrolysis of indigo trisulfonate (I3S) at a fixed applied potential. (a) Oxidized I3S salt is blue, and after reducing at -90 mV vs SHE, the solution color changes to greenish-yellow (b).

5.2.4. Steady-state nitrite reduction by I3S$_{red}$ catalyzed by *S. oneidensis* wtccNiR

Solutions containing I3S in concentrations ranging from 10 μM - 50 μM were partially

reduced at −90 mV vs SHE applied potential, as described in the previous section, then mixed with

solutions containing micromolar concentrations of fully oxidized wtccNiR and mM concentrations

of nitrite. A UV/Vis spectrophotometer was used to monitor the reoxidation of I3S$_{red}$. Initially, the reoxidation was monitored for 1 hour in the range from 300 nm - 800 nm at 15 s intervals (240 cycles total). Later experiments were monitored for 3 minutes only (12 cycles at 15s intervals).

To quantify how much, if any, hydroxylamine was generated as I3S re-oxidized, Six samples were prepared as just described, but using 150 μM I3S. After 3 minutes the reaction mixture was subjected to a hydroxylamine assay, as described in more detail in the results section. The hydroxylamine assay was performed by fellow graduate student Victoria Mandella.

5.3. Results

5.3.1. In-house extinction coefficient and midpoint potential determination for I3S

The blue traces in Fig. 5.3a show the spectral changes seen in the experiment described in section 5.2.2, where a solution of I3S was reduced stepwise in a UV/Vis spectropotentiometry experiment. The data were fit with the Nernst equation (Scheme 3.1), with the number of electrons transferred fixed at $n = 2$ (dotted red traces, Fig. 5.3a). An absorbance vs applied potential slice of the Fig. 5.3 spectra at 600 nm is shown in Fig. 5.4. The exact concentration of the I3S solution was obtained from its absorbance at 600 nm and the known extinction coefficient at that wavelength (14,600 $M^{-1}cm^{-1}$),[3] after which extinction coefficient spectra for both the oxidized and reduced forms of I3S (I3S$_{ox}$ and I3S$_{red}$) could be obtained from the fits of the Fig 5.3a data (Fig. 5.3b). The Nernstian fit also yielded a midpoint potential of $\varepsilon_m° = -74$ mV vs SHE for I3S, which is slightly higher but close to the literature value ($\varepsilon_m° = -81$ mV vs SHE).[3]

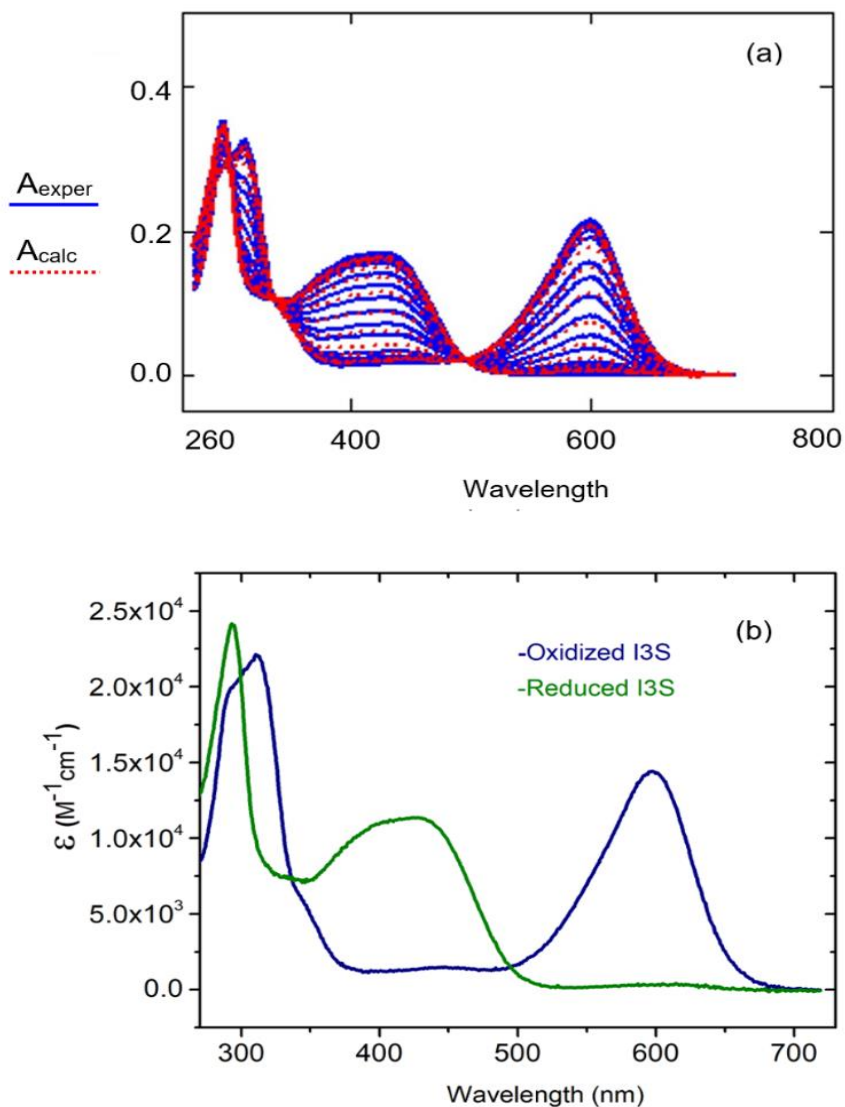**Figure 5.3.** UV/Vis spectropotentiometric analysis of indigo tri-sulfonate (I3S) using the Nernst equation. (a) A_{exper} refers to the theoretical spectra (blue solid line) at each potential and A_{calc} refers to the calculated value at each applied potential (dotted red lines). (b) Fully oxidized (blue) and reduced (green) I3S extinction coefficient spectra calculated from the experiment.
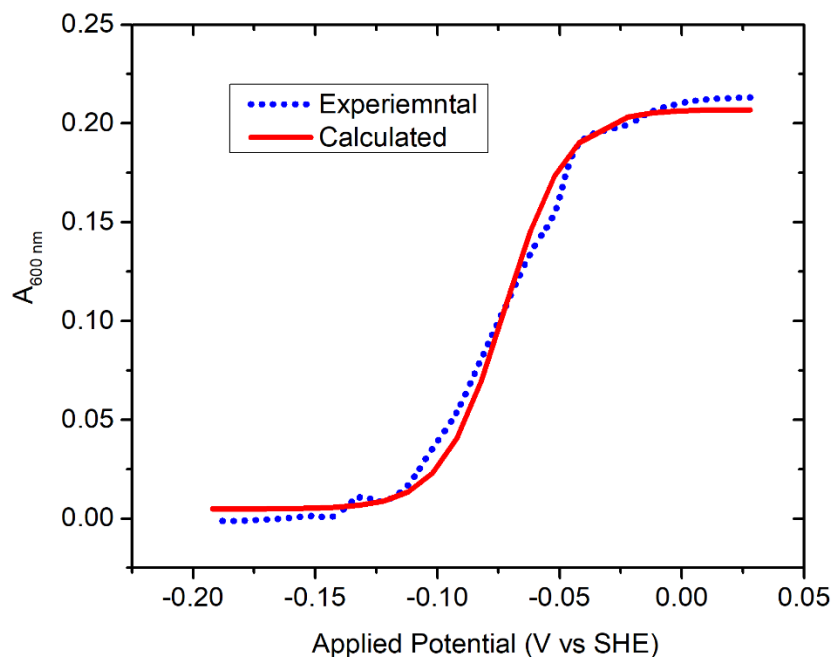
Figure 5.4. The applied potential vs absorbance slice at 600nm, obtained from the Fig. 5.3 spectra. Dotted blue line: experimental values; red line: values calculated by least-squares fit to the Nernst equation, using $n = 2$ as the number of electrons. The applied potential range was from +30mV to -200mV vs SHE.

5.3.2. Evidence for ccNiR heme#4 reduction by I3S$_{red}$

Figure 5.5 shows the spectral changes observed in a solution initially containing 2 μM wtccNiR, 0.5 mM nitrite and 30 μ mM I3S pre-reduced at a −90 mV applied potential. The major spectral changes can be ascribed to re-oxidation of I3S$_{red}$, as can be seen qualitatively by comparing the Fig. 5.5 spectra to the Fig. 5.3b I3S extinction coefficient spectra. However, the Fig. 5.5 spectra also show clear contributions from the ccNiR hemes. The most prominent c-heme feature is the Soret band centered around 409 nm that becomes distinct once I3S$_{red}$ re-oxidizes completely (the reduced indigo absorbs strongly in the 400 nm region, whereas I3S$_{ox}$ does not; Fig. 5.3b). The most intriguing c-heme feature though, is not the Soret band, but rather it's the small but distinct shoulder that is visible at 553 nm in the Fig 5.5 spectra (enlarged in the Fig. 5.5b

141

inset). Signals in the 550 nm – 555 nm range are characteristic of most low-spin ferrous c hemes, but are *not* detected for the ferrous nitrite-loaded active site heme#1.[4] Therefore, the presence of such a signal indicates that, at the −90 mV applied potential, one of the 6-coordinate ccNiR hemes is being reduced in addition to the active site. An earlier spectropotentiometric analysis showed that, after the active site heme#1, the next heme to reduce in *S. oneidensis* wtccNiR is heme#4 (Fig. 5.6), which has a midpoint potential of −89 mV.[5] Therefore, the 553 nm signal seen in Fig. 5.3b is tentatively assigned to reduced heme#4.
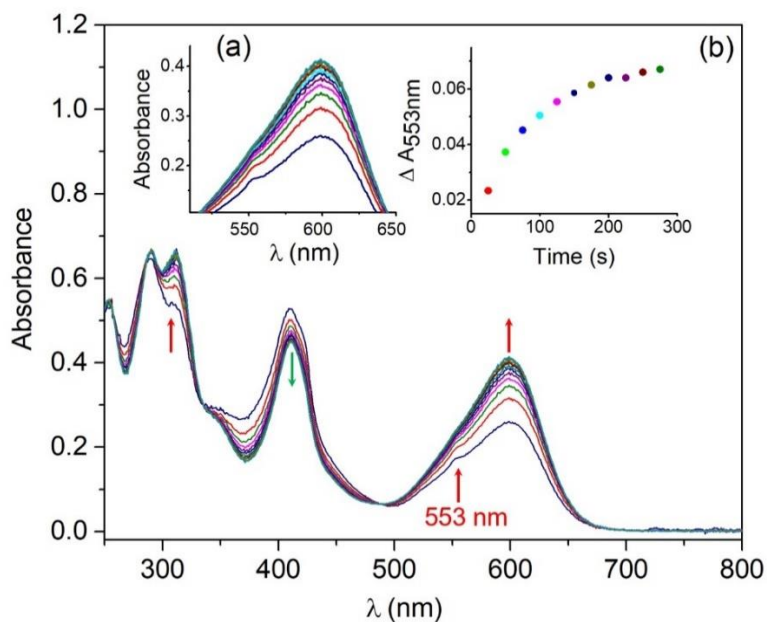
Figure 5.5. Spectral changes observed in a solution initially containing 2 μM wtccNiR, 0.5 mM nitrite and 30 μM I3S pre-reduced at a −90 mV applied potential (see main text for details). The main graph shows 12 spectra taken at 15 s intervals. The inset (a) shows the spectral changes in the range from 500 nm to 700 nm to focus more intensively on the shoulder at 553 nm, and inset (b) shows the absorbance change vs time at 553 nm, where the shoulder is seen (arrows in the spectra).

$\varepsilon^\circ_1 = +0.027$ V (Heme#1)
$\varepsilon^\circ_2 = -0.089$ V (Heme#4)
$\varepsilon^\circ_3 = -0.388$ V (Heme#3)
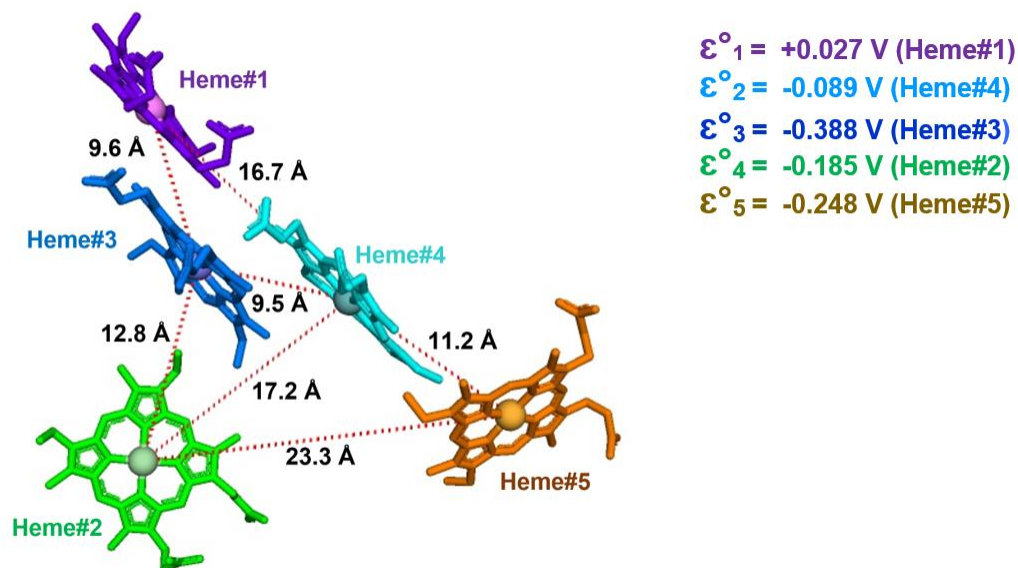$\varepsilon^\circ_4 = -0.185$ V (Heme#2)
$\varepsilon^\circ_5 = -0.248$ V (Heme#5)

Figure 5.6. The heme arrangement in one of the ccNiR enzyme protomers (PDB 6P73). The stick structure refers to the porphyrin ring and spheres in the center represent the iron atoms. All the distances are shown in Å. The Fe-Fe distance (red dotted line) between heme#1 (purple) to heme#3 (blue) is 9.6 Å whereas the distance between heme#1 and heme#3 (cyan) is 16.7 Å. The *S. oneidensis* heme midpoint potentials (vs SHE) obtained in the preence of the strong-field (SF) ligand cyanide are shown in the inset.[4-5]

5.3.3. Test for the presence of hydroxylamine as a reaction intermediate during nitrite ammonification by wtccNiR

The spectral changes seen in Fig. 5.5 show that ccNiR catalyzes the oxidation of $I3S_{red}$ by nitrite, and that the rate of $I3S_{red}$ oxidation is significantly faster than that of NO· formation seen in experiments with TMPD and other weak reductants. This suggests that the nitrogenous product of nitrite reduction is something other than NO·, since NO· formation does not become faster under more reducing conditions (Section 2.3.1). Three likely possibilities are nitrous oxide, hydroxylamine or ammonium. This section describes preliminary experiments designed to test for hydroxylamine production. The hydroxylamine assay was one described by Johnson in 1968, and it was performed by Victoria Mandella of the Pacheco group. The basic procedure was as follows.

The six samples for this experiment were similar to the one used in the Section 5.3.2 experiment, but they contained 150 μM of ~50% reduced I3S instead of 130 μM. Furthermore, each sample contained a fixed amount of hydroxylamine, ranging from 0 μM to 1.5 μM. The reaction mixtures were allowed to incubate for 3 minutes in the glovebox, after which they were filtered using a centrifugal concentrator to separate the protein from the low molecular weight compounds. The low molecular weight filtrate was incubated with *p*-nitrobenzaldehyde, a procedure that generates the oxime with whatever hydroxylamine is present,[6] after which the UV spectrum of the assay mixture was taken. As a control, six samples containing only 0.3 μM – 1.5 μM hydroxylamine hydrochloride were also incubated with *p*-nitrobenzaldehyde to generate the oxime.

Figure 5.7 shows the UV/Vis spectra of the oxime samples made from blank solutions that contained only hydroxylamine; the band with maximum at 370 nm arises from the oxime. Fig. 5.8 shows the A370 vs added hydroxylamine for the blank solution and the solution that also contained the products from nitrite reduction, for two experiments performed at different $I3S_{red}$ concentrations. In both cases, the plots of the blank and of the reaction mixtures overlap within the uncertainty of the method, indicating that no additional hydroxylamine was generated by $I3S_{red}$ reduction of nitrite. If hydroxylamine had been generated, the A370 vs added hydroxylamine line for the reaction mixture would still have been parallel to the line for the blank, but with a non-zero A370 nm intercept.
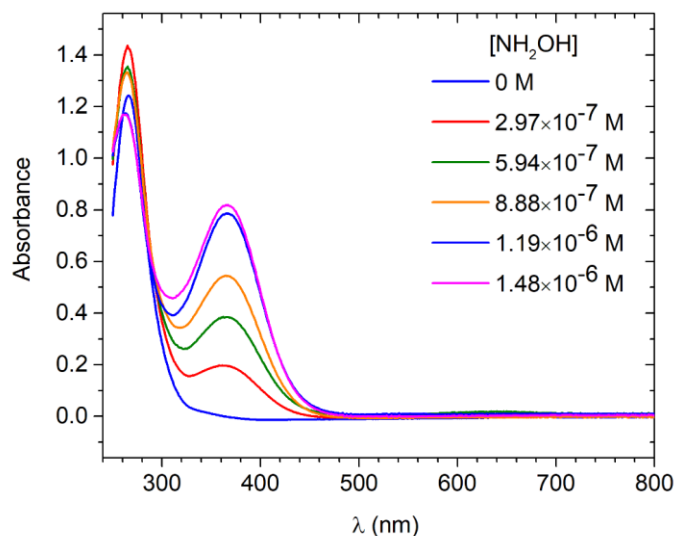
Figure.5.7. UV/Vis spectra of the oxime generated when the protein-free products of ccNiR-ctalyzed nitrite reduction by I3S$_{red}$ were subjected to the hydroxylamine assay (see main text for details).[6] The six different spectra were collected for solutions to which six different hydroxylamine concentrations had been added. The sample spectra were compared to spectra obtained under the same assay conditions which contained known amounts of hydroxylamine, but no nitrite, I3S$_{red}$ or ccNiR.
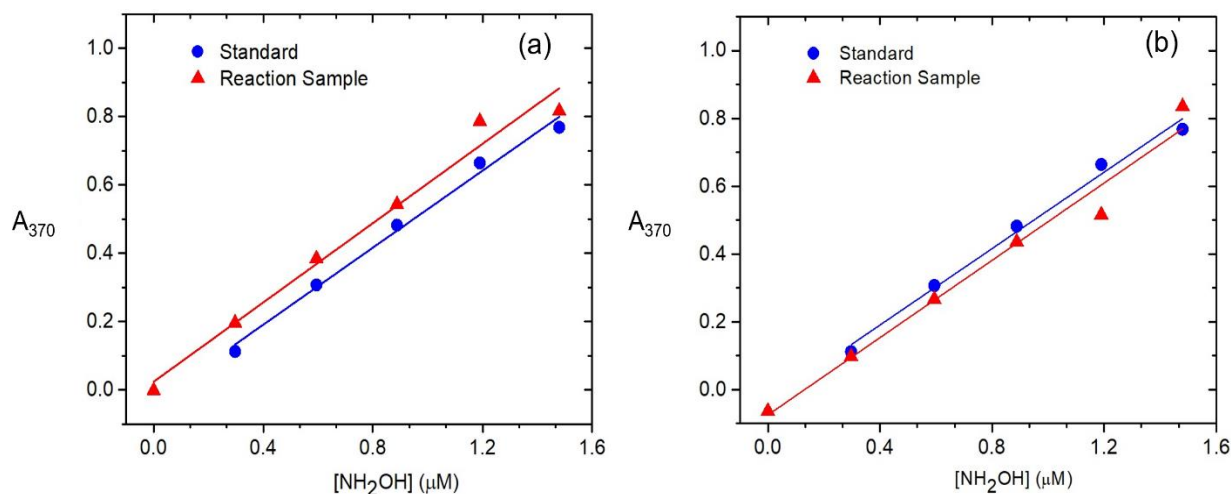

Figure 5.8. Hydroxylamine detection after *S. oneidensis*-catalyzed wtccNiR reduction of nitrite by I3S$_{red}$. (a) 30 μM, (b) 150 μM I3S salt was used as an electron donor after reduction at -90mV vs SHE applied potential. Hydroxylamine detection was with the Johnson assay, in which hydroxylamine reacts with p-nitrobenzaldehyde to generate the oxime (Fig. 5.7).[6] Blue traces: generated from blank solutions containing only added hydroxylamine. Red traces: generated from reaction mixtures to which hydroxylamine was later added as an internal standard. The blank and reaction mixture traces overlap, showing that no additional detactable hydroxylamine was generated when nitrite was reduced by I3S$_{red}$

145

5.4. Discussion

The experiments presented in this chapter lead to two important conclusions. First, when ccNiR catalyzes the reduction of nitrite by $I3S_{red}$ in solutions poised at roughly -90 mV, a long-lived reduced ccNiR species is generated in which heme#4 is at least partially in the ferrous state. Second, catalytic reduction of nitrite by I3S does not generate free hydroxylamine. Scheme 5.1 proposes a guess as to the character of the putative metastable intermediates that might be generated when $\{Fe_{H1}NO\}^7$ is reduced by reductants such as I3S that have potency between that of TMPD and MV_{red}. The scheme takes into account the results from this chapter, the theoretical calculations of Bykov and Neese (Section 1.6.2),[7-10] results from earlier experiments by Youngblut et al.[11] and the fact that hemes#1 and #4 (Fig. 5.6) are the first to reduce as the potential applied to *S. oneidensis* ccNiR is lowered.[5]

In Scheme 5.1, the 3- and 4-electron reduced nitrite-loaded ccNiR species are labeled as $ccNiR^{3-}$ and $ccNiR^{4-}$, respectively, to allow for a flexible interpretation of what such species might be. The 4-electron reduced moiety $ccNiR^{4-}$ is of special interest because preliminary UV/Vis spectropotentiometry experiments suggested that $\{Fe_{H1}NO\}^7$ reduces in a concerted 2-electron step.[1] Focussing on $ccNiR^{4-}$ in Scheme 5.1, one can see that the 4-electron reduced moiety could comprise of a $\{Fe_{H1}(HNO)\}^8$ active site and reduced heme#4, $[\{Fe_{H1}(HNO)\}^8, Fe_{H4}^{II}]$, a hydroxylamine radical at a ferrous active site ($Fe_{H1}^{II}H_2NO\cdot$) and a ferric heme#4, $[Fe_{H1}^{II}H_2NO\cdot, Fe_{H4}^{III}]$, or a hydroxylamine at a ferric active site and a ferric heme#4, $[Fe_{H1}^{III}H_2NOH, Fe_{H4}^{III}]$. The presence of a ferrous heme#4 signal in the UV/Vis spectra of nitrite-loaded ccNiR reduced by $I3S_{red}$ (Fig. 5.5) suggests that at least some $[\{Fe_{H1}(HNO)\}^8, Fe_{H4}^{II}]$ is being generated in the reduction.
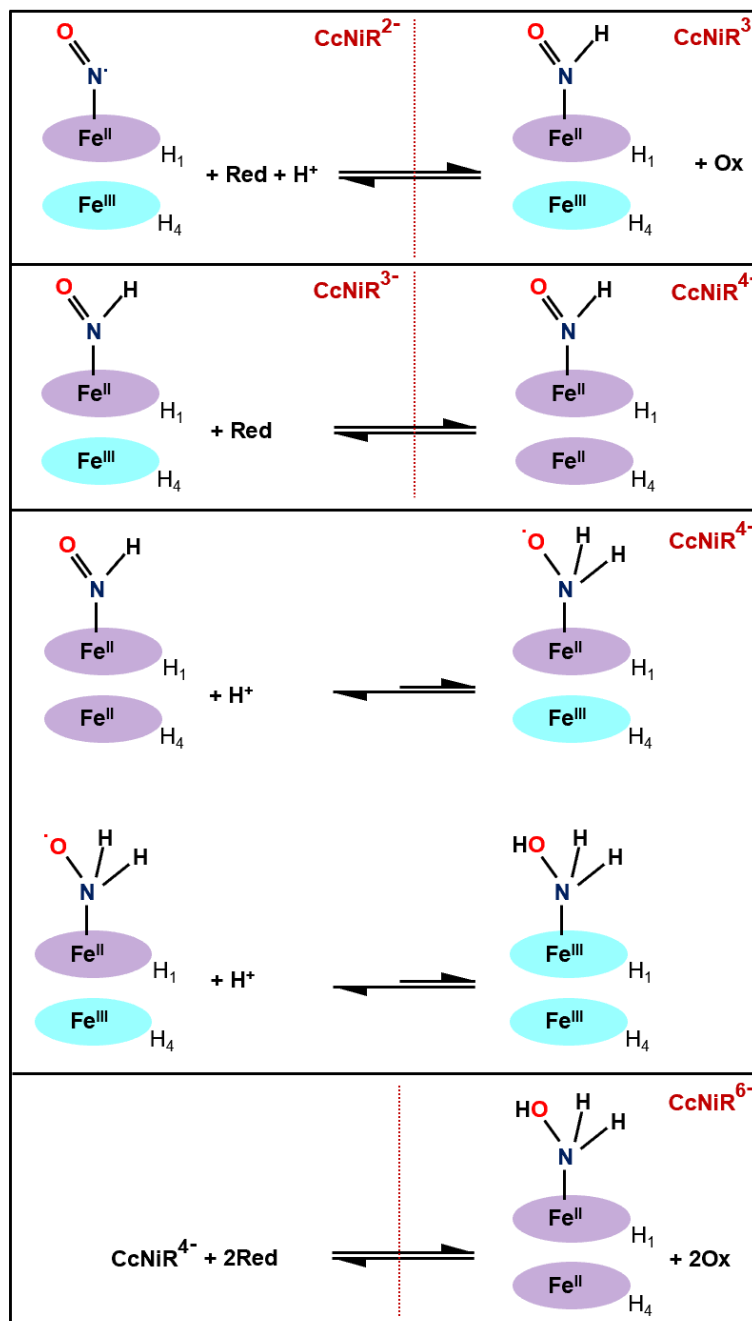
Scheme 5.1. Species that may be generated at applied potentials between -80 mV and -120 mV vs SHE. Here, H_1 and H_4 denote the heme#1 (active site heme) and heme#4, respectively. The light blue color and pink color indicate the oxidized and reduced states of iron in the heme center, respectively. ccNiR^{2-} refers the $\{Fe_{H1}NO\}^7$ formation in the active site, wherease ccNiR^{3-} refers $\{Fe_{H1}(HNO)\}^8$. The Enemark-Feltham notation of $\{Fe_{H1}NO\}^7$ and $\{Fe_{H1}(HNO)\}^8$ is described in the main text.

147

The UV/Vis stopped-flow and rapid freeze-quench EPR experiments of Youngblut et al,[11] summarized in Section 1.6.3.2, provided evidence that a $Fe_{H1}^{II}H_2NO\cdot$ moiety built up within 100 ms of mixing hydroxylamine with oxidized ccNiR, and then decayed, but not to zero concentration, in a process that transferred electrons from the nitrogenous moiety to the *c*-heme pool. A final equilibrium was reached within 10s of mixing. Taken together with the results reported in this chapter, the earlier rapid freeze-quench studies may indicate that the 4-electron reduced moiety is not a single species but rather is an equilibrium mixture of $[\{Fe_{H1}(HNO)\}^8,\ Fe_{H4}^{II}]$ and $[Fe_{H1}^{II}H_2NO\cdot,\ Fe_{H4}^{III}]$. Such a conjecture would explain how the design of ccNiR minimizes release of toxic free hydroxylamine. The high K_m value seen in the ccNiR catalyzed reduction of hydroxylamine by MV_{red} (~0.02 M, Table 4.2) suggests that hydroxylamine binds weakly to the active site. Therefore, optimizing the structure to stabilize $[\{Fe_{H1}(HNO)\}^8,\ Fe_{H4}^{II}]$ and $[Fe_{H1}^{II}H_2NO\cdot,\ Fe_{H4}^{III}]$ would minimize the concentration of the labile $[Fe_{H1}^{III}H_2NOH,\ Fe_{H4}^{III}]$ moiety. According to the Scheme 5.1 mechanism, ccNiR-bound hydroxylamine could become a dominant species after the final two electrons for hydroxylamine reduction to ammonia become available, but presumably at that point reduction would be faster than hydroxylamine dissociation. Studies are now under way to test the conjectures presented in Scheme 5.1, and also to identify the nitrogenous product(s) of ccNiR-catalyzed nitrite reduction by $I3S_{red}$.

5.5. References

1.   Stein, N. In *Spectroscopic and electrochemical studies of Shewanella oneidensis cytochrome c nitrite reductase, and improving c-heme expression systems*, 2014.

2.   Watanabe, T. H., K.,, Measurement of the extinction coefficient of the methyl viologen cation radical and the efficiency of its formation by semiconductor photocatalysis. *J. Phys. Chem.* **1982,** *86,* , 2617-2619.

3.   Tratnyek, P. G.; Reilkoff, T. E.; Lemon, A. W.; Scherer, M. M.; Balko, B. A.; Feik, L. M.; Henegar, B. D., Visualizing Redox Chemistry: Probing Environmental Oxidation–Reduction Reactions with Indicator Dyes. *The Chemical Educator* **2001,** *6* (3), 172-179.

4.   Ali, M.; Stein, N.; Mao, Y.; Shahid, S.; Schmidt, M.; Bennett, B.; Pacheco, A. A., Trapping of a Putative Intermediate in the Cytochrome c Nitrite Reductase (ccNiR)-Catalyzed Reduction of Nitrite: Implications for the ccNiR Reaction Mechanism. *J Am Chem Soc* **2019,** *141* (34), 13358-13371.

5.   Stein, N.; Love, D.; Judd, E. T.; Elliott, S. J.; Bennett, B.; Pacheco, A. A., Correlations between the Electronic Properties of Shewanella oneidensis Cytochrome c Nitrite Reductase (ccNiR) and Its Structure: Effects of Heme Oxidation State and Active Site Ligation. *Biochemistry* **2015,** *54* (24), 3749-58.

6.   Johnson, D. P., Spectrophotometric determination of oximes and unsubstituted hydroxylamine. *Analytical Chemistry* **1968,** *40* (3), 646-648.

7.   Bykov, D.; Neese, F., Substrate binding and activation in the active site of cytochrome c nitrite reductase: a density functional study. *J Biol Inorg Chem* **2011,** *16* (3), 417-30.

8.   Bykov, D.; Neese, F., Reductive activation of the heme iron–nitrosyl intermediate in the reaction mechanism of cytochrome c nitrite reductase: a theoretical study. *JBIC Journal of Biological Inorganic Chemistry* **2012,** *17* (5), 741-760.

9.   Bykov, D.; Plog, M.; Neese, F., Heme-bound nitroxyl, hydroxylamine, and ammonia ligands as intermediates in the reaction cycle of cytochrome c nitrite reductase: a theoretical study. *JBIC Journal of Biological Inorganic Chemistry* **2014,** *19* (1), 97-112.

10.   Bykov, D.; Neese, F., Six-electron reduction of nitrite to ammonia by cytochrome c nitrite reductase: insights from density functional theory studies. *Inorg Chem* **2015,** *54* (19), 9303-16.

11.   Youngblut, M.; Pauly, D. J.; Stein, N.; Walters, D.; Conrad, J. A.; Moran, G. R.; Bennett, B.; Pacheco, A. A., Shewanella oneidensis cytochrome c nitrite reductase (ccNiR) does not disproportionate hydroxylamine to ammonia and nitrite, despite a strongly favorable driving force. *Biochemistry* **2014,** *53* (13), 2136-44.

Chapter 6

Conclusions And Suggestions For Further Study

6.1. Concluding Remarks

The results presented in this thesis show how transient intermediates in the *S. oneidensis* ccNiR-catalyzed reduction of nitrite to ammonium can be trapped and studied by judicious choice of reducing agent. With strong reducing agents such as MV_{red}, used in the standard assay, nitrite is reduced to ammonia in a process that generates no detectable intermediates. On the other hand, reduction of nitrite-loaded ccNiR by the weak reductant TMPD generates a transient intermediate, assigned as the 1-electron reduced species $Fe_{H1}^{II}(NO_2^-)$, and the long-lived species $\{Fe_{H1}NO\}^7$ (Chapter 2). Using the more powerful reducing agent $I3S_{red}$, which is nevertheless still weaker than MV_{red}, allows one or more long-lived species, tentatively assigned as 4-electron reduced ccNiR moieties collectively referred to as $ccNiR^{4-}$, to accumulate (Chapter 5, Scheme 5.1).

Under steady-state conditions, ccNiR was found to catalyze the slow 1-electron reduction of nitrite to NO· by TMPD (Chapter 2). The rate of $TMPD^+$ formation was found to be directly proportional to the concentration of $TMPD^+$ at low TMPD concentrations, providing good evidence that the primary mechanism of NO· release is via the more labile $\{Fe_{H1}NO\}^6$ moiety (Scheme 2.4). However, a small amount of NO· release was observed even in the absence of $TMPD^+$, and at high concentrations of TMPD, where oxidation of $\{Fe_{H1}NO\}^7$ to $\{Fe_{H1}NO\}^6$ can't occur. This demonstrated that $\{Fe_{H1}NO\}^7$ must release NO· as well, albeit very slowly. The steady-state studies also showed that nitrite is a substrate inhibitor of NO· release when TMPD is the electron source, probably because it blocks exit by NO· through the nitrite entry channel.

151

Altogether, the Chapter 2 results show that ccNiR appears to be optimized to capture nitrite and minimize release of free NO·. Capture is achieved by reducing bound nitrite with even weak electron donors such TMPD, and NO· release is minimized by stabilizing the comparatively substitutionally inert $\{Fe_{H1}NO\}^7$ over the more labile $\{Fe_{H1}NO\}^7$.

The optimization of ccNiR for avoiding loss of partially reduced nitrogenous intermediates appears to extend to the 4-electron reduced $ccNiR^{4-}$ moieties generated when nitrite-loaded ccNiR is reduced by $I3S_{red}$. The preliminary studies of Chapter 5 showed that no detectable amounts of toxic hydroxylamine were released under these conditions. Scheme 5.1 suggests as a possible explanation for this that $ccNiR^{4-}$ is primarily a mixture of the species $[\{Fe_{H1}(HNO)\}^8, Fe_{H4}^{II}]$ and $[Fe_{H1}^{II}H_2NO·, Fe_{H4}^{III}]$, while the presumedly labile moiety $[Fe_{H1}^{III}H_2NOH, Fe_{H4}^{III}]$ is minimized. The Scheme 5.1 conjecture is based on the fact that a signal characteristic of Fe_{H4}^{II} is seen in the UV/Vis spectra of nitrite-loaded ccNiR after its reduction by $I3S_{red}$ (Fig. 5.5), and also on earlier results from experiments that investigated the reaction between hydroxylamine and ccNiR, and provided evidence for an intermediate that contained the $H_2NO·$ radical.[1]

The H257Q variant of ccNiR was found to have $1/400^{th}$ of the wild type enzyme's nitrite reductase activity in the standard assay in which methyl viologen monocation radical (MV_{red}) is the electron source, but nearly normal hydroxylamine reductase activity (Chapter 4). This demonstrated that H257 is essential for nitrite reduction but not for reduction of hydroxylamine, a putative intermediate in the catalytic process. UV/Vis spectropotentiometry showed that the nitrite-loaded active site of H257Q still reduced at fairly high applied potential ($\varepsilon_m^o = +87$ mV vs SHE compared to 240 mV for the wild type), but the reduction was by one electron, whereas the wild type is reduced in a concerted 2-electron step. The experiments with the variant, coupled with

the pH-dependent stopped flow experiments with wtccNiR presented in Chapter 2, confirm H257's importance in facilitating nitrite reduction, but suggest that its role is to modulate the pK_a values of one or more of the waters that form a complex hydrogen bonding network in the active site. This is view is more conservative than theoretical predictions of direct histidine involvement in nitrite diprotonation leading to N – O bond cleavage that have been suggested on the basis of structural and computational studies.[2-4]

The results presented herein focused primarily on the detection and kinetic characterization of putative intermediates generated during the ccNiR-catalyzed reduction of nitrite to ammonium. These results pave the way for future investigations that will aim to characterize the transient intermediates spectroscopically and structurally; such investigations are already under way in the Pacheco group. Some EPR characterization of the species $\{Fe_{H1}NO\}^7$, and the proposed species $[\{Fe_{H1}(HNO)\}^8, Fe_{H4}^{II}]$ and $[Fe_{H1}^{II}H_2NO\cdot, Fe_{H4}^{III}]$ has already been done,[5-6] and has shown that these species have some intriguing electronic properties. In future studies samples will be prepared by rapid freeze-quench, which will allow the transient $Fe_{H1}^{II}(NO_2^-)$ to be trapped in addition to the more long-lived $\{Fe_{H1}NO\}^7$, and the proposed species $[\{Fe_{H1}(HNO)\}^8, Fe_{H4}^{II}]$ and $[Fe_{H1}^{II}H_2NO\cdot, Fe_{H4}^{III}]$. Rapid freeze-quench may also reveal a 3-electron reduced species (ccNiR^{3-}, Scheme 5.1), which has been proposed as a transient intermediate in theoretical studies,[3, 7] but has not been observed in our kinetic studies thus far. In addition to CW-EPR spectroscopy, samples prepared by rapid freeze-quench will be investigated using more advanced EPR techniques, and also Mossbauer spectroscopy, in collaboration with Professor Wilcoxen of the UWM chemistry department. Finally, in collaboration with Professor Schmidt from the UWM physics department, preparations are under way to study the reaction of nitrite-loaded ccNiR with TMPD (and later I3S$_{red}$) using time-resolved serial femtosecond X-ray crystallography (TR-SFX). This technique

uses X-ray free electron lasers (XFELS) to capture diffraction patterns of enzymes that are in the middle of reactions. The results presented herein have shown that $Fe_{H1}^{II}(NO_2^-)$ and $\{Fe_{H1}NO\}^7$ at least, and possibly also some of the proposed $ccNiR^{4-}$ species, should be readily amenable to investigation by TR-SFX techniques recently developed by Prof. Schmidt and his colleagues. Time-resolved crystallographic analyses could answer questions about the ccNiR reaction mechanism that no other experiment could, such as the precise way in which H257 and other conserved active site amino acids contribute to the nitrite protonation steps necessary for the first N – O bond cleavage.

6.2. References

1.   Youngblut, M.; Pauly, D. J.; Stein, N.; Walters, D.; Conrad, J. A.; Moran, G. R.; Bennett, B.; Pacheco, A. A., Shewanella oneidensis cytochrome c nitrite reductase (ccNiR) does not disproportionate hydroxylamine to ammonia and nitrite, despite a strongly favorable driving force. *Biochemistry* **2014,** *53* (13), 2136-44.

2.   Bykov, D.; Neese, F., Substrate binding and activation in the active site of cytochrome c nitrite reductase: a density functional study. *J Biol Inorg Chem* **2011,** *16* (3), 417-30.

3.   Bykov, D.; Neese, F., Reductive activation of the heme iron–nitrosyl intermediate in the reaction mechanism of cytochrome c nitrite reductase: a theoretical study. *JBIC Journal of Biological Inorganic Chemistry* **2012,** *17* (5), 741-760.

4.   Einsle, O.; Messerschmidt, A.; Huber, R.; Kroneck, P. M.; Neese, F., Mechanism of the six-electron reduction of nitrite to ammonia by cytochrome c nitrite reductase. *J Am Chem Soc* **2002,** *124* (39), 11737-45.

5.   Ali, M.; Stein, N.; Mao, Y.; Shahid, S.; Schmidt, M.; Bennett, B.; Pacheco, A. A., Trapping of a Putative Intermediate in the Cytochrome c Nitrite Reductase (ccNiR)-Catalyzed Reduction of Nitrite: Implications for the ccNiR Reaction Mechanism. *J Am Chem Soc* **2019,** *141* (34), 13358-13371.

6.   Youngblut, M.; Judd, E. T.; Srajer, V.; Sayyed, B.; Goelzer, T.; Elliott, S. J.; Schmidt, M.; Pacheco, A. A., Laue crystal structure of Shewanella oneidensis cytochrome c nitrite reductase from a high-yield expression system. *J Biol Inorg Chem* **2012,** *17* (4), 647-62.

7.   Bykov, D.; Plog, M.; Neese, F., Heme-bound nitroxyl, hydroxylamine, and ammonia ligands as intermediates in the reaction cycle of cytochrome c nitrite reductase: a theoretical study. *JBIC Journal of Biological Inorganic Chemistry* **2014,** *19* (1), 97-112.

Appendix 1
Supporting Material
For Chapter 2

A1.1. Pyridine hemochromagen assay for determining the concentration of heme in purified ccNiR protein
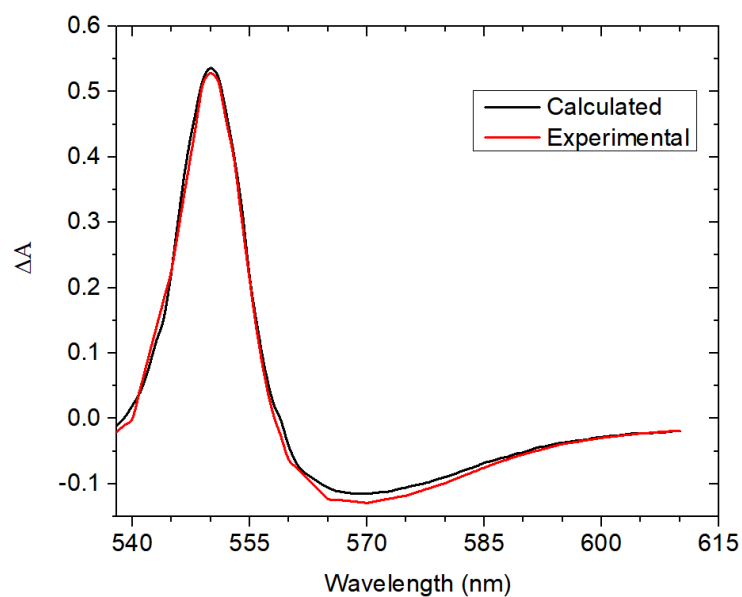

Fig. A1.1 Least-squares fit of a ccNiR pyridine hemochrome difference spectrum with a *c*-heme literature standard. The black trace is calculated from the literature extinction coefficient *c*-heme difference spectrum provided by Berry et al[1] and the red trace is for the pyridine hemochrome difference spectrum generated for a wtccNiR sample using the procedure of Barr et al.[2]

A1.2. Effect of TMPD$_{ox}$ on the ccNiR-catalyzed reduction of nitrite by TMPD

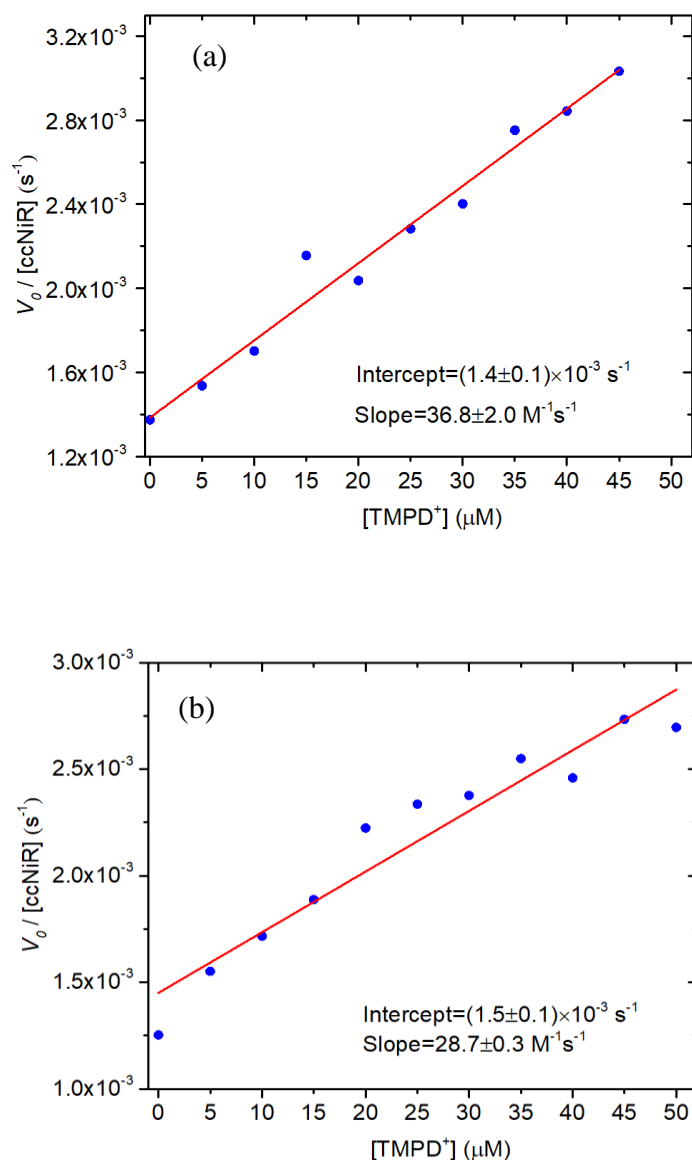Below are two figures equivalent to Fig. 2.4 equivalent, but obtained with [TMPD] = 400 μM and 800 μM instead of 600 μM.

Fig. A1.2 Dependence of V_0/[ccNiR] (where V_0 is the initial rate of TMPD oxidation in M/s, obtained from fits of the corresponding Λ_1 components) on initial TMPD$^+$ concentrations in the presence of (a) 400 μM TMPD, and (b) 800 μM TMPD. The nitrite concentration was 1 mM in all experiments, and the ccNiR concentration was roughly 2 μM, with the exact concentration being obtained from the Λ_0 fits in each experiment. All experiments were in 50 mM HEPES buffer, pH 7.0

A1.3. Derivation of Equation 2.7 for analysis of the steady-state experiments

157

The Eq. 2.7 rate law is based on the Scheme 2.4 mechanism. It assumes that, under steady-state conditions, the only ccNiR species present in significant concentrations is $\{Fe_{H1}NO\}^7$, and that the rate-limiting steps in catalytic NO· formation are breaking of the $Fe_{H1} - NO$ bonds in $\{Fe_{H1}NO\}^7$ and $\{Fe_{H1}NO\}^6$. In Eq. A1.1 we apply the steady-state treatment to

$$\frac{d\{Fe_{H1}NO\}^6}{dt} = 0 = k_{ox}[TMPD^+]\{Fe_{H1}NO\}^7 - \left(k_{red}[TMPD] + k_{1NO}\right)\{Fe_{H1}NO\}^6 \qquad \text{A1.1}$$

$\{Fe_{H1}NO\}^6$. Solving Eq. A1.1 for $\{Fe_{H1}NO\}^6$ gives Eq. A1.2. Equation A1.3 is the rate equation for the appearance of NO·. Since the electron that reduces NO· comes from TMPD, the rate of

$$\{Fe_{H1}NO\}^6 = \frac{k_{ox}[TMPD^+]\{Fe_{H1}NO\}^7}{k_{red}[TMPD] + k_{1NO}} \qquad \text{A1.2}$$

$$\frac{d[NO·]}{dt} = \frac{d[TMPD^+]}{dt} = k_{1NO}\{Fe_{H1}NO\}^6 + k_{2NO}\{Fe_{H1}NO\}^7 \qquad \text{A1.3}$$

$TMPD^+$ formation is the same as that of NO· formation, as is also shown in Eq. A1.3. Substituting Eq. A1.2 into Eq. A1.3 gives Eq. A1.4, which is the same as Eq. 2.7 if $\{Fe_{H1}NO\}^7 = [ccNiR]_{total}$.

$$\frac{d[NO·]}{dt} = \frac{d[TMPD^+]}{dt} = \{Fe_{H1}NO\}^7 \left\{ \frac{\left(k_{1NO}/k_{red}\right)·k_{ox}}{[TMPD] + \left(k_{1NO}/k_{red}\right)}[TMPD^+] + k_{2NO} \right\} \qquad \text{A1.4}$$

A1.4. References

1.   Berry, E. A.; Trumpower, B. L., Simultaneous determination of hemes a, b, and c from pyridine hemochrome spectra. *Anal Biochem* **1987,** *161* (1), 1-15.

2.   Barr, I.; Guo, F., Pyridine Hemochromagen Assay for Determining the Concentration of Heme in Purified Protein Solutions. *Bio Protoc* **2015,** *5* (18).

Appendix 2
Supporting Material
For Chapter 3

A2.1 Constructing active site variants of the ccNiR gene and transforming into into *S.*

***oneidensis* TSP-C cells**
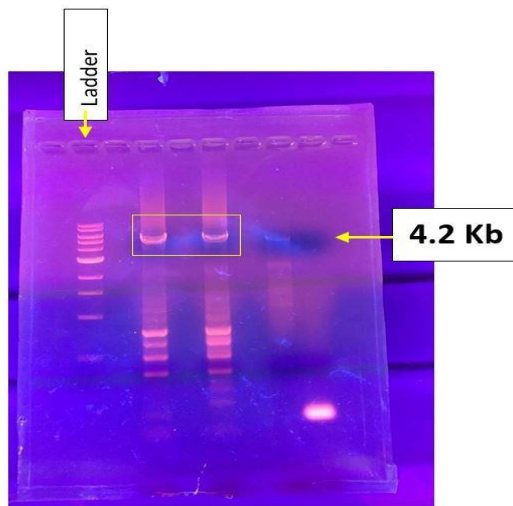

Figure A2.1. Agarose gel electrophoresis of the PCR products obtained after attempted H257Q mutation of wtccNiR. The 4.2 kb band shows the ccNiR gene-containing plasmid, correctly amplified by PCR.
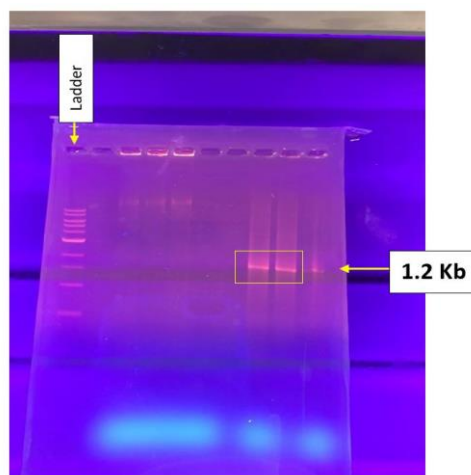

Figure A2.2. Agarose gel electrophoresis of the PCR product obtained using the sequencing primers. The 1.2 kb band shows the presence of mutant ccNiR, correctly amplified by PCR.

A2.2. Determination of the optimum imidazole concentration in loading buffer

Figure A2.3 shows how the A_{410}/A_{280} ratio of the eluant band from the HisTrap FF column chromatography step of H257Q purification varied as the imidazole concentration in the loading buffer was increased from 0 – 60 mM. The A_{410}/A_{280} ratio of pure ccNiR is greater than 3.8, so this ratio provides a quick and convenient estimate of the eluant's purity. The A_{410}/A_{280} ratio in Fig. A2.3 increases steadily until the imidazole concentration reaches 30 mM and then levels off, showing that 30 - 50 mM imidazole is needed to avoid unwanted non-specific protein binding during the column loading process.
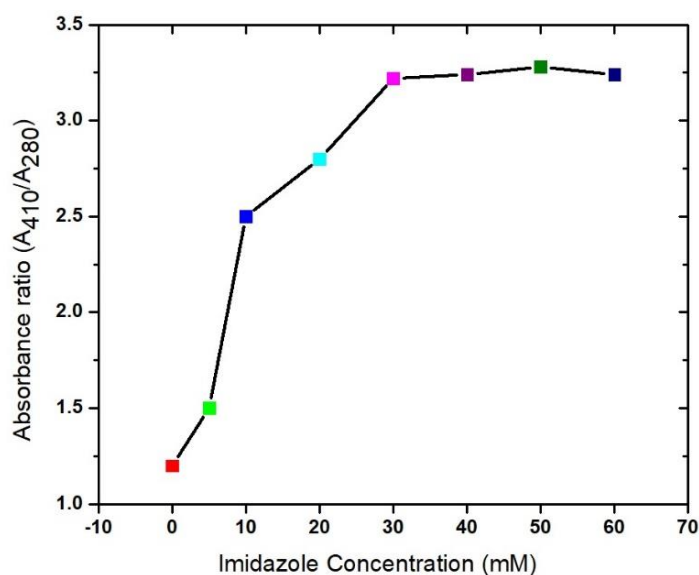

Figure A2.3. Determination of the optimum imidazole concentration needed in the binding (loading) buffer during HisTrap FF column chromatography (See main section 3.2.3.2 for details).

A2.3. TEV protease expression and purification protocol

The pET-28-TEVpM2 plasmid was transferred into BL21 *E. coli* cells. A single colony of bacteria was inoculated into 4 x 20 mL of LB Broth with 50 µg/ml Kanamycin into each tube as a starter culture. The starter culture was grown at 37 °C and continued for approximately 2.5 hours (optical density value 0.6 - 0.9 at 600 nm). The inducer IPTG (400 µL of 1 M) was added and continued to grow overnight at 22 °C. The overnight culture was spun down at $5,800 \times g$ for 20 min and the cell pellets collected. The bacterial cell pellets were resuspended with 25 mM tris, 300 mM NaCl, 10 mM Imidazole at pH 8.0, namely buffer A (1 g pellet ≈ 5 mL buffer A). To lyse the cell pellet, sonication was applied with the following parameters: 60 % power for 10 min 30 sec on 45 sec off. After spinning down the lysed sample, the supernatant was loaded onto the nickel column pre-equilibrated with buffer A. After loading all the samples, the column was again washed with buffer A. The sample was eluted using buffer B (25 mM Tris pH 8.0, 300 mM NaCl, 250 mM Imidazole) with a 4-step gradient of buffer B (0 % to 15 %, 50 %, 100%). The 50 % buffer B eluant contained pure TEV protein, as confirmed by SDS-electrophoresis (Fig A2.4). The buffer of the pure TEV protein was exchanged for 25 mM Tris, pH 8.0, after which the sample was concentrated to100 µM and stored at -80 °C.
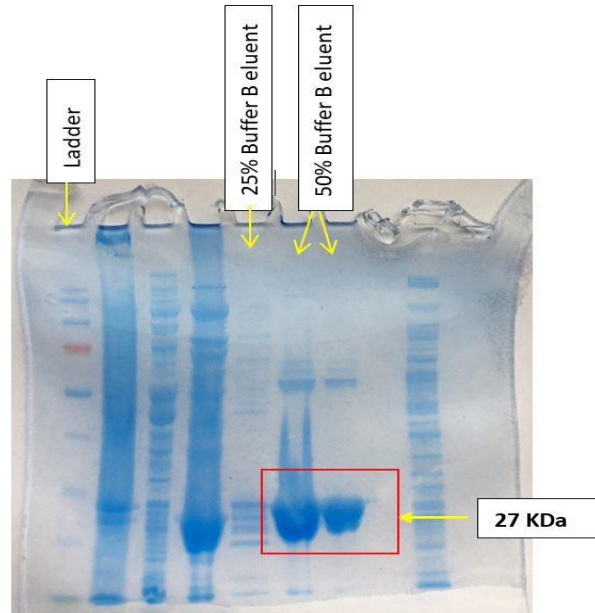
Figure. A2.4. SDS-gel electrophoresis the fractions obtained during TEV protease purification. The leftmost lane of the gel was loaded with a commercial ladder. 50 % Buffer B eluent shows a band at 27 kDa[1-2] which confirms the pure TEV protease. The two lanes of 50 % eluent show the same sample, the left 50 % buffer B eluent lane shows a more concentrated sample than the right 50 % buffer eluent (details discussed in the A2.3 main text).
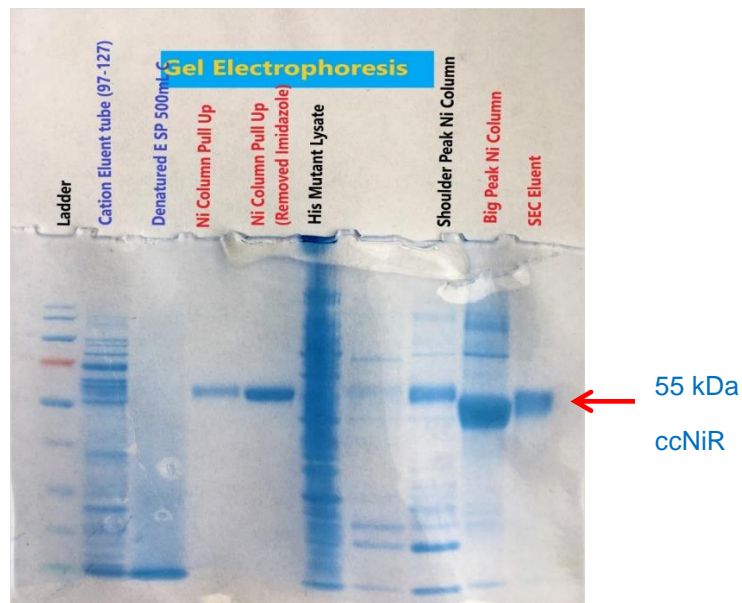

Figure A2.5. SDS-gel electrophoresis of the H257Q variant at various stages of purification. The leftmost lane of gel was loaded with a commercial ladder. The rightmost lane shows the pure mutant ccNiR from the last step of purification (eluent from the size exclusion column). The molecular weight of *Shewanella oneidensis* ccNiR is approximately 55 kDa.[3-4]

162

A2.4. References

1.   Nallamsetty, S.; Kapust, R. B.; Tözsér, J.; Cherry, S.; Tropea, J. E.; Copeland, T. D.; Waugh, D. S., Efficient site-specific processing of fusion proteins by tobacco vein mottling virus protease in vivo and in vitro. *Protein Expr Purif* **2004,** *38* (1), 108-15.

2.   Wu, X.; Wu, D.; Lu, Z.; Chen, W.; Hu, X.; Ding, Y., A novel method for high-level production of TEV protease by superfolder GFP tag. *J Biomed Biotechnol* **2009,** *2009*, 591923.

3.   Ali, M.; Stein, N.; Mao, Y.; Shahid, S.; Schmidt, M.; Bennett, B.; Pacheco, A. A., Trapping of a Putative Intermediate in the Cytochrome c Nitrite Reductase (ccNiR)-Catalyzed Reduction of Nitrite: Implications for the ccNiR Reaction Mechanism. *J Am Chem Soc* **2019,** *141* (34), 13358-13371.

4.   Youngblut, M.; Judd, E. T.; Srajer, V.; Sayyed, B.; Goelzer, T.; Elliott, S. J.; Schmidt, M.; Pacheco, A. A., Laue crystal structure of Shewanella oneidensis cytochrome c nitrite reductase from a high-yield expression system. *J Biol Inorg Chem* **2012,** *17* (4), 647-62.

Curriculum Vitae

SHAHID SHAHID

shahid.shahid55k@gmail.com

LinkedIn   Google Scholar   Research Gate Chemistry Department,UWM

Current Position:
PhD Candidate
Biological Chemistry and Structural Biology Lab
Supervisor: Dr. A. Andrew Pacheco (Professor)
Tentative Thesis Title: A Mechanism Investigation of Cytochrome c Nitrite Reductase Catalyzed
Reduction of Nitrite to Ammonia: A search for Catalytical Intermediates
Graduate Research Seminar: Helicase and Translocase Activities of UvrD: A novel Discovery
for DNA Repair Mechanism
Department of Chemistry and Biochemistry, University of Wisconsin-Milwaukee, Wisconsin, US

Education
2020: PhD, University of Wisconsin-Milwaukee, Wisconsin, US
2011: MS, Department of Biochemistry and Molecular Biology, University of Dhaka, Bangladesh
2010: BS, Department of Biochemistry and Molecular Biology, University of Dhaka, Bangladesh

Publication
•**Shahid, Shahid**, et al ''Kinetics Analysis of Early Stage of Cytochrome *c* Nitrite Reductase
(CcNiR) Enzyme catalyzed Nitrite Reduction to Ammonia: A search for Catalytical
Intermediates'', Manuscript in Preparation, Anticipate publishing in Journal of the American
Chemical Society (JACS).2021

•**Shahid, Shahid**, et al. ''New mechanistic insight of Cytochrome c Nitrite Reductase (ccNiR) it's
variants; H257QccNiR and R103QccNiR, Manuscript in Preparation'', Anticipate publishing in
Biochemistry.2021

• New Mechanistic Insight of Cytochrome c Nitrite Reductase Enzyme and It's Variants''
American Society for Biochemistry and Molecular Biology **(ASBMB), 2020**, Abstract Published
in '***The FASEB Journal, V34, IS1***'

•Mahbbat Ali, Natalia Stein, Yingxi Mao, **Shahid Shahid,** Marius Schmidt, Brian Bennett, A. Andrew Pacheco. "Trapping of a putative intermediate in the *Shewanella oneidensis* cytochrome *c* nitrite reductase (ccNiR)-catalyzed reduction of nitrite: implications for the ccNiR reaction mechanism." Journal of the American Chemical Society (JACS).2019, 141, 34, 13358-13371

Professional Summary and Research Experience
Graduate Research Assistant
Biological Chemistry & Structural Biology Lab, Department of Chemistry and Biochemistry, University of Wisconsin-Milwaukee, WI, USA

1. **Site directed mutation of cytochrome c nitrite reductase (ccNiR) enzyme and gene expression in *Shewanella oneidensis* bacteria**
   - Mutated the active site of H257QccNiR, R103QccNiR gene and expressed mutated ccNiR into TSPC cells of *S. oneidensis*
   - Developed large scale *S. oneidensis, E. coli* culture **(50L)** protocol to purify bulk amount of **ccNiR** protein
   - Improved chromatographic techniques for high yield protein purification using First Performance Liquid Chromatography (FPLC)
   - Designed UNICORN™ 7.0 software programs to purify large scale protein automatically

2. **New mechanistic insight of ccNiR and it's variants (R103QccNiR, H257QccNiR)**
   - Determined kinetic parameters (K_m, V_{max}, k_{cat}) and designed activity assay of ccNiR in **anaerobic** condition using **glovebox** (MBRAUN)
   - Investigated the roles of active site amino acid residues (R103QccNiR, H257QccNiR) by studying thermodynamics and thermo-kinetics
   - Designed kinetic programs using **Mathcad** and **Origin** software to analysis spectropotentiometric behavior of enzyme

3. **Spectroscopic characterization of the ccNiR reduction of nitrite**
   - Analyzed the UV/Vis and electro-paramagnetic resonance (EPR) spectropotentiometric behavior of nitrite loaded H257QccNiR
   - Performed stopped-flow, time resolved, rapid freeze-quench spectroscopy to analyze nitrite loaded ccNiR reduction kinetics and stablished a novel mechanism proving intermediates formation unlike *in vivo*
   - Investigated the midpoint potential of active site heme of wtccNiR, H257QccNiR and R103QccNiR by applying controlled potential

2. Graduate Teaching Assistant

Department of Chemistry and Biochemistry, University of Wisconsin-Milwaukee, WI

- Performed both lecture and laboratory classes for Survey of Biochemistry, General Chemistry, Chemistry for Engineer
- Taught more than **100** Students each semester and made quizzes, graded quizzes and exams
- Performed online classes due to Covid 19 emergency

3. Mentorship Assistance

Department of Chemistry and Biochemistry, University of Wisconsin-Milwaukee, WI

- Mentored more than **20 new graduate teaching assistants** for three semesters and intensively trained three of them
    1) Nicholas Zahn, mzahn@uwm.edu, Spring 2018
    2) Nicholas Robert Lewandowski, lewand65@uwm.edu, Fall 2018
    3) Daniel Andrew Webb dawebb@uwm.edu, Fall 2019
- **Supervised two Undergrad students and designed their research projects**
    1) Jacob Paul Adams, jacobpadams@icloud.com, adamsjp@uwm.edu, Fall 2019
    2) Tyler David Holz, tyholz1213@gmail.com, tdholz@uwm.edu, Spring 2020
    3) William Brown Marston, wmarston@uwm.edu, Spring 2020

Major Skills

Major Microbiology and Molecular Biology Skills

- Gene expression and cloning
- Large scale bacterial cell culture **(45L)** of *S. oneidensis* and *Mycobacterium tuberculosis* for bulk protein purification
- Chromosomal and plasmid DNA extraction and DNA sequencing
- Side directed mutation of active site of enzyme/ gene mutation
- Real time polymerase chain reaction (RT-PCR)

Biochemistry Skills

- Protein purification in high scale (**ccNiR**, **truncated hemoglobin**, Cytochrome P450, Catalase, TEV Protease, glucose oxidase)
- Design kinetic and assay model for determining **protein misfolding and aggregation**
- **Pyridine Hemochromagen Assay**
- Hydrophobic Interaction/ Ion-Exchange (cation/ anion)/ Affinity chromatography/ Size-Exclusion chromatography
- Column packing, preparation and regeneration, Tangential flow filtration
- Northern/ Western/ Southern Blot, Gel electrophoresis, Pyridine hemochromagen assay
- Bioinformatics for new protein characterization and drug target optimization
-

Immunological Skills
- Antibody isolation and purification
- **ELISA**: enzyme-linked immunosorbent assay for antibodies detection
- Antibody for lymphocyte supernatant (ALS) for *Mycobacterium tuberculosis* detection
- Immunoblotting

Analytical Skills & Machine Expertise
- **FPLC** (AKTA Pure)-Fast Protein Liquid Chromatography for protein purification
- **Stopped-Flow** (XS20, Applied Photophysics) for pre-steady state kinetics analysis of enzymatic reactions.
- **Glovebox** (MBraun) for analyzing oxidation-reduction reaction in Anaerobic condition
- **UV/Vis** spectropotentiometry for characterizing redox-active enzymes
- **BASi Electrochemical Analyzers**
- **Schlenk Line System** for degas solvents (enzymes, buffer)
- **Stereo Microscope** (AmScope)

Software Expertise
- **PyMol**: Protein molecule visualization system
- **Mathcad** and MATLAB: Used to fit kinetic data to investigate the enzyme's reaction mechanism
- **Origin 8/9:** Used for interactive scientific graphing and data analysis
- **CorelDRAW**: Used for reaction and instrument graphic designing
- **UNICORN™ 7** Software based on AKTA pure system to purify large scale protein automatically
- **KINETICS**: Cary Win UV Software for record steady state spectrometric data
- **Pro-Data View/ SX** (Applied Photo-physics) analyzing stopped-flow spectral based kinetics

Statistical Analysis
- Michaelis Menten Fitting, Lineweaver–Burk plot for enzyme's parameters K_m, k_{cat}, Vmax
- **Global Fit Analysis** (Linear or Nonlinear Least-Squares Analysis, Simulate Curve, Single/Multiple Linear Regression)
- Singular Value Decomposition, t-test, Z-test, ANOVA

Awards and Prizes
- **Chancellor's graduate fellowship**, Department of Chemistry and Biochemistry; UWM; September 2015 to Present

Certificates and Training

- Biosafety Training, Provided by UWM, 2016-2019
- Sci-Finder n Training, UWM, 2020
- President, Bangladesh Student Association, UWM, 2019-2020
- COVID-19: Operational Planning Guidelines & COVID-19 Partners platform to support country preparedness and response (WHO, online, 2020)

Conference and Poster Presentation

- New Mechanistic Insight of Cytochrome c Nitrite Reductase Enzyme and It's Variants'' Enzymes, Coenzymes and Metabolic Pathways, **Gordon Research Conference, 2020**, Abstract accepted
- New Mechanistic Insight of Cytochrome c Nitrite Reductase Enzyme and It's Variants'' American Society for Biochemistry and Molecular Biology **(ASBMB), 2020**, Abstract Published in '*The FASEB Journal, V34, IS1*'
- New Mechanistic Insight of Cytochrome c Nitrite Reductase Enzyme
  Midwest Enzyme Chemistry Conference, Illinois Institute of Technology, October **2019**
- Towards the Novel Mechanism of Nitrite to Ammonia by Cytochrome c Nitrite Reductase (ccNiR)', UWM Chemistry and Biochemistry Symposium **(2016,2017,2018,2019)**
- Cytochrome c Nitrite Reductase: A Novel Enzyme Mechanism to Study Dissimilatory Nitrite Reduction'
  Dhaka University Biochemistry Alumni in North America (**DUBANA), NY, June 2018**
- Cytochrome c Nitrite Reductase: A Novel Enzyme Mechanism to Study Dissimilatory Nitrite Reduction'
  Bangladesh Chemical and Biochemical Association in North America (**BACABANA**), Milwaukee, WI, August **2018**